Employing γ-ray Tracking as an Event-discrimination Technique for γ-spectroscopy with AGATA

Anwendung von γ-ray Tracking als Ereignis-basierte Distinktionstechnik für die γ-Spektropskopie mit AGATA

Zur Erlangung des Grades eines Doktors der Naturwissenschaften (Dr. rer. nat.) genehmigte Dissertation im Fachbereich Physik von Philipp Napiralla aus Kronach

Tag der Einreichung: 19.11.2019, Tag der Prüfung: 09.12.2019

1. Gutachten: Prof. Dr. Dr. h.c. mult. Norbert Pietralla
2. Gutachten: Prof. Dr. Herbert Egger

Darmstadt – D 17

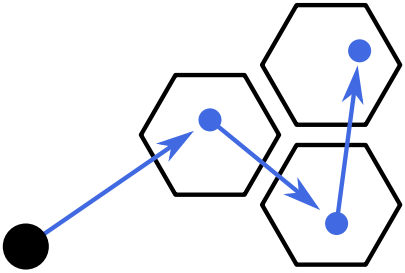

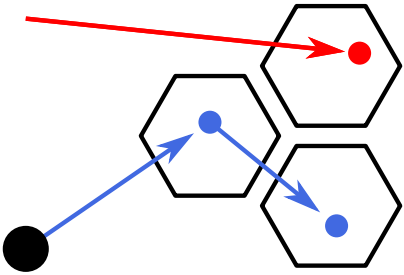

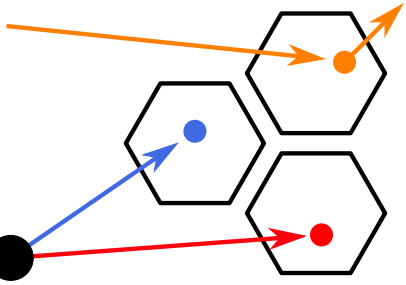

TECHNISCHE UNIVERSITÄT DARMSTADT

Fachbereich Physik
Institut für Kernphysik
AG Pietralla

Sponsored by

HIC for FAIR
Helmholtz International Center

HGS-HIRe for FAIR
Helmholtz Graduate School for Hadron and Ion Research

Bundesministerium für Bildung und Forschung
under grant Nos.
05P15RDFN9, 05P18RDFN9

Employing γ-ray Tracking as an Event-discrimination Technique for γ-spectroscopy with AGATA
Anwendung von γ-ray Tracking als Ereignis-basierte Distinktionstechnik für die γ-Spektropskopie mit AGATA

genehmigte Dissertation im Fachbereich Physik von Philipp Napiralla

1. Gutachten: Prof. Dr. Dr. h.c. mult. Norbert Pietralla
2. Gutachten: Prof. Dr. Herbert Egger

Tag der Einreichung: 19.11.2019
Tag der Prüfung: 09.12.2019

Darmstadt – D 17

Bitte zitieren Sie dieses Dokument als:
URN: urn:nbn:de:tuda-tuprints-96737
URL: http://tuprints.ulb.tu-darmstadt.de/9673

Dieses Dokument wird bereitgestellt von tuprints,
E-Publishing-Service der TU Darmstadt
http://tuprints.ulb.tu-darmstadt.de
tuprints@ulb.tu-darmstadt.de

Die Veröffentlichung steht unter folgender Creative Commons Lizenz:
Namensnennung – Nicht kommerziell – Keine Bearbeitungen 4.0 International
https://creativecommons.org/licenses/by-nc-nd/4.0/deed.de

Erklärungen laut Promotionsordnung

§8 Abs. 1 lit. c PromO

Ich versichere hiermit, dass die elektronische Version meiner Dissertation mit der schriftlichen Version übereinstimmt.

§8 Abs. 1 lit. d PromO

Ich versichere hiermit, dass zu einem vorherigen Zeitpunkt noch keine Promotion versucht wurde. In diesem Fall sind nähere Angaben über Zeitpunkt, Hochschule, Dissertationsthema und Ergebnis dieses Versuchs mitzuteilen.

§9 Abs. 1 PromO

Ich versichere hiermit, dass die vorliegende Dissertation selbstständig und nur unter Verwendung der angegebenen Quellen verfasst wurde.

§9 Abs. 2 PromO

Die Arbeit hat bisher noch nicht zu Prüfungszwecken gedient.

Darmstadt, den 19.11.2019

Philipp Napiralla

Für *Hartmut*,
meinen Großvater

If you can meet with Triumph and Disaster
And treat those two impostors just the same;

From *If–* by Rudyard Kipling [Kip10]

Abstract

This doctoral thesis focuses on the utilization of γ-ray tracking for the distinction between different scenarios, such as various possible incident γ-ray energies or different points of their origin. Such scenarios arose in an experimental benchmark test of the so-called *Coulex-multipolarimetry*, as well as in a first simulation-based approach to potential competitive double γ-decay experiments with the Advanced GAmma Tracking Array AGATA.

The first benchmark of the *Coulex-multipolarimetry* was performed during the PreSPEC campaign at the GSI Helmholtzzentrum für Schwerionenforschung in 2014 to identify the potential $\pi p_{3/2} \rightarrow \pi p_{1/2}$ spin-flip transition in the neutron-rich ^{85}Br via measurement of the $E2/M1$ multipole mixing ratio δ. The achieved performance of said first benchmark test is presented using standard methods of γ-spectroscopy as well as γ-ray tracking and derived methods.

The competitive double γ decay, measured for the first time in ^{137}Ba in 2015 via $LaBr_3$(Ce) detectors, is a potential source for new information about nuclear structure. Since angular and energy correlations between the emitted γ rays are one of the main sources of said information, AGATA with its high angular and energy resolution appears to be predestined for this task. Due to its comparatively small time resolution capabilities, a successful distinction between single and double γ-decay events, however, has to fully rely on γ-ray tracking techniques. Whether such measurements of the double γ decay with AGATA are feasible is verified in this work based on simulations. Novel insights into γ-ray tracking which arose during the analysis resulted in the development of a novel γ-ray tracking algorithm, called `ExpTrack`, based on experimentally achieved Compton-scattering angles. This new approach is also presented in this work.

Zusammenfassung

Im Rahmen dieser Doktorarbeit soll die Anwendung von γ-ray tracking für die Unterscheidung verschiedener Szenarien, die bei der Emission von γ Strahlung auftreten, beschrieben werden. Beispiele hierfür sind die Identifikation der Quellposition, beziehungsweise die Energie der gemessenen γ Strahlung. Die genannten Szenarien traten beim ersten Benchmark-Test der *Coulex-Multipolarimetrie* Methode sowie bei der Analyse potentieller Experimente des kompetitiven doppelten γ Zerfalls mit dem Advanced GAmma Tracking Array AGATA auf.

Der erste Benchmark-Test der *Coulex-Multipolarimetrie* Methode wurde im Jahr 2014 im Rahmen der PreSPEC Kampagne am GSI Helmholtzzentrum für Schwerionenforschung durchgeführt. Ziel war die Identifikation des potentiellen einteilchen $\pi p_{3/2} \rightarrow \pi p_{1/2}$ Spin-flip Übergangs des neutronen-reichen ^{85}Br mittels der Bestimmung des $E2/M1$ Multipolmischungsverhältnisses δ. Die erreichbare Performance des Experiments basierend auf üblichen γ-spektroskopischen Methoden als auch auf γ-ray tracking und davon abgeleiteten Methoden wird präsentiert.

Der kompetitive doppelte γ Zerfall, der erstmals in ^{137}Ba im Jahr 2015 mit Hilfe von $LaBr_3$(Ce) Detektoren nachgewiesen werden konnte, kann weitere Einblicke in die Struktur verschiedenster Kerne ermöglichen. Da viele dieser potentiellen Informationen in der Winkel- sowie Energiekorrelation der emittierten γ Strahlen enthalten sind, scheint AGATA prädestiniert für diese Aufgabe zu sein. Aufgrund der vergleichsweise niedrigen Zeitauflösung von AGATAs Germaniumdetektoren sind erfolgreiche Experimente des doppelten γ-Zerfalls mit AGATA vollständig auf γ-ray tracking Methoden angewiesen. Ob solche Experimente realisierbar mit AGATA sind, wird in dieser Arbeit verifiziert. Die im Rahmen der Analyse gewonnenen Erkenntnisse über das γ-ray tracking resultierten in einem neuen Ansatz für das γ-ray tracking basierend auf experimentellen Daten, benannt `ExpTrack`, welcher im Rahmen dieser Arbeit vorgestellt wird.

Contents

1. Introduction

Nuclear physics experiments, be it for the study of astrophysical processes or the underlying structure of nuclei, are often based on spectroscopic methods. One particular concept is γ-spectroscopy, an experimental technique in which γ rays from subsequent γ decays in the nucleus of interest are measured, yielding information about nuclear structure properties such as the geometrical shape of the nucleus. Over the course of history, γ-ray detectors have increased in resolution drastically. Starting from the mere ability to detect ionizing γ rays using Geiger-Müller counters, over to the first energy resolving detectors such as scintillation detectors like NaI-scintillators, detector science has culminated in high-resolving High Purity Germanium (HPGe) detectors – single crystal germanium with highest achievable purity. Since germanium has a comparatively low γ-ray detection efficiency, larger and larger arrays of germanium detectors were built to geometrically cover wide areas of solid angle. The latest type of germanium detector arrays, so-called γ-ray tracking arrays, are designed, such that they practically form a complete shell of germanium around the source position of emitted γ rays. Via the high-achievable position resolution of these γ-ray tracking arrays, the physical paths of incident γ rays can be mathematically reconstructed via their known interaction processes in germanium. At the moment, there exist two realizations of such γ-ray tracking arrays – the European project of the Advanced GAmma Tracking Array AGATA [Akk12] and the American project of the Gamma Ray Energy Tracking Array GRETA [GRE17], currently realized as the Gamma-Ray Energy Tracking In-beam Nuclear Array GRETINA [Lee04]. Although a full 4π solid angle coverage is still not accomplished by both projects, successful campaigns for AGATA [Bos19, Sta15c, Ral17a, Dud17] as well as for GRETINA [Wol19, Iwa14, Gad14] were already performed.

Based on the high achievable position resolution and the novelty of γ-ray tracking, new experimental techniques such as Compton imaging via γ-ray tracking [Rec09a, Ste17] as well as background reduction based on said imaging methods [Don10] arose. In addition, experiments with relativistic beams that predomi-

nantly suffered from large beam-velocity induced Doppler-shifts with geometrically limited possibilities for correction of these Doppler-shifts, can now be corrected with high geometrical granularity. A lifetime determination method that utilizes this high granularity is the so-called continuous angle Doppler-shift attenuation method [Sta17]. The novelty of γ-ray tracking can also be used as an experimental discrimination technique, differentiating between the likeliness of multiple causes for the measurements, such as the discrimination between different types or position of emission of incident γ rays. These scenarios are subject of this thesis.

The first scenario is a benchmark test of a novel technique based on relativistic ion beams, called *Coulex-multipolarimetry* [Sta15b], emulating a two-beam energy setup with two thick gold targets and specifically developed for germanium arrays with high granularity such as AGATA. The achievable performance of the first experiment based on this new method, designed to measure the potential $\pi p_{3/2} \rightarrow \pi p_{1/2}$ spin-flip transition in the radioactive even-odd nucleus ^{85}Br, is presented employing standard γ-spectroscopy analysis techniques as well as γ-ray tracking. In addition, a γ-ray tracking discrimination approach for the emission point of γ rays is shown.

The second scenario is based on the competitive double γ-decay, a second-order quantum mechanical process in which a decay from an initial nuclear state J_i to a final state J_f is performed via the emission of two γ rays that share the energy of the single γ-decay photon. However, this process is strongly suppressed compared to the single γ decay. Novel information about nuclear structure such as generalized polarizabilities are accessible via successful measurements of the competitive double γ decay and its underlying angular and energetic correlations between the emitted γ rays. So far, only two possible angles were measured for the only observation of the competitive double γ decay in ^{137}Ba. Since AGATA's angular resolution is in the range of 1°, measurements of the competitive double γ decay seem reasonable. Whether such measurements are possible based on AGATA's γ-ray tracking performance is analyzed.

In Chapter 2, all necessary physical and mathematical prerequisites are presented. Emphasis lies on the theoretical description of relativistic Coulomb excitation as well as the competitive double γ decay. In addition, the mathematical

background of often used probability density functions and probability distributions is presented.

Chapter 3 focuses on the description of the Advanced GAmma Tracking Array AGATA and its mode of operation. The principle behind its high position resolution, the so-called Pulse-Shape Analysis, is presented. In addition, the mathematical principle behind γ-ray tracking and standard tracking algorithms such as the Orsay Forward Tracking [Lop04, KL19] and the Mars Gamma-ray Tracking [Baz04, KL19] are presented.

The first benchmark test of the *Coulex-multipolarimetry* based on the $\pi p_{3/2} \rightarrow \pi p_{1/2}$ spin-flip transition in ^{85}Br is shown in Chapter 4. Here, the underlying experiment S426 at PreSPEC at GSI Helmholtzzentrum für Schwerionenforschung is presented. Calibration techniques for the used particle and γ-ray detectors as well as data analysis methods via particle-γ-ray conditions are shown. The achievable performance with standard γ-spectroscopic methods in addition to the impact of γ-ray tracking are presented. Target identification methods based on γ-ray tracking are portrayed.

Chapters 5 and 6 focus on the potential measurement of the competitive double γ-decay with AGATA. In Chapter 5, a novel γ-ray tracking algorithm called `ExpTrack` that was developed based on experimental data and especially designed for competitive double γ-decay experiments with AGATA is presented. The achieved performance is compared to the Orsay Forward Tracking algorithm using a ^{137}Cs source measurement. Chapter 6 focuses on the simulation and discrimination analysis of the single and double γ-decay in ^{137}Ba with AGATA. The analysis is performed with the Orsay Forward Tracking as well as with the novel γ-ray tracking algorithm `ExpTrack`. The discrimination performance of both algorithms is presented and discussed.

Summary and outlook of this work are given in Chapter 7.

2. Theoretical Background

A general description of all physical and mathematical prerequisites is given in this Chapter. For a more detailed description, the reader is referred to the respective mentioned references (and references therein).

2.1. Relativistic Coulomb Excitation

There are many possibilities to measure nuclear properties arising from the shell structure of nuclei [Göp48, Göp49, Hax49] such as single particle excitation energies or collective phenomena of the nucleus [Cas05], e.g., described in the interactive boson model [IA87] or quasi-particle phonon model [Sol92]. For stable nuclei, methods like nuclear resonance fluorescence [Kne96] or inelastic electron scattering [Übe71, The06] can be used to access such nuclear structure information. However, in the vicinity of radioactive nuclei, these methods cannot be efficiently utilized since targets might not be producible due to potentially short lifespans of the nuclei of interest. In such scenarios, the method of *Coulomb excitation* (CoulEx) can be applied [Ald56, AW66, AW75, AW79] since accelerated short-lived nuclei are excited and decay in such a short time-span that γ-spectroscopic experiments can be performed in direct vicinity of the excitation. CoulEx is the electromagnetic excitation of a nucleus during the collision process with another nucleus. In the so-called semi-classical limit, the scattering process can be expressed in terms of classical particle trajectories instead of quantum-mechanical wave functions. To verify whether the semi-classical approach is applicable, the Sommerfeld parameter [AW66]

$$\eta = \frac{2a}{\lambda} = \frac{2Z_P Z_T \alpha \hbar c}{\hbar v}, \tag{2.1}$$

with the half-distance of closest approach in a head-on collision

$$a = \frac{Z_P Z_T \alpha \hbar c}{\mu v^2}, \tag{2.2}$$

the reduced mass

$$\mu = \frac{m_T m_P}{m_T + m_P}, \tag{2.3}$$

with the respective masses of the target nucleus m_T and projectile nucleus m_P, the angular de-Broglie wavelength $\lambda\!\!\!^{-} = \hbar/(\mu v)$ of the projectile, the fine-structure constant $\alpha \approx 1/137$ and the charge numbers of the beam projectile Z_P and target nucleus Z_T can be used. For $\lambda\!\!\!^{-} \ll 2a$, corresponding to $\eta \gg 1$, the orbit of the beam projectile can be described via a classical trajectory [AW66]. In the case of the analyzed ^{197}Au(^{85}Br,^{85}Br)^{197}Au reaction performed in Chapter 4 with $\beta \approx 0.6$, the Sommerfeld parameter is $\eta \approx 67$. In general, CoulEx can be expressed in terms of two different phenomena, the actual scattering process of the two collision partners and the electromagnetic excitation of the collision partners due to their mutually influencing electromagnetic fields. In the classical limit $\beta \to 0$, the scattering process can be described via the well-known Rutherford-scattering process and the CoulEx amplitudes $P_{n\to m}$ via

$$\left(\frac{\partial\sigma}{\partial\Omega}\right)_{\text{CoulEx}} = \left(\frac{\partial\sigma}{\partial\Omega}\right)_{\text{Ruth.}} P_{n\to m}, \tag{2.4}$$

with the differential cross section of the Rutherford scattering [AW66, Pov14]

$$\left(\frac{\partial\sigma}{\partial\Omega}\right)_{\text{Ruth.}} = \frac{a^2}{4}\sin^{-4}\left(\frac{\theta}{2}\right). \tag{2.5}$$

The parameter a is related to the scattering angle via

$$\tan\left(\frac{\theta}{2}\right) = \frac{a}{b}, \tag{2.6}$$

with the impact parameter b (see Fig. 2.1). The CoulEx probability is given by

$$P_{n\to m} = \frac{1}{2J_n + 1}\sum_{M_m M_n} |a_{J_n M_n, J_m M_m}|^2. \tag{2.7}$$

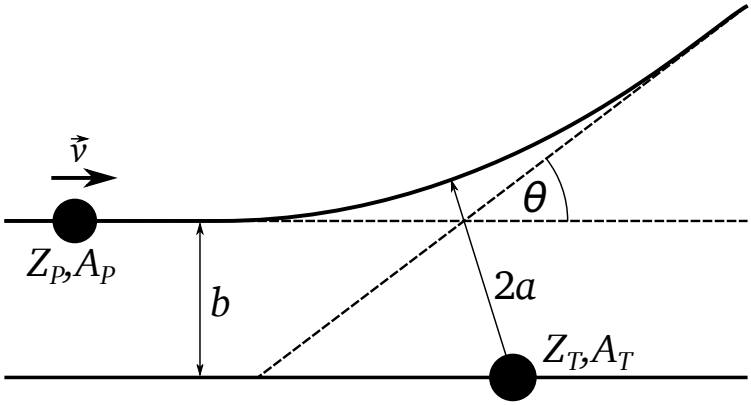

Figure 2.1.: Rutherford scattering of a projectile nucleus with mass number A_P and charge Z_P moving with velocity $\vec{v}$ off a non-moving target nucleus with mass A_T and charge Z_P. For details see text.

The transition probabilities $|a_{J_n M_n, J_m M_m}|^2$ for a transition from the initial state J_n to the final state J_m given the magnetic substates M_n and M_m is discussed in further detail in the following. The interaction between the two collision partners, the projectile P and the target nucleus T, can be expressed in terms of a Schrödinger equation describing the dynamics of an intrinsic wave function $|\Psi(t)\rangle$ [AW66]

$$i\hbar\frac{\partial}{\partial t}|\Psi(t)\rangle = [H_0(P) + H_0(T) + W(P,T,\vec{r}(t))]\,|\Psi(t)\rangle\ , \tag{2.8}$$

with the free Hamiltonians $H_0(\mathscr{P})$ with $\mathscr{P} = P \vee T$ for projectile and target nuclei. The electromagnetic interaction between projectile and target is described by

$$W(P,T,\vec{r}(t)) = V(P,\vec{r}(t)) + V(T,\vec{r}(t)) + \underbrace{\frac{Z_P Z_T e^2}{||\vec{r}(t)||}}_{V_{\text{mono}}}\ . \tag{2.9}$$

In addition to the interaction between the monopole moments of projectile and target V_{mono}, the multipole interaction of the target caused by the projectile called $V(T,\vec{r}(t))$ and vice versa $V(P,\vec{r}(t))$ can be split into purely magnetic and electric

components

$$V(\mathscr{P},\vec{r}(t)) = V_E(\mathscr{P},\vec{r}(t)) + V_M(\mathscr{P},\vec{r}(t)). \tag{2.10}$$

To express the electromagnetic interaction, the potentials $V_\sigma(\mathscr{P},t)$, where $\sigma = E$ denotes electric and $\sigma = M$ magnetic transitions, can be developed in a multipole expansion via [AW75]

$$V_\sigma(\mathscr{P},\vec{r}(t)) = \sum_{\lambda=1,\mu}^{\infty} \frac{4\pi Z_{\overline{\mathscr{P}}} e}{2\lambda+1} (-1)^\mu \overline{S}_{\sigma\lambda\mu}(t) \mathscr{M}(\sigma\lambda,-\mu) \tag{2.11}$$

with

$$\overline{\mathscr{P}} = \begin{cases} T\,, & \text{if } \mathscr{P} = P \\ P\,, & \text{if } \mathscr{P} = T \end{cases}. \tag{2.12}$$

Here, λ is the multipolarity, μ its projection onto the symmetry axis and $\mathscr{M}(\sigma\lambda,\mu)$ are the electric and magnetic multipole operators in spherical coordinates

$$\mathscr{M}(E\lambda,\mu) = \int \mathrm{d}\vec{r}\, \rho(\vec{r}) r^\lambda Y_{\lambda\mu}\left(\frac{\vec{r}}{r}\right), \tag{2.13}$$

$$\mathscr{M}(M\lambda,\mu) = \frac{-i}{c(\lambda+1)} \int \mathrm{d}\vec{r}\, \vec{j}(\vec{r}) r^\lambda L Y_{\lambda\mu}\left(\frac{\vec{r}}{r}\right), \tag{2.14}$$

with the angular momentum operator $L = -i\vec{r}\times\nabla$, the charge and current densities $\rho(\vec{r})$ and $\vec{j}(\vec{r})$, and the spherical harmonics $Y_{\lambda\mu}$. The orbital integrals are given by [AW75]

$$\overline{S}_{E\lambda\mu}(t) = \frac{1}{r^{\lambda+1}(t)} Y_{\lambda\mu}(\theta(t),\varphi(t)), \tag{2.15}$$

with the polar angle $\theta(t)$ of $\vec{r}$ and its azimuth $\varphi(t)$ for electric excitations, and by

$$\overline{S}_{M\lambda\mu}(t) = \frac{i}{\lambda} \frac{1}{r^{\lambda+1}(t)} \frac{\dot{\vec{r}}(t) L}{c} Y_{\lambda\mu}(\theta(t),\varphi(t)), \tag{2.16}$$

for magnetic excitations. The influence of the different multipolarities on the scattering scenario between projectile and target nucleus can be described in time

dependent perturbation theory (see [Fli18] for details).

Quantum mechanically, the dynamics of the respective nuclei can be expressed in terms of their initial state $|J_n, M_n\rangle$ and their final state after the scattering process $|J_m, M_m\rangle$. In addition, the so-called multipole moments, the expectation values of the respective multipole operators $\mathscr{M}(\sigma\lambda, \mu)$, can be simplified via

$$\langle J_m, M_m|\mathscr{M}(\sigma\lambda,\mu)|J_n, M_n\rangle = (-1)^{J_n - M_n}\begin{pmatrix} J_n & \lambda & J_m \\ -M_n & \mu & M_m \end{pmatrix} i^{-\lambda}\,\langle J_m||i^{\lambda}\mathscr{M}(\sigma\lambda)||J_n\rangle \tag{2.17}$$

expressing the multipole moments in terms of so-called reduced matrix elements $\langle J_m||i^{\lambda}\mathscr{M}(\sigma\lambda)||J_n\rangle$ using the Wigner-Eckart theorem [Rac42, AW66]. Here, $(\cdots)$ depicts the Wigner $3-j$ symbol [Suh07]. In a relativistic scope, including the reduced matrix elements, solutions to the Schrödinger equation (see Eq. (2.8)) in time-dependent perturbation theory (see [Fli18]) can obtained from the calculation of transition probabilities c_m, solving

$$\begin{aligned}\frac{\mathrm{d}c_m(\tau)}{\mathrm{d}\tau} = -i\alpha c \sum_{n\lambda\mu}\Bigg[&\exp(i\omega_{mn}\tau)(-1)^{J_n - M_n}\begin{pmatrix} J_n & \lambda & J_m \\ -M_n & \mu & M_m \end{pmatrix} \\ &\times i^{-\lambda}\,\langle J_m||i^{\lambda}\mathscr{M}(\sigma\lambda)||J_n\rangle\,\overline{S}_{\sigma\lambda\mu}(\tau)c_n(\tau)\Bigg],\end{aligned} \tag{2.18}$$

where $\tau = t/\gamma$ is the proper time in the particle's reference frame with the relativistic factor $\gamma = (1-\beta^2)^{-1/2}$. Equation (2.18) can be solved numerically [Ree18]. However, in the presented case of Chapter 4, only small scattering angles of the projectiles are analyzed. For such cases, the so-called straight-line approximation [AW79] yields an analytical solution to Equation (2.18).

2.1.1. Straight-line Approximation

In the ultra-relativistic limit $\beta \to 1$, the straight-line approximation in which the target is stationary and the projectile moves along a straight line with distance b to the target nucleus, can be applied. Here, the scattering angle is approximately given by [AW79]

$$\theta \approx \frac{\Delta p}{p}, \quad \text{with} \quad p = \gamma m v\,. \tag{2.19}$$

Hence, the scattering angle in the laboratory frame in the straight-line approximation is given by

$$\theta = \frac{2Z_P Z_T \alpha \hbar c}{m_P v^2 \gamma b}. \tag{2.20}$$

Since relativistic effects are relevant for a correct description of the scattering process, the electric and magnetic fields of the stationary target nucleus

$$\vec{E} = q\frac{\vec{r}}{r^3}, \qquad \vec{B} = \vec{0}, \tag{2.21}$$

where $r^3 = \left(b^2 + \gamma^2 v^2 t^2\right)^{3/2}$ describes the relativistic movement along the straight line, have to be Lorentz-boosted, yielding

$$\vec{E} = \frac{q\gamma}{r^3}\begin{pmatrix} -vt \\ b \\ 0 \end{pmatrix}, \quad \vec{B} = \frac{q\gamma b\beta}{r^3}\begin{pmatrix} 0 \\ 0 \\ 1 \end{pmatrix}. \tag{2.22}$$

Including the mutual repulsion transverse to the direction of flight of the projectile, the impact parameter is modified via [AW79]

$$b' = b + \frac{Z_P Z_T a \hbar}{\mu \beta^2 c \gamma}. \tag{2.23}$$

In first order perturbation theory and straight-line approximation (for details, see [AW79]), the analytic solution for Equation (2.18) expressed in terms of a single transition from $|J_n, M_n\rangle$ to $|J_m, M_m\rangle$ is given by

$$\begin{aligned} a_{J_n M_n, J_m M_m} = -i\frac{Z\alpha}{\beta\gamma}\sum_{\sigma\lambda\mu}\Big[& G_{\sigma\lambda\mu}\left(\beta^{-1}\right)(-1)^{\mu} K_{\mu}(\xi(b'))\sqrt{2\lambda+1}\, k^{\lambda} \\ & \times \langle J_m, M_m | \mathscr{M}(\sigma\lambda,\mu) | J_n, M_n \rangle \Big], \end{aligned} \tag{2.24}$$

where, for electric transitions with $\mu \geq 0$

$$\begin{aligned} G_{E\lambda\mu}\left(\beta^{-1}\right) = & i^{\lambda+\mu}\frac{\sqrt{16\pi}}{\lambda(2\lambda+1)!!}\sqrt{\frac{(\lambda-\mu)!}{(\lambda+\mu)!}}\frac{1}{\sqrt{\beta^{-2}-1}} \\ & \times\left[\frac{(\lambda+1)(\lambda+\mu)}{2\lambda+1}P^{\mu}_{\lambda-1}\left(\beta^{-1}\right) - \frac{\lambda(\lambda-\mu+1)}{2\lambda+1}P^{\mu}_{\lambda+1}\left(\beta^{-1}\right)\right] \end{aligned} \tag{2.25}$$

and for magnetic transitions with $\mu \geq 0$

$$G_{M\lambda\mu}\left(\beta^{-1}\right) = i^{\lambda+\mu+1}\frac{\sqrt{16\pi}}{\lambda(2\lambda+1)!!}\sqrt{\frac{(\lambda-\mu)!}{(\lambda+\mu)!}}\frac{1}{\sqrt{\beta^{-2}-1}}\mu P_\lambda^\mu\left(\beta^{-1}\right). \tag{2.26}$$

For $\mu < 0$, the relations

$$G_{E\lambda-\mu}\left(\beta^{-1}\right) = (-1)^\mu G_{E\lambda\mu}\left(\beta^{-1}\right), \tag{2.27}$$

$$G_{M\lambda-\mu}\left(\beta^{-1}\right) = (-1)^{\mu+1} G_{M\lambda\mu}\left(\beta^{-1}\right), \tag{2.28}$$

hold. In addition, $P_\lambda^\mu(x)$ are the associated Legendre functions evaluated at $x > 1$ and K_μ the irregular modified cylindrical Bessel function of order μ [AW79]. A full derivation of Equation (2.24) is depicted in [AW79]. The so-called adiabaticity

$$\xi(b') = \frac{\omega b'}{c\beta\gamma} = \omega T', \tag{2.29}$$

can be understood as a comparison between the oscillation of the nuclear excitation ω with the time scale

$$T' = b'\underbrace{\left(\frac{1}{\gamma}\frac{1}{c\beta}\right)}_{=1/v'}, \tag{2.30}$$

of the electromagnetic perturbation during the scattering process. The cross section for the CoulEx can be calculated via

$$\sigma_{J_n,J_m}(b_{\min}) = \frac{2\pi}{2J_n+1}\int_{b_{\min}}^{\infty} \mathrm{d}b \sum_{M_n,M_m} |a_{J_n,M_n,J_m,M_m}(b)|^2 b, \tag{2.31}$$

where $b_{\min}$ describes the closest distance between the two nuclei that still ensures that the nuclei are only excited via Coulomb interaction and not via nuclear interactions. Although rather phenomenological, the distance $b_{\min}$, referred to as the distance of "safe" CoulEx, can be calculated, e.g., via [Wol92]

$$b_{\min} = C_T + C_P + 5\,\mathrm{fm}, \tag{2.32}$$

where

$$C_i = R_i\left(1-\frac{1}{R_i^2}\right)\text{fm}, \quad \text{with} \quad R_i = 1.28A_i^{1/3} - 0.76 + 0.8A_i^{-1/3} \tag{2.33}$$

for $i = P \vee T$. Here, C_i are the radii of half-density of a Fermi mass distribution and R_i are nuclear radii calculated from the liquid drop model [Cas05] using the mass numbers A_i of the respective nuclei. The additional 5 fm are included to ensure safe CoulEx and is often referred to as *Cline's criterion* [Cli69].

2.1.2. DWEIKO

To calculate the cross sections σ_{J_n,J_m} (see Eq. (2.31)), the computer program Distorted Wave EIKOnal approximation `DWEIKO` can be used [Ber99, Ber]. It solves the differential equations in Equation (2.18) in straight-line approximation. Additionally, an approximate treatment of nuclear interactions is also included in the framework. However, for all performed calculations in this work, nuclear influences on the scattering process were neglected.

2.2. Nuclear Structure Observables

Although (reduced) matrix elements cannot be accessed directly in nuclear structure experiments, other measurable quantities are physically linked to them. Such a property is, e.g., the mean lifetime τ of a nuclear state J_n with respective transition energy E_γ. From its knowledge, the total decay width of the respective transition $J_n^{\pi_n} \to J_m^{\pi_m}$ can be deduced via

$$\Gamma_{\text{tot}} = \frac{\hbar}{\tau}. \tag{2.34}$$

Due to selection rules related to parity [Suh07]

$$\pi_\gamma = \pi_n\pi_m = \begin{cases} (-1)^\lambda, & \text{for electric character } (\sigma = E), \\ (-1)^{\lambda+1}, & \text{for magnetic character } (\sigma = M), \end{cases} \tag{2.35}$$

and angular momentum

$$|J_n - J_m| \leq \lambda \leq J_n + J_m, \tag{2.36}$$

multiple types of transitions can occur. Since all of those contribute to the total decay width,

$$\Gamma_{\text{tot}} = \sum_{i=1}^{N} \Gamma(\sigma_i, \lambda_i) \tag{2.37}$$

holds, where N is the total amount of possible transition types from J_n to J_m and $\Gamma(\sigma_i, \lambda_i)$ is the respective decay width for a certain set of σ and λ. Each decay width is related to the so-called reduced transition strength [Suh07]

$$B(\sigma\lambda; J_n \rightarrow J_m) = \frac{1}{2J_n + 1} \left| \langle J_m || \mathscr{M}(\sigma\lambda) || J_n \rangle \right|^2 , \tag{2.38}$$

via

$$\Gamma(\sigma\lambda) = 8\pi \frac{\lambda + 1}{\lambda[(2\lambda + 1)!!]^2} \left(\frac{E_\gamma}{\hbar c} \right)^{2\lambda+1} B(\sigma\lambda; J_n \rightarrow J_m) . \tag{2.39}$$

Hence, from the knowledge of so-called multipole mixing ratios δ with [Suh07]

$$\delta^2 = \frac{\Gamma(\sigma_i \lambda_i)}{\Gamma(\sigma_j \lambda_j)} , \tag{2.40}$$

comparing the relative decay probabilities of two sets $\sigma_i\lambda_i$ and $\sigma_j\lambda_j$ of possible transition types, the respective decay widths $\Gamma(\sigma_i\lambda_i)$ can be obtained from Γ_{tot} and used to calculate the reduced matrix elements $\langle J_m || \mathscr{M}(\sigma\lambda) || J_n \rangle$ via Equation (2.38). Multipole mixing ratios can, e.g., be obtained from angular correlations between emitted γ-rays [Rai06] or from internal conversion data [Löb72]. An additional method to calculate $E2/M1$ multipole mixing ratios is presented in Chapter 4.

2.3. Doppler Shift and Lorentz Boost

Since a majority of nuclear structure experiments are performed at relativistic conditions, γ rays that are emitted from the moving beam particles, after, e.g., a CoulEx, are subject to different types of relativistic effects, namely Doppler shift of the γ-ray energies as well as a Lorentz boost of the emission direction of the γ rays.

Doppler Shift

Depending on the polar angle α of emission between a γ ray and the traveling direction of its respective beam particle, the measurable energy of said γ ray is Doppler-shifted via

$$E'_\gamma = E_\gamma \frac{\sqrt{1-\beta^2}}{1-\beta\cos\alpha}\,, \tag{2.41}$$

where $\beta = v/c$ with the velocity of the beam v and the speed of light c.

Lorentz Boost

In addition to a different energy, the original angle of emission θ_γ of the γ ray in its center-of-mass frame is shifted due to Lorentz contraction. Given the angle of the recoiling nucleus relative to its original direction of motion in the laboratory frame ϑ_N, its azimuth φ_N and similarly for the emitted γ ray ϑ_γ and φ_γ, the Lorentz-boosted angles of the γ ray in the center-of-mass frame are given by

$$\cos\theta_\gamma = \frac{\cos\vartheta_\gamma - \cos\vartheta_N\,[\beta\gamma - (\gamma-1)\cos\alpha]}{\gamma\,(1-\beta\cos\alpha)}\,, \tag{2.42}$$

$$\tan\phi_\gamma = \frac{\sin\vartheta_\gamma\sin\varphi_\gamma - \sin\vartheta_N\sin\varphi_N\,[\beta\gamma - (\gamma-1)\cos\alpha]}{\sin\vartheta_\gamma\cos\varphi_\gamma - \sin\vartheta_N\cos\varphi_N\,[\beta\gamma - (\gamma-1)\cos\alpha]}\,, \tag{2.43}$$

with the Lorentz-factor $\gamma = (1-\beta^2)^{-1/2}$. Under the assumption that the beam is traveling along the z-axis, it follows that

$$\theta_N = \vartheta_N = 0\,, \tag{2.44}$$

$$\alpha = \vartheta_\gamma\,, \tag{2.45}$$

yielding

$$\theta_\gamma = \arccos\left(\frac{\cos\alpha - \beta}{1-\beta\cos\alpha}\right), \tag{2.46}$$

$$\phi_\gamma = \varphi_\gamma\,. \tag{2.47}$$

The Lorentz boost of the emission angle of γ rays for isotropically distributed angles in the center-of-mass frame is depicted in Figure 2.2.

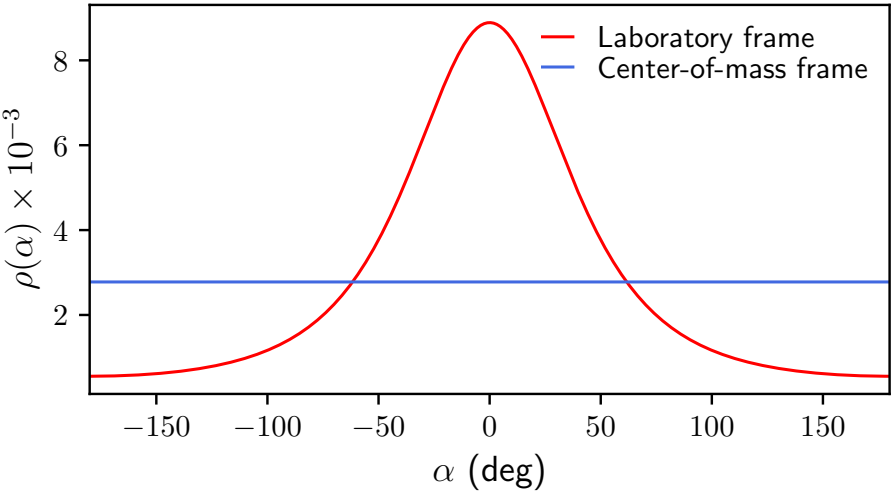

Figure 2.2.: Probability density $\rho(\alpha)$ of isotropically emitted γ rays in the center-of-mass frame (blue) and in the laboratory frame (red) for $\beta = 0.6$. It is assumed that the emitting nuclei move along the z-axis.

2.4. Competitive Double γ ($\gamma\gamma/\gamma$) Decay

In the following, a brief introduction to the theory of the competitive double γ ($\gamma\gamma/\gamma$) decay is given using the already observed $\gamma\gamma/\gamma$ decay in ^{137}Ba [Wal15] as an example case.

The γ decay is the most prominent type of decay in nuclear physics. It can occur in practically all nuclei and is a major tool for accessing the underlying structure of any particular nucleus of interest. Since the γ decay is only a first-order process of a transition from the initial state $|i\rangle$ to the final state $|f\rangle$, quantum electrodynamics suggest the existence of next-to-leading order transition processes. The next order process for the $|i\rangle \rightarrow |f\rangle$ transition is the $\gamma\gamma$ decay [Göp30, Fri75, Kra87]. It is a second order process in which two γ rays are emitted in the decay process instead of a single one. The Hamiltonian of such a decay, describing the interaction

between a nucleus and the electromagnetic field can be expressed (in Gaussian units $\hbar = c = 1$ and $\alpha = e^2$) via [Kra87]

$$H_{\text{int}} = \int \mathrm{d}^3x\, j_\mu(x) A^\mu(x) + \frac{1}{2} \int \mathrm{d}^3x\, \mathrm{d}^3y\, B_{\mu\nu} A^\mu(x) A^\nu(y)\,, \tag{2.48}$$

with $j_\mu(x) = [\rho(x), \vec{j}(x)]$ as the current operator, where $\rho(x)$ is the charge density and $\vec{j}(x)$ is the current density, and $A^\mu(x)$ as the vector potential. In addition, $B_{\mu\nu}$ is the so-called *seagull* operator. It essentially represents a sum over high-mass states containing virtual nucleon-antinucleon pairs. A full description of the seagull operator would exceed the scope of this work. The reader is therefore referred to [Kra87]. Additionally, for any electromagnetic transition, the parity selection rule

$$(-1)^{L+S+L'+S'} = \pi_i \pi_f\,, \tag{2.49}$$

where π_i and π_f are the parity quantum numbers of the initial and final state, L and L' are the mulitpolarities and their respective transition characters S and S' (for E: $S = 0$ and for M: $S = 1$) of both virtual transitions, as well as the spin selection rules

$$\begin{aligned} |I_i - I_f| \leq J \leq |I_i + I_f|\,, \\ |L - L'| \leq J \leq |L + L'|\,, \end{aligned} \tag{2.50}$$

with J as the coupling of angular momentum of the two photons, must be obeyed. Hence, for the case of the $\gamma\gamma$ decay of ^{137}Ba, only the following multipolarities are possible. Starting from the β^- decay of ^{137}Cs, the $1h^-_{11/2}$ state of ^{137}Ba is predominantly populated. It γ-decays via emission of a photon with an energy of $E_\gamma = 661.7\,\text{keV}$ to the $2d^+_{3/2}$ ground state. Given the spins of the two states, the possible multipolarities are $J = 4, 5, 6$ and 7. In first-order approximation, it is sufficient to constrain the multipolarity to $J = 4$, yielding $E1M3$, $E3M1$ and $M2E2$ as possible combinations of $\gamma\gamma$ transitions [Wal14] (see also Fig. 2.3). Applying second-order perturbation theory on the first term in Equation (2.48) as well as first-order perturbation theory on the second term, calculations – which are not shown in this work (see [Kra87]) – yield the differential decay probability for the $1h^-_{11/2} \rightarrow 2d^+_{3/2}$ transition via a $\gamma\gamma$ decay, given by [Wal15] (supplementary

material)

$$\frac{\mathrm{d}^5\Gamma_{\gamma\gamma}}{\mathrm{d}\omega\mathrm{d}\Omega\mathrm{d}\Omega'} = \frac{\omega\omega'}{96\pi^3} \sum_{\substack{S_1L_1S_1'L_1' \\ S_2L_2S_2'L_2' \\ J}} P_J'(S_1L_1, S_1'L_1', \omega\omega') P_J'(S_2L_2, S_2'L_2', \omega\omega') \sum_l a_l^{J\xi} P_l(\cos\theta)\,, \tag{2.51}$$

with the parameter ξ describing the full set of transition characters and multipolarities $\{S_1L_1S_1'L_1', S_2L_2S_2'L_2'\}$ of both γ rays, the Legendre polynomials $P_l(\cos\theta)$ of the angle θ between the emitted γ rays and parameters $a_l^{J\xi}$ from angular momentum coupling given in [Wal15] (supplementary material). In addition, the energies of the emitted γ rays in the $\gamma\gamma$ decay are ω and ω' with $\omega + \omega' = E_\gamma$. The so-called generalized polarizabilities are given by [Wal15] (supplementary material)

$$\begin{aligned} &P_J'(SL, S'L', \omega\omega') = \\ &\quad (-1)^{S+S'} 2\pi (-1)^{I_i+I_f} \omega^L \omega'^{L'} \frac{\sqrt{(2L+1)(2L'+1)}}{(2L+1)!!(2L'+1)!!} \sqrt{\frac{L+1}{L}\frac{L'+1}{L'}} \\ &\quad \times \sum_n \left[\begin{Bmatrix} L & L' & J \\ I_f & I_i & I_n \end{Bmatrix} \alpha_{SLS'L'}(\omega, n) + (-1)^{L+L'+J} \begin{Bmatrix} L' & L & J \\ I_f & I_i & I_n \end{Bmatrix} \alpha_{S'L'SL}(\omega', n) \right], \end{aligned} \tag{2.52}$$

with

$$\alpha_{SLS'L'}(\omega, n) = \frac{\langle I_f || i^{L'-S'} \mathscr{M}(S'L') || I_n \rangle \langle I_n || i^{L-S} \mathscr{M}(SL) || I_i \rangle}{E_n - E_i + \omega}\,. \tag{2.53}$$

Here, $\{\cdots\}$ describes the Wigner $6-j$ symbol [Suh07]. The total contribution of a certain multipolarity $SLS'L'$ is given by

$$\alpha_{SLS'L'}(\omega) = \sum_n \alpha_{SLS'L'}(\omega, n)\,. \tag{2.54}$$

Hence, the values $\alpha_{SLS'L'}(\omega)$ parameterize the probability of the $\gamma\gamma$ decay of the $I_i \to I_f$ transition via the transition characters and multipolarities $SLS'L'$. For the case of ^{137}Ba, these parameters are shown in Figure 2.3.

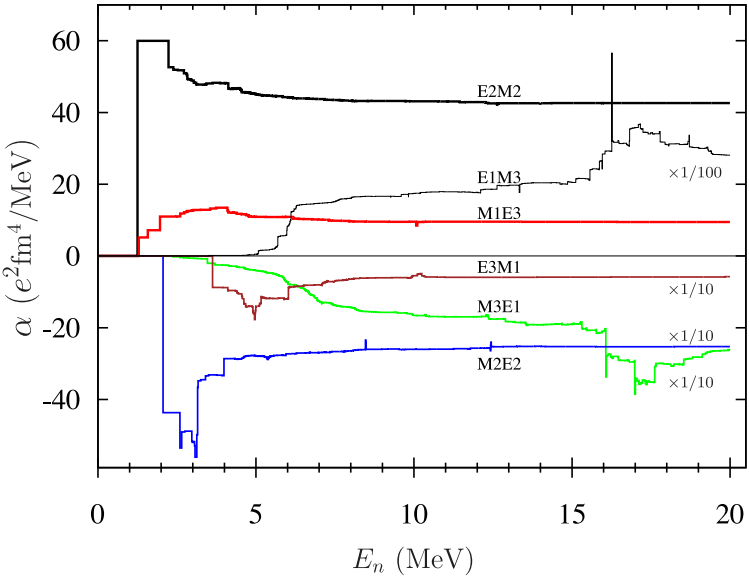

Figure 2.3.: Calculated parameters α (see Eq. (2.54)) for various $\gamma\gamma$-decay transitions in ^{137}Ba as a running sum of the energy E_n of the included levels. The value of α at 20 MeV marks the final value of α. The mentioned $E3M1$ and $M2E2$ transitions correspond to the $E2M2$ and $M1E3$ curves in the presented figure. Reprinted by permission from the Springer Nature Customer Service Centre GmbH: Nature [Wal15] (supplementary material), Copyright (2015). Figure slightly modified.

Via successful measurements of $\gamma\gamma$ decay, it would be possible to access nuclear properties encoded in the generalized polarizabilities P'_J, as it has already been performed in other types of experiments for the diagonal electric dipole polarizability of the ground state defined by [Kra87, RN10]

$$\alpha_{E1} = \frac{8\pi}{9} \sum_n \frac{\left|\langle 0_1^+ || i\mathscr{M}(E1) || 1_n^- \rangle\right|^2}{E_n} \tag{2.55}$$

which can be used to access, e.g., information about the neutron skin thickness in nuclei [RN10, Bir17]. To gain access to the generalized polarizabilities, a measurement of the total decay probability as well as angular and energy-correlations between the emitted γ rays of the $\gamma\gamma$ decay would be necessary. To calculate the total decay probability, integrations over the spatial angle set Ω and Ω' as well as the respective energies ω need to be performed

$$\Gamma_{\gamma\gamma} = \frac{1}{2}\int_0^{E_\gamma} \mathrm{d}\omega \int_{\Omega'} \mathrm{d}\Omega' \int_{\Omega} \mathrm{d}\Omega \, \frac{\mathrm{d}^5\Gamma_{\gamma\gamma}}{\mathrm{d}\omega \mathrm{d}\Omega \mathrm{d}\Omega'} \,. \tag{2.56}$$

Integration over Ω and Ω' of Equation (2.51) for one set of multipolarities L, S and L', S' in addition to the assumption of large differences in level energies E_i and E_n where $E_n - E_i + \omega$ can be approximated via

$$E_n - E_i + \omega \approx E_i - E_n - \frac{E_\gamma}{2} =: \Delta E \,, \tag{2.57}$$

yields [Wal14]

$$\begin{aligned} \frac{\mathrm{d}\Gamma_{\gamma\gamma}}{\mathrm{d}\omega} \approx & \frac{\langle I_f || i^{L'-S'} \mathscr{M}(S'L') || I_n \rangle^2 \langle I_n || i^{L-S} \mathscr{M}(SL) || I_i \rangle^2}{\Delta E} \\ & \times \left[\omega^{2L+1} (E_\gamma - \omega)^{2L'+1} + \omega^{2L'+1} (E_\gamma - \omega)^{2L+1} \right] . \end{aligned} \tag{2.58}$$

As stated in [Wal14, Wal15] (see also Fig. 2.3), the branching ratios for $M2E2$ are approximately given by the $1h^-_{11/2} \to 1g^+_{7/2} \to 2d^+_{3/2}$ transition via

$$\frac{\Gamma_{\gamma\gamma}}{\Gamma_\gamma} = 4.58 \times 10^{-2} \frac{E_\gamma}{\Delta E} \alpha \frac{B(M2; 1h^-_{11/2} \to 1g^+_{7/2}) B(E2; 1g^+_{7/2} \to 2d^+_{3/2})}{B(M4; 1h^-_{11/2} \to 2d^+_{3/2})} \,. \tag{2.59}$$

For $E3M1$, the $1h^-_{11/2} \to 2d^+_{5/2} \to 2d^+_{3/2}$ transition is sufficient to calculate the branching ratio

$$\frac{\Gamma_{\gamma\gamma}}{\Gamma_\gamma} = 5.82 \times 10^{-2} \frac{E_\gamma}{\Delta E} \alpha \frac{B(E3; 1h^-_{11/2} \to 2d^+_{5/2}) B(M1; 2d^+_{5/2} \to 2d^+_{3/2})}{B(M4; 1h^-_{11/2} \to 2d^+_{3/2})} \,. \tag{2.60}$$

The calculated branching ratios are given in Table 2.1. These calculated values are only an estimate on the expected branchings which need to be accessed via

Table 2.1.: Calculated branching ratios $\Gamma_{\gamma\gamma}/\Gamma_{\gamma}$ of the $\gamma\gamma$ decay compared to the γ decay for the $E3M1$ and $M2E2$ transitions (adapted from [Wal14]).

	$E3M1$	$M2E2$	Sum
$\Gamma_{\gamma\gamma}/\Gamma_{\gamma}$	0.78×10^{-6}	1.28×10^{-6}	2.06×10^{-6}

measurements. To access the branching ratios in addition to potentially gaining knowledge about nuclear properties, measurements of angular distributions as well as energy distributions can be used. For angular distributions, all l-dependent properties in Equation (2.51) have to be considered. For $E3M1$, the angular distribution is given by [Wal14]

$$W(\theta) = 1 - \frac{1}{8} P_2(\cos\theta), \tag{2.61}$$

as well as for $M2E2$ by

$$W(\theta) = 1 + \frac{5}{49} P_2(\cos\theta) + \frac{40}{441} P_4(\cos\theta). \tag{2.62}$$

Both distributions are depicted in Figure 2.4 (left). In addition to angular distributions, the energy distributions of the emitted photons is also influenced by the decay behavior. In the case of $E3M1$ transitions (see Eq. (2.58)),

$$\frac{\mathrm{d}\Gamma_{\gamma\gamma}}{\mathrm{d}\omega} \propto \omega^3 (E_\gamma - \omega)^7 + \omega^7 (E_\gamma - \omega)^3 \tag{2.63}$$

and for $M2E2$ transitions

$$\frac{\mathrm{d}\Gamma_{\gamma\gamma}}{\mathrm{d}\omega} \propto \omega^5 (E_\gamma - \omega)^5 . \tag{2.64}$$

The energy distributions are also shown in Figure 2.4 (right) as probability densities $\rho(\omega)$. The assumed independence of ΔE of the energy ω is only valid for large single particle excitation energy differences $E_i - E_n$. For small values of ΔE, deviations from the mentioned behavior depicted in Figure 2.4 are anticipated. Only ω is described here since $\omega' = E_\gamma - \omega$.

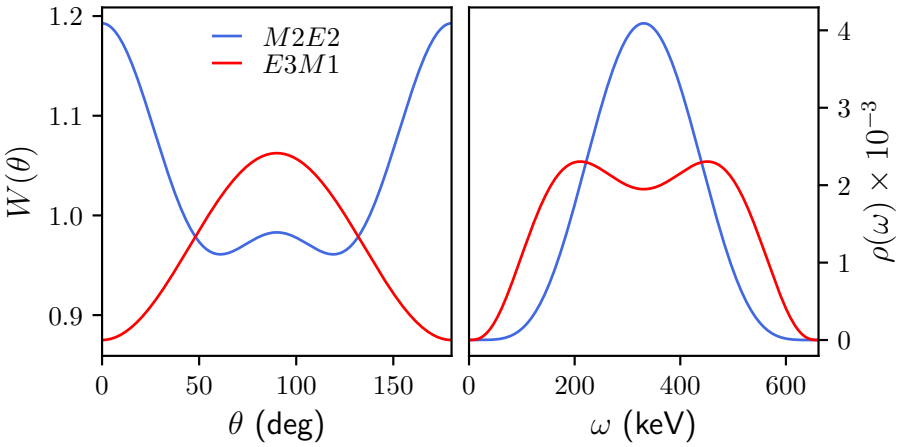

Figure 2.4.: *Left*: Angular distributions between the two emitted γ rays for the $M2E2$ transition (blue) and the $E3M1$ transition (red). *Right*: Probability densities $\rho(\omega)$ of the emitted γ ray energy ω for the respective transition types (same color code as in $W(\theta)$) were calculated via Equations (2.63) and (2.64).

First Experimental Observation

The first observation of the $\gamma\gamma/\gamma$ decay was achieved in the nucleus ^{137}Ba in 2015. The setup consisted of five $LaBr_3$(Ce) assembled in a star-shaped configuration (see Fig. 2.5). The time differences between two detectors were used to determine, whether the measured energies in said detectors stem from a single photon being Compton-scattered between the detectors, or two photons from the $\gamma\gamma$ decay were emitted at the same time and photo-absorbed in the two detectors. The measured branching ratio of $\gamma\gamma$ events to γ events is [Wal15]

$$\frac{\Gamma_{\gamma\gamma}}{\Gamma_{\gamma}} = 2.05(37) \times 10^{-6}\,. \tag{2.65}$$

However, due to the angular limitations of the experimental setup, angular correlations have only been measured for two different angles $\theta_1 = 72°$ and $\theta_2 = 144°$.

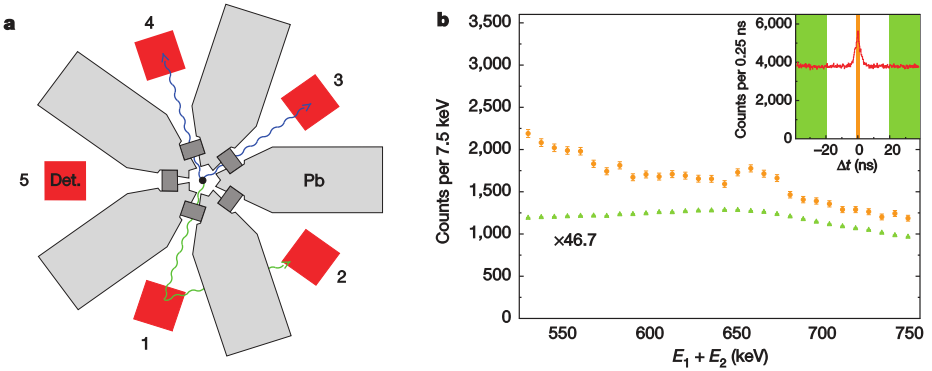

Figure 2.5.: Setup of the experiment observing the $\gamma\gamma/\gamma$ in ^{137}Ba for the first time. Five $LaBr_3$(Ce) aligned in a star-shaped configuration were used (see (a)). The observed $\gamma\gamma$ decay γ rays that add up to 661.7 keV with very small time differences are shown in (b). Reprinted by permission from the Springer Nature Customer Service Centre GmbH: Nature [Wal15], Copyright (2015).

2.5. Mathematical Prerequisites

Over the course of this work, mathematical constructs such as probability densities and random number generation from arbitrary probability densities are used. These concepts are briefly presented in the following.

2.5.1. Probability Space and Density

To get a general definition of a probability space, the definition of the so-called σ-algebra is helpful.

σ-algebra

Let Ω be a non-empty set. A set $\mathscr{A}$ of subsets of the sample space Ω is called *σ-algebra* over Ω, if [EK17]

1. $\emptyset \in \mathscr{A}$ and $\Omega \in \mathscr{A}$.
2. From $A \in \mathscr{A}$ follows $A^c := \Omega \setminus A \in \mathscr{A}$.
3. From $A, B \in \mathscr{A}$ follows $A \cup B \in \mathscr{A}$, $A \cap B \in \mathscr{A}$ and $A \setminus B \in \mathscr{A}$.
4. If $A_1, A_2, \cdots \in \mathscr{A}$, so $\bigcup_{n=1}^{\infty} A_n$ and $\bigcap_{n=1}^{\infty} A_n \in \mathscr{A}$.

Via the σ-algebra, one can define a general description of a probability space.

Probability Space

Let Ω be a non-empty set and $\mathscr{A}$ be a σ-algebra over Ω. A mapping $P : \mathscr{A} \to \mathbb{R}$ is called *probability measure*, if [EK17]:

1. $P(A) \in [0, 1]$ for all $A \subseteq \Omega$.
2. $P(\emptyset) = 0$ and $P(\Omega) = 1$.
3. For all $A \in \mathscr{A}$

$$P(A^c) = 1 - P(A). \tag{2.66}$$

4. For all $A, B \in \mathscr{A}$ with $A \subseteq B$

$$P(A) \leq P(B)\,. \tag{2.67}$$

5. For all $A, B \in \mathscr{A}$ with $A \cap B = \emptyset$

$$P(A \cup B) = P(A) + P(B)\,. \tag{2.68}$$

6. For all $A_1, A_2, \ldots, A_n \in \mathscr{A}$ with $A_i \cap A_j = \emptyset$ for all $i \neq j$

$$P\left(\bigcup_{k=1}^{n} A_k\right) = \sum_{k=1}^{n} P(A_k)\,. \tag{2.69}$$

7. For all $A_1, A_2, \cdots \in \mathscr{A}$ with $A_i \cap A_j = \emptyset$ for all $i \neq j$

$$P\left(\bigcup_{k=1}^{\infty} A_k\right) = \sum_{k=1}^{\infty} P(A_k)\,. \tag{2.70}$$

In this case, $(\Omega, \mathscr{A}, P)$ is called *probability space*. All sets $A \in \mathscr{A}$ are called *events* and $P(A)$ is called the *probability* of event $A \in \mathscr{A}$.

To obtain a sensible description of a so-called probability density, all following definitions are based on the Borel σ-algebra.

Borel σ-algebra

Let $\Omega = \mathbb{R}^n$ and

$$G = \left\{ \prod_{i=1}^{n} [a_i, b_i] : a_i < b_i;\ a_i, b_i \in \mathbb{Q} \right\}, \tag{2.71}$$

be a system containing all rectangular boxes in $\mathbb{R}^n$ with rational vertices and edges parallel to the axes. The system $\mathscr{B}^n = \sigma(G)$, the σ-algebra over set G, is called *Borel σ-algebra* in $\mathbb{R}^n$. From the definition follows that every open and closed set $A \subset \mathbb{R}^n$ is a *Borel set*. For the proof and further details on Borel sets and σ-algebras, the reader is referred to [Geo07, Els18].

Using the definition of the probability space, assuming that the sample space Ω is equal to $\mathbb{R}$ and the definition of the Borel σ-algebra, a probability density can be defined.

Probability Density

Let $\rho : \mathbb{R} \to \mathbb{R}$ be a mapping with

$$\rho(x) \geq 0\,, \quad \text{for all } x \in \mathbb{R}\,, \quad \text{and} \quad \int_{\mathbb{R}} \mathrm{d}x\, \rho(x) = 1\,. \tag{2.72}$$

Via the sample space $\Omega = \mathbb{R}$ and σ-algebra $\mathscr{B}$, the probability space $(\mathbb{R}, \mathscr{B}, P)$ is defined, where

$$P(A) = \int_A \mathrm{d}x\, \rho(x)\,, \quad \text{with} \quad A \in \mathscr{B}\,, \tag{2.73}$$

is defined as a probability measure P. The function ρ is called *probability density* of the probability measure P. Since the probability measure P can also be viewed as a sum over all densities $\rho(x')$ from $-\infty$ to x, $P(-\infty, x)$ is also often referred to as the *cumulative distribution function* (CDF) of the probability density function (PDF) ρ. If not stated otherwise, functions denoted as $\rho(x)$ are always considered as PDFs in the following.

2.5.2. Sampling via Arbitrary Probability Densities

Via the definition of the CDF, a so-called random variable can be defined.

Random Variable

Let Ω' be a non-empty set and $\mathscr{A}'$ a σ-algebra over Ω'. Then $(\Omega', \mathscr{A}')$ is called *measurable space*. Now, let $(\Omega, \mathscr{A}, P)$ be a probability space and let $(\Omega', \mathscr{A}')$ be a measurable space. Then, every mapping $X : \Omega \to \Omega'$ with

$$X^{-1}(A') := \left\{\omega \in \Omega : X(\omega) \in A'\right\} \in \mathscr{A} \quad \text{for all} \quad A' \in \mathscr{A}'\,, \tag{2.74}$$

is called *random variable*. If $\Omega' = \mathbb{R}$ and $\mathscr{A}' = \mathscr{B}$, X is called *real random variable*. If $X : \Omega \to \Omega'$ is a random variable, $(\Omega', \mathscr{A}', P_X)$ is a probability space with

$$P_X(A') := P(X^{-1}(A')) = P\left(\left\{\omega \in \Omega : X(\omega) \in A'\right\}\right)\,, \tag{2.75}$$

where the probability measure P_X is the CDF of random variable X. For simplicity, a random variable X with CDF $\mathscr{Y}(a,b)$, where $\Omega = [a,b]$ defines the sample space, is written as

$$X \sim \mathscr{Y}(a,b)\,, \tag{2.76}$$

from this point on. CDFs used in the following are the unitary distributed CDF $\mathscr{U}(a,b)$ with $-\infty < a < b < \infty$ defined via the PDF [EK17]

$$\rho(x) = \begin{cases} \frac{1}{b-a}\,, & \text{if} \quad a \leq x \leq b\,, \\ 0\,, & \text{if} \quad x < a \vee x > b\,, \end{cases} \tag{2.77}$$

as well as the normal distribution $\mathscr{N}(\mu,\sigma)$ with $\mu \in \mathbb{R}$ and $\sigma \in \mathbb{R}_+$ defined by the PDF

$$\rho(x) = \frac{1}{\sqrt{2\pi}\sigma} \exp\left(-\frac{(x-\mu)^2}{2\sigma^2}\right). \tag{2.78}$$

Arbitrarily Sampled Random Numbers

To numerically sample a random number X from any invertible CDF $\mathscr{Y}$, the following theorem can be used (see [Mül12] for details).

Let $X \sim \mathscr{F}$ be a random variable with invertible CDF $\mathscr{F}$ and an additional random variable $U \sim \mathscr{U}(0,1)$. It follows

$$P(\mathscr{F}^{-1}(U) \leq x) = P(U \leq \mathscr{F}(x)) \equiv \mathscr{F}(x)\,. \tag{2.79}$$

Hence, the random variable $Y = \mathscr{F}^{-1}(U)$ has $\mathscr{F}$ as its CDF. As an example case, the mentioned procedure for sampling $Y \sim \mathscr{F}(0,\infty)$ with the CDF $\mathscr{F}(0,x) = 1 - \exp(-x)$ using $U \sim \mathscr{U}(0,1)$ is shown in Figure 2.6.

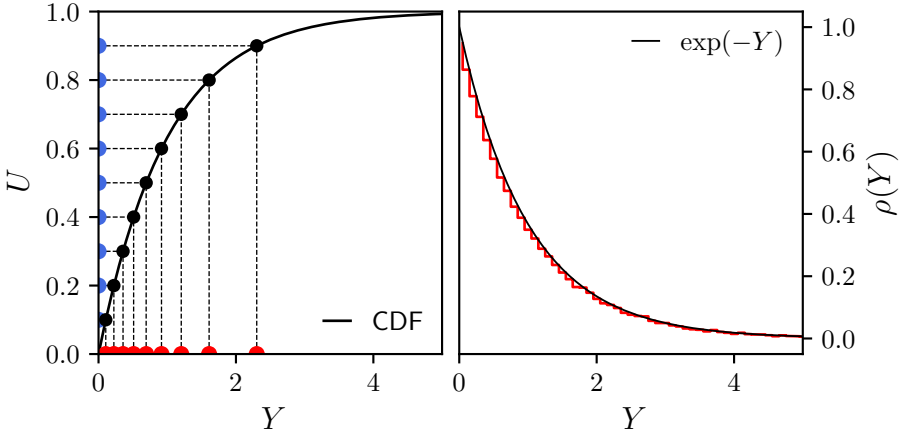

Figure 2.6.: Procedure for sampling $Y \sim 1 - \exp(-x)$ via $U \sim \mathcal{U}(0,1)$ (left). For each U, the value $Y = \mathcal{F}^{-1}(U)$ is calculated. The resulting distribution of Y then follows the desired CDF $\mathcal{F}(0,x)$ (see right).

3. Advanced GAmma Tracking Array

AGATA is the European version of a new state-of-the-art γ-spectrometer type – large high-purity germanium detector γ-ray tracking arrays. In the following, the evolution of γ-detector arrays is presented briefly. The general working principle of High-Purity Germanium (HPGe) detectors as well as novel abilities of position resolution of these detectors via Pulse Shape Analysis (PSA) are elaborated. In addition, the principle of γ-ray tracking, different approaches to γ-ray tracking as well as different kinds of tracking algorithms developed in the past such as the *Orsay Forward Tracking* (OFT) [Lop04, KL19] and the *Mars Gamma-ray Tracking* (MGT) [Baz04, KL19] are presented.

3.1. High Purity Germanium Detector Arrays

Due to the high energy resolution of HPGe detectors [Leo94], it became the standard detector type for γ-spectroscopy experiments. To increase the amount of sensitive material, large arrays of HPGe detectors were built. To decrease the Compton-scattering induced background in the measured γ-ray spectra, Compton-suppression measures were taken in the form of scintillation veto-detectors. The most prominent examples of such Compton-suppressed detector arrays are Gammasphere [Lee90] and Euroball [Sim97]. A technical drawing of Gammasphere is shown in Figure 3.1. Here, γ rays that deposited some energy in a HPGe detector but are Compton-scattered into the bismuth germanate $Bi_4Ge_3O_{12}$ (BGO) scintillation detectors are not taken into account. Since the total volume of HPGe material is small compared to the total detector volume, the γ-ray detection efficiency is only in the range of $\epsilon \leq 10\,\%$. However, the achievable peak-to-total ratio is in the range of 65 % [Lee90].

To achieve larger γ-ray detection efficiencies, a larger HPGe detector volume is needed. However, in the case of a complete shell covering a solid angle of 4π, the

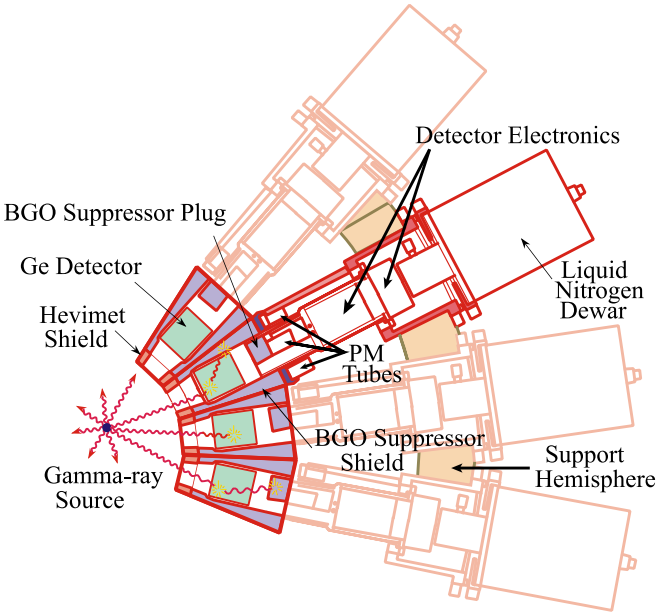

Figure 3.1.: Schematic drawing of Gammasphere. Only events without any veto signal from the respective BGO suppressor shields and plugs are analyzed further. Reprinted from [ES08], Copyright (2008), with permission from Elsevier, and slightly modified.

distinction between multiple γ rays interacting with the detector is non-trivial. To account for this problem, a large amount of very small HPGe detectors could be used – reducing the probability of two γ rays interacting with the same detector at the same time[1] to practically zero. However, such an approach is not justifiable financially.

In detector arrays without any Compton-suppression measures, so-called add-back can be used, a procedure in which the sum of all (or a certain subset) measured deposited energies are added up to assign the energies of the incident γ rays, potentially yielding a larger detection efficiency. However, such add-back

[1] within the time resolution of the HPGe detectors

procedures can also yield falsely assigned γ-ray energies, especially in the case of a high amount of incident γ rays. Since the dynamics of Compton scattering are well understood, mathematical approaches to reconstruct the γ ray paths in the detector can be conceptualized – yielding to so-called γ-ray tracking detector arrays.

3.2. Technical Demands for γ-ray Tracking Arrays

To analyze the possible paths of γ rays in matter with regards to Compton scattering, the two major contributions to a successful reconstruction are the deposited energy of a photon and the exact position of interaction. Since a high energy resolution is the major strength of HPGe detectors, no new inventions have to be made in this regard. However, so far the position resolution was restricted by the assumption that the interaction occurred, e.g., at the center of the involved detector. This is not sufficient to reconstruct the γ-ray paths with high accuracy. A first approach to improve position resolution was performed with the MINIBALL HPGe detector array which consists of 40 HPGe detectors that are sixfold electrically segmented [Wei03], allowing for a reconstruction on a sub-segment level via PSA.

3.2.1. Pulse Shape Analysis

The MINIBALL HPGe detectors are hexagonally shaped and sixfold segmented. All segments share the same core contact, the anode of the semiconductor. At the edge of each segment, the respective cathodes are situated, yielding a total of seven signals that need to be processed. Since HPGe detectors are in principal a diode operated in reverse bias mode [Leo94], ionizing radiation that interacts with the detector material will create many electron–electron-hole pairs (e^-h^+), due to the radiation's high energy compared to the bandgap of the semiconductor. Electron-holes are fictive particles resembling a positive particle with charge $+e$ that move across the detector due to neighboring electrons filling the gap of the h^+, resulting in the movement of h^+ across the diode towards the cathode (see Fig. 3.2). The amount of created e^-h^+ pairs is directly proportional to the incident energy of the ionizing radiation. The electrons and their respective electron-holes separate, building "charge clouds" that travel to the corresponding contacts. The

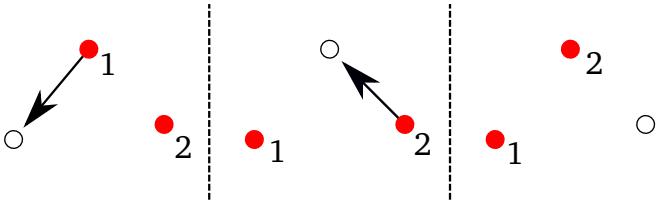

Figure 3.2.: “Movement” of electron-holes in a semi-conductor. The electrons (solid dots) fill the gap of the electron-hole (open circles) and leave an electron-hole behind.

charge clouds induce mirror charges in the anode and cathode, where the amount of induced mirror charges depends on the distance of the respective charge cloud to the anode or cathode. Since positive mirror charges are induced in the anode, this can be measured as a negative charge in the preamplifier due to electrons being drained from the anode during the approach of the electron charge cloud. Similarly, negative mirror charges are induced in the cathode by the h^+ cloud, yielding a measurable positive charge in the preamplifiers. The change of charge over time in the respective preamplifiers is measured as a voltage. In the example cases shown in Figure 3.3, the interaction points of the γ rays are depicted as red dots. On the left side, the proximity of the interaction point to the cathode causes a fast rise of the measured voltage in segment 4. In comparison, the rise time of the core signal increases more slowly since the electrons need some time to reach the anode. On the contrary, the interaction point on the right yields a fast rise in the core signal and a comparatively slow rise in the signal of segment 4.

In addition to the mirror charges induced in the cathodes and anode of the primary segment, mirror charges are also induced in the neighboring segments. However, since no charge clouds have been created in these segments, the measured signals will return to the baseline level when the primary charges are completely depleted. From the respective heights of the neighboring segment signals, the proximity of the primary interaction can be inferred. If the primary interaction was close to the respective neighbor, a large amount of mirror charges are induced (see, e.g., Fig. 3.3, segment 3). In addition, if the primary interaction was close to the anode, the electrons are collected fast by the anode, leaving only the electron-holes on their path to the cathode. This causes negative mir-

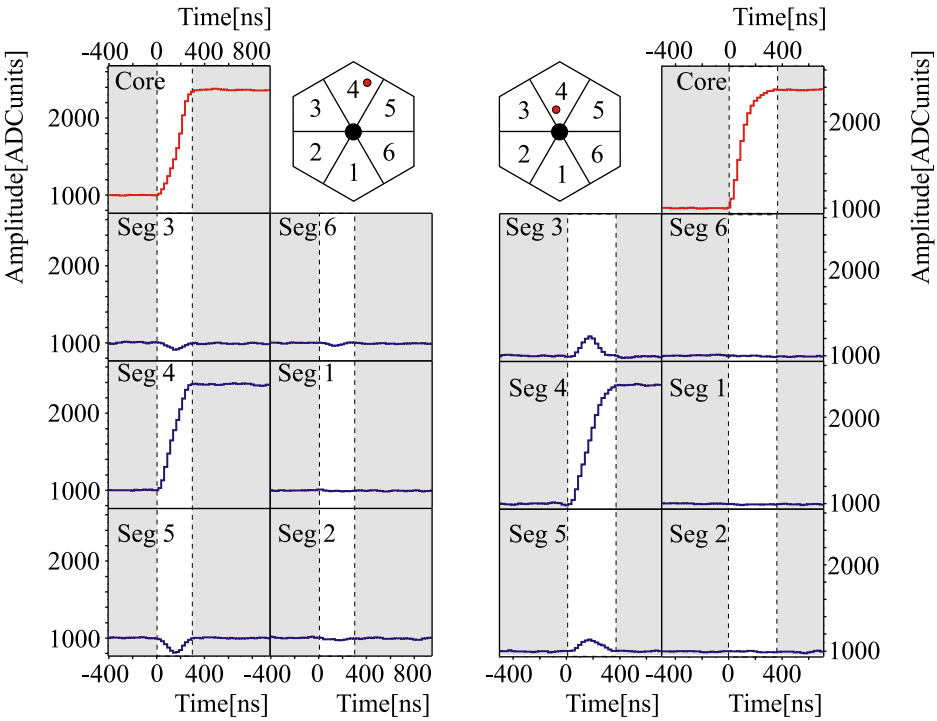

Figure 3.3.: Schematics of measured pulse shapes by a MINIBALL detector for γ-ray interactions in segment 4. From the rise time of the core signal and the primary segment signal in addition to the signal shapes in the neighboring segments due to induced mirror charges, the interaction point of the γ ray can be inferred. See text for details. The picture was adapted from and modified in [Sta15a], originally from [Wei03].

ror charges to be induced on the neighboring segment cathodes, measured as a positive charge in the preamplifiers. If the primary interaction is close to the cathode, only electrons remain, yielding positive mirror charges in the neighboring segment cathodes measured as negative charges in the preamplifier.

Hence, from the comparison of rise times in the primary segment, the radial

component of the interaction point can be inferred. In addition, the angular information can be deduced from the analysis of all neighboring segment signals.

The determination of the interaction point is usually performed by PSA algorithms that compare the measured signals to calculated ones. These calculations were performed via electromagnetic simulations of the detectors [Bru16, Sch11b]. Prominent examples for PSA algorithms are the adaptive grid search algorithm [VB04], the fully-informed particle-swarm method [Sch11a] and the Matrix Method [Ola06].

Via PSA methods, the position resolution can be improved to roughly 5 mm FWHM [Rec09b, Söd11] which is far superior compared to the geometrical dimensions of the used detectors in the range of centimeters.

3.3. AGATA

In Europe, a γ-ray tracking array is realized within the large-scale AGATA project [Akk12]. In its finished form, it will consist of 180 hexagonally shaped HPGe detectors that are 36-fold segmented each. The geometrical properties of the detectors are depicted in Figure 3.4. The detectors are arranged in triple cluster. For each triple cluster, one cryostat is used for the cooling of the HPGe crystals with liquid nitrogen to strongly decrease the amount of leak currents caused by the low band gap of germanium. The formed sphere of all 60 triple clusters is interrupted by twelve pentagons (see Fig. 3.4) which are used for feed-through of the beam pipe and additional instrumentation for, e.g., the target chamber. From extensive Monte-Carlo simulation, the expected γ-ray detection efficiency lies in the range of $43-28\,\%$ and the expected peak-to-total ratio around $59-43\,\%$ for γ rays with an energy of 1 MeV and a multiplicity of incident γ rays of $1-30$ [Far10]. First experiments with the AGATA Demonstrator consisting of five triple clusters were performed at the Laboratori Nazionali di Legnaro LNL [Gad11] in late 2010 with huge success [Sta15c, Vog15, Vog17, Joh14, Joh17, Kay19]. The PreSPEC campaign at GSI Helmholtzzentrum für Schwerionenforschung from 2012-2014 [Pie14, Clé18] used additional AGATA detectors totaling to 21 used in experiment S426, analyzed in Chapter 4. Successful experiments of the PreSPEC campaign, e.g, focused on the isobaric multiplet ^{46}Cr—^{46}V—^{46}Ti [Bos19] or lifetime measurements in even-even Mb isotopes [Ral17a]. At the moment, AGATA is

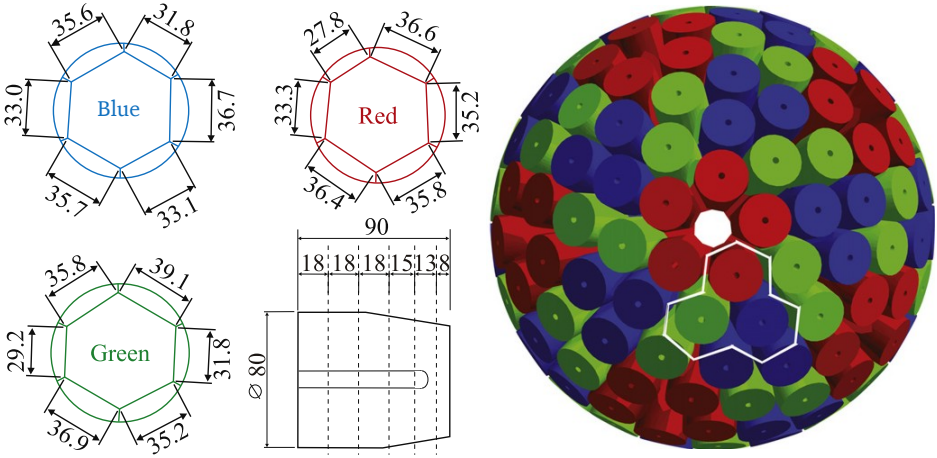

Figure 3.4.: Geometrical properties of the 36-fold segmented HPGe detectors of AGATA (left) as well as AGATA's conceptualized 4π configuration (right). Pentagonal feed-throughs where five red detectors are adjacent to each other (see, e.g, white spot in sphere center). Pictures originally from [Akk12], modified by C. Stahl in [Sta15a] and slightly modified again.

based at the Grand Accélérateur National d'Ions Lourds (GANIL) facility in Caen, France. Many experiments have already been performed [Dud17, Ral17b] and it is planned to finish the AGATA 1π setup, consisting of a total of 45 detectors and covering a 1π solid angle [Clé17]. A return of AGATA to LNL in 2021 is planned.

3.4. γ-ray Tracking

In the following, the physical and mathematical foundations for γ-ray tracking are presented.

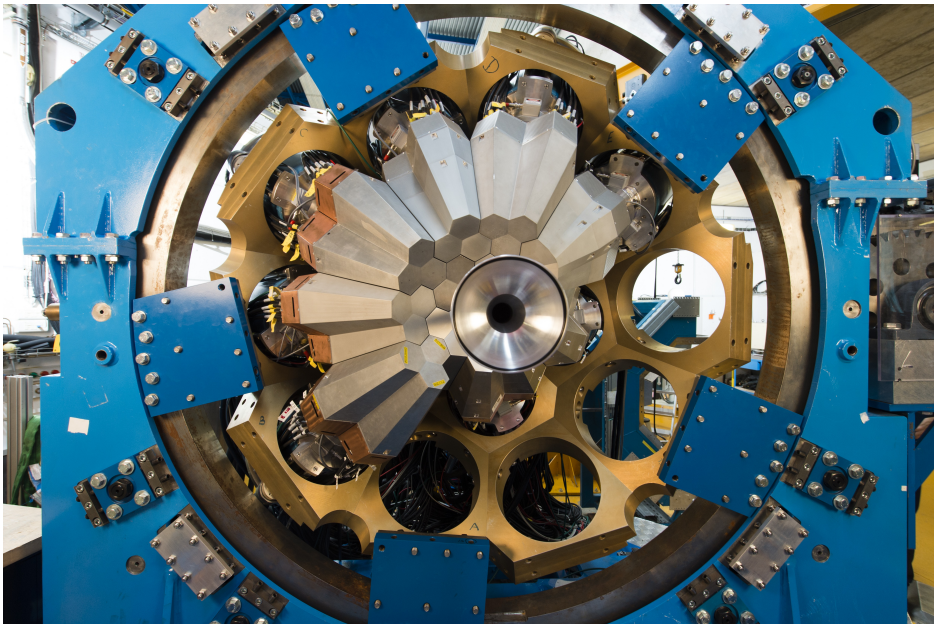

Figure 3.5.: AGATA at GANIL in 2016. 35 detectors were mounted at that time. Picture by P. Stroppa, Centre de recherche CEA de Saclay, Paris.

3.4.1. Interaction of γ Rays with Matter

In the photon energy range relevant for γ-spectroscopy experiments with AGATA, three types of interactions of γ rays with matter govern. These are the photoelectric effect, the Compton effect and pair production. Depending on the incident photon energy E_γ, these processes vary in relative probability, mirrored by the respective cross sections depicted in Figure 3.6.

Photoelectric Effect

Dominating at low γ-ray energies, the photoelectric effect occurs when an incident γ ray is absorbed by an electron bound to an atom with binding energy W_A. The photon energy E_γ has to be larger than the electron's binding energy W_A. The

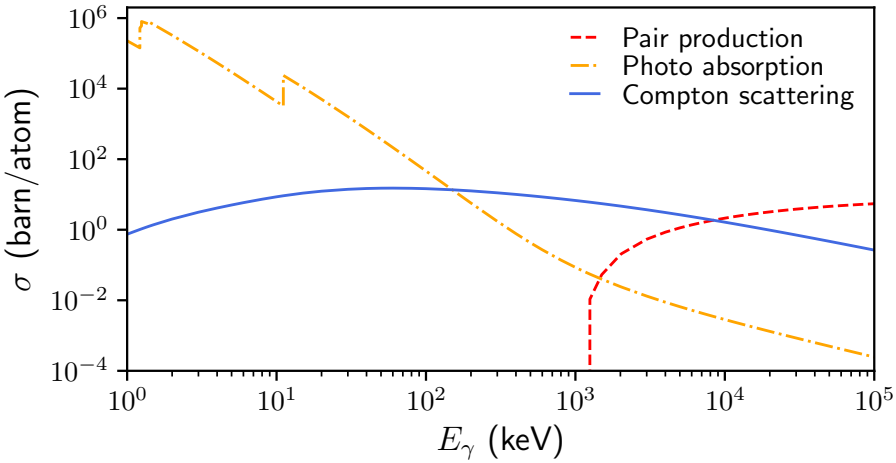

Figure 3.6.: Total cross section σ for the various interaction types of γ rays in germanium (photoelectric effect in orange, Compton effect in blue and pair production in red). The cross sections were extracted from the NIST XCOM database [Ber10].

kinetic energy of the electron after the absorption is [Kno00]

$$E_e = E_\gamma - W_A \,. \tag{3.1}$$

Since the binding energies are quantized due to the atomic shell structure, higher energetic γ rays can release electrons that are bound more strongly. The quantization yields to emerging steps in the total cross section with increasing γ-ray energy. In general, the total cross section of the photoelectric effect drops with increasing γ-ray energy (see Fig. 3.6).

Compton Effect

The Compton effect describes the inelastic scattering of a photon off an electron. Binding effects of the electron as well as Doppler-broadening of the γ-ray energies described in [Rib75, RB82, Bru96] are neglected for now. It is assumed that

the electron involved in the Compton-scattering process is unbound and at rest. During the scattering process, γ rays are not fully absorbed but only transfer a part of their energy to the electron. Given the Compton scattering angle θ between the directions of the incident and scattered photon, the energy of the γ ray after the scattering is given by [Kno00]

$$E'_\gamma = \frac{E_\gamma}{1 + \frac{E_\gamma}{m_e c^2}(1 - \cos\theta)}. \tag{3.2}$$

Here, m_e is the rest mass of the electron and c the speed of light in vacuum. The probability for a scattering by the angle θ as a function of incident photon energy is given by the *Klein-Nishina* double differential cross section [Hei60]

$$\frac{\mathrm{d}^2\sigma}{\mathrm{d}\phi\,\mathrm{d}\theta\,\sin\theta} = \frac{Z}{2} r_e^2 \left(\frac{E'_\gamma}{E_\gamma}\right)^2 \left(\frac{E'_\gamma}{E_\gamma} + \frac{E_\gamma}{E'_\gamma} - 2\sin^2\theta\cos^2\phi\right), \tag{3.3}$$

with the atomic charge number Z, the classical electron radius

$$r_e = \frac{1}{4\pi\epsilon_0}\frac{e^2}{m_e c^2} \approx 2.818\,\mathrm{fm}, \tag{3.4}$$

and the scattering angle ϕ between the incident photon's polarization plane and the direction of the scattered photon. Since γ-ray tracking is only sensitive on deposited energies and not directly on photon polarizations, the single differential Klein-Nishina cross section

$$\int_0^{2\pi} \mathrm{d}\phi\, \frac{\mathrm{d}^2\sigma}{\mathrm{d}\phi\,\mathrm{d}\theta\,\sin\theta} = Z\pi r_e^2 \left(\frac{E'_\gamma}{E_\gamma}\right)^2 \left(\frac{E'_\gamma}{E_\gamma} + \frac{E_\gamma}{E'_\gamma} - \sin^2\theta\right) \tag{3.5}$$

is sufficient to describe the Compton scattering behavior of γ rays. The single differential Klein-Nishina cross section is exemplary shown in Figure 3.7 for various incident photon energies in germanium. With increasing γ-ray energy, the probability for Compton scattering in forward direction increases as well.

e^-e^+ Pair Production

For large photon energies well above 1 MeV, the pair production is the dominating process (see Fig. 3.6). Here, a photon is transformed into an electron positron

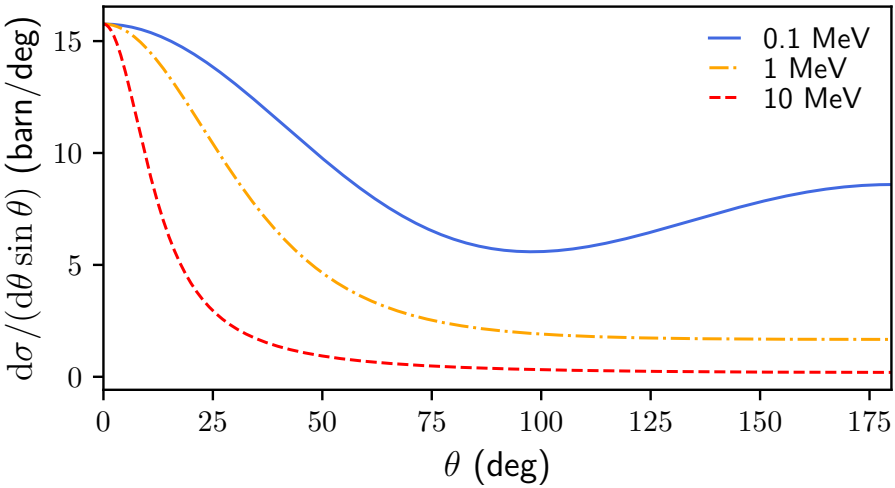

Figure 3.7.: Differential Klein-Nishina cross section $\mathrm{d}\sigma/(\mathrm{d}\theta \sin\theta)$ for various incident γ-ray energies $E_\gamma = 0.1\,\mathrm{MeV}$ (blue), 1 MeV (orange) and 10 MeV (red) in germanium. With increasing γ-ray energy, small scattering angles are more and more favored.

(e^-e^+) pair. Due to momentum conservation, pair production can only occur in the Coulomb field of a nearby atom. The e^-e^+ pair production is only possible if the photon's energy exceeds the rest mass energies of the electron and positron, meaning $E_\gamma \geq 2m_e c^2$ with $m_e c^2 \approx 511\,\mathrm{keV}$. The difference between the incident γ-ray energy and the combined rest mass energies is transferred into kinetic energy of the e^-e^+ pair. In the high energy limit, the cross section of the pair production calculated in Born-approximation is given by

$$\begin{aligned} \mathrm{d}\sigma = 4Z^2 r_e^2 \alpha \frac{\mathrm{d}E_+}{E_\gamma^3} \Bigg[(E_+^2 + E_-^2) \left(\frac{\varphi_1(\xi)}{4} - \frac{1}{3}\ln(Z) - f(Z) \right) \\ + \frac{2}{3} E_+ E_- \left(\frac{\varphi_2(\xi)}{4} - \frac{1}{4}\ln(Z) - f(Z) \right) \Bigg], \end{aligned} \tag{3.6}$$

with the Sommerfeld's constant $\alpha \approx 1/137$, the total energy of the outgoing electron E_- (or positron E_+), two arbitrary screening functions $\varphi_1(\xi)$ and $\varphi_2(\xi)$ and the Coulomb correction $f(Z)$ (see [Leo94] for details). In addition,

$$\xi = \frac{100 m_{e_0} c^2 E_\gamma}{E_+ E_- Z^{1/3}}. \tag{3.7}$$

3.4.2. Mean Free Path

For a given γ-ray energy E_γ, the probability density for a γ ray interacting with matter at the distance d is given by

$$\rho(E_\gamma, d) = \frac{1}{\lambda(E_\gamma)} \exp\left(-\frac{d}{\lambda(E_\gamma)}\right), \tag{3.8}$$

where $\lambda(E_\gamma)$ is the energy-dependent mean free path of the γ ray. It strongly depends on the material the γ rays travel through. It can be directly derived from the material-dependent cross sections $\sigma(E_\gamma)$ (see Sec. 3.4.1) via [Kno00]

$$\lambda(E_\gamma) = \frac{A}{N_A \rho_M \sigma(E_\gamma)}, \tag{3.9}$$

where N_A is Avogadro's constant, ρ_M the mass density and A the mass number of the involved material.

3.4.3. Principle of γ-ray Tracking

The general approach to γ-ray tracking is based on the energy–scattering angle correlation given by Compton scattering (see Eq. (3.2)) and AGATA's high position resolution. Two sets of scattering angles, derived from measured positions as well as deposited energies, are compared via a predefined weighting function. Measurement uncertainties are taken into account during this process.

Given a set of measured interaction points $\vec{r}_{i-1}, \vec{r}_i$ and $\vec{r}_{i+1}$ with respective measured deposited energies $E_{\mathrm{dep},i-1}, E_{\mathrm{dep},i}$ and $E_{\mathrm{dep},i+1}$, two different scattering angles can be calculated. Here, $0 < i < N,\ i \in \mathbb{N}$ with N as the total number of measured interaction points. Using the measured positions, the position based scattering

angle ϑ_i at $\vec{r}_i$ is given by

$$\vartheta_i = \arccos\left(\frac{\langle \vec{r}_i - \vec{r}_{i-1}, \vec{r}_{i+1} - \vec{r}_i \rangle}{||\vec{r}_i - \vec{r}_{i-1}|| \cdot ||\vec{r}_{i+1} - \vec{r}_i||}\right), \tag{3.10}$$

with the scalar product $\langle \vec{a}, \vec{b} \rangle = \sum_j a_j b_j$ and the Euclidean norm $||\vec{a}|| = \sqrt{\sum_j a_j^2}$. Given an incident photon energy E_i after the energy deposition $E_{\mathrm{dep},i-1}$, the Compton-scattering angle θ_i at the deposited energy $E_{\mathrm{dep},i}$ can be calculated using Equation (3.2), yielding

$$\theta_i = \arccos\left(1 - \frac{m_e c^2}{E_i - E_{\mathrm{dep},i}} + \frac{m_e c^2}{E_i}\right). \tag{3.11}$$

To calculate the Compton-scattering angles, it is assumed that the initial photon energy is given by $E_\gamma = \sum_{i=1}^{N} E_{\mathrm{dep},i}$. However, this assumption is not necessarily correct since it is also possible that multiple incident γ rays deposited the measured energy or a higher energetic γ ray was Compton-scattered out of the detector, only partially depositing its energy. To weight the differences in scattering angles θ_i and ϑ_i, a Gaussian distribution

$$\mathcal{G}(\theta_i, \vartheta_i) \propto \exp\left[-\frac{(\theta_i - \vartheta_i)^2}{\sigma^2_{\theta_i,\vartheta_i}}\right], \tag{3.12}$$

can be used. Here, $\sigma_{\theta_i,\vartheta_i} = \sqrt{\Delta\theta_i^2 + \Delta\vartheta_i^2}$ is the Gaussian propagated uncertainty of $\theta_i - \vartheta_i$. The uncertainty $\Delta\theta_i$ is given by

$$\Delta\theta_i = \sqrt{\left(\frac{\partial\theta_i}{\partial E_i}\Delta E_i\right)^2 + \left(\frac{\partial\theta_i}{\partial E_{\mathrm{dep},i}}\Delta E_{\mathrm{dep},i}\right)^2}, \tag{3.13}$$

where

$$\Delta E_i = \sqrt{\sum_{k=1}^{i-1} \Delta E^2_{\mathrm{dep},k}}, \tag{3.14}$$

and

$$\Delta E_{\mathrm{dep},i} = \frac{0.002\, E_{\mathrm{dep},i}}{2.355}, \tag{3.15}$$

corresponding to AGATA's intrinsic energy resolution of 0.2% FWHM [Akk12]. The uncertainty $\Delta\vartheta_i$ can be calculated via

$$\Delta\vartheta_i = \sqrt{\sum_{k=i-1}^{i+1}\sum_{j=1}^{3}\left(\frac{\partial\vartheta_i}{\partial r_{kj}}\Delta r_{kj}\right)^2}, \tag{3.16}$$

with $\Delta r_{kj} = 2.12\,\text{mm}$ (5 mm FWHM) and j as the j-th element of vector $\vec{r}_k$.

For all possible permutations of the N measured interaction points, each potential Compton scattering is validated using the weighting function $\mathcal{G}(\theta_i, \vartheta_i)$ (Eq. (3.12)). In addition, the probability of the last interaction being a photoelectric absorption is included. For a single permutation $\pi(N)$ of all N interaction points, the total probability of the $N-1$ Compton scatterings and the photoabsorption at the last interaction can, e.g., be calculated via

$$P_{\pi(N)} = \left[\prod_{i=1}^{N-1}\mathcal{G}(\theta_i, \vartheta_i)\right] \cdot P_{\text{Photo}}\,. \tag{3.17}$$

The probability $P_{\pi(N)}$ of said permutation is cross-checked against all other possible permutations and subsets including multiple γ rays being the cause for the measured data. The most likely configuration is then accepted as the "true" γ-ray path. How this probability $P_{\pi(N)}$ is constructed strongly depends on the used γ-ray tracking algorithm. Measured interactions can also be rejected, if no permutation yields a physically possible photon path given the assumed incident photon energy, e.g., if the γ ray stemmed from the background radiation emitted from an arbitrary position in the experimental hall.

To reduce the computation time of order $\mathcal{O}(N!)$, clustering algorithms can be used that geometrically form clusters of interaction points. Especially, interaction points that are far away from each other are more likely to stem from different incident γ rays.

3.4.4. Common γ-ray Tracking Algorithms

In general, there exist two major branches of γ-ray tracking algorithms – forward- and backward algorithms.

Forward Methods

The most commonly used approach of γ-ray tracking methods is the forward method. Here, geometrical clusters of interaction points are formed and the tracking is performed in forward direction. This means that the incident γ-ray energy is assumed to be the total sum of deposited energies in the cluster. With this energy, the probability of a γ ray of said energy being emitted from the source position and undergoing all included scattering processes as well as being absorbed at the last interaction is calculated (similar to the explanation in Sec. 3.4.3). The path with the highest probability, often expressed via a figure-of-merit, is chosen to be the "true" path of interaction. If no path is found whose Figure-of-merit lies above a certain pre-set minimum, the cluster size is increased. However, clusters sizes have to be limited since the amount of necessary calculations scales with $N!$, with N as the amount of interactions in the cluster, since all possible permutations of the interaction points have to be calculated. This, however, limits the achievable performance – at least for experiments where a high photon multiplicity is expected.

The two major tracking algorithms of the forward-type are MGT [Baz04, KL19] and OFT [Lop04, KL19]. Both algorithms are used in this work.

MGT: The Mars Gamma-ray Tracking MGT was developed by D. Bazzacco *et al.* [Baz04, Lie01]. After a geometrical clustering is performed based on a preset opening angle in which all interaction points considered to be part of a single γ ray lie, the measured energies E_{dep} are compared to the deposited energies calculated via the Compton-scattering formula (see Eq. (3.2)). The likelihood of the measured interaction points stemming from a single γ ray is evaluated via a χ^2 test, comparing all interaction points in the sequence via

$$\chi^2 \propto \sum_{n=1}^{N-1} W_n \left(\frac{E_{\mathrm{dep},n} - E_{\mathrm{pos},n}}{E_\gamma} \right)_n^2 , \tag{3.18}$$

with the weighting factors W_n including photo-absorption, Compton scattering, pair-production and travel-path probabilities of the potential γ-ray, measured deposited energy at the n-th interaction point $E_{\mathrm{dep},n}$ and the deposited energy $E_{\mathrm{pos},n}$ via Compton scattering derived from the geometrical scattering angle ϑ_n at the n-th interaction point (see Eq. (3.10)). A potential γ ray is accepted, if its χ^2 lies below a predefined threshold χ^2_{Max}.

OFT: The Orsay Forward Tracking OFT [Lop04] is based on the principle of MGT. However, the clustering algorithm is much more sophisticated than in MGT. Instead of a predefined opening acceptance angle, the clustering is performed using the measured amount of interaction points n_{int}. The maximum angular separation, describing the largest angle in which interaction points potentially corresponding to a single γ ray may lie, is defined as

$$\alpha_{\max} = \arccos\left(1 - \frac{2}{[(n_{\mathrm{int}}+2)/3]^{0.9}}\right). \tag{3.19}$$

Hence, given the spherical coordinate angles for two interactions points θ_i, φ_i and θ_j, φ_j, two interaction points are considered to be in the same cluster, if

$$\left|\arccos\left(\sin\theta_j \sin\theta_i \cos(\varphi_j - \varphi_i) + \cos\theta_i \cos\theta_j\right)\right| \leq \alpha_k\,, \tag{3.20}$$

holds. All interaction points that lie in cones with $\alpha_k < \alpha_{\max}$ are assigned to the same cluster. The angle α_k is increased iteratively until $\alpha_{\max}$ is reached. Similar to MGT, the physical likelihood of all those interaction points stemming from a single γ ray is evaluated via a figure-of-merit

$$F_{\mathrm{tot}} = \left[\prod_{n=1}^{N-1} P_n \cdot \exp\left(\frac{-a(E_{\mathrm{dep},n} - E_{\mathrm{pos},n})^2}{\sigma_c^2}\right)\right]^{1/(2N-1)}, \tag{3.21}$$

with the uncertainty in energies caused by energy and position resolution of AGATA (see also Sec. 3.4.3) and the probabilities P_i for Compton scattering or photo-absorption as well as traveling a certain distance in germanium. The values $E_{\mathrm{dep},n}$ and $E_{\mathrm{pos},n}$ are the same as in MGT. The permutation that maximizes F_{tot} is taken as the most likely configuration. If all values of F_{tot} lie below a preset threshold, the cluster is rejected. The three essential parameters of OFT are *sigma_theta*, *minprobsing* and *minprobtrack*. Here, *sigma_theta* parameterizes the position uncertainty assumed by OFT in centimeters. A *sigma_theta* of 0.8, e.g., means that the uncertainty (see also Δr_{kj} in Eq. (3.16)) is 0.8 cm. In addition, *minprogsing* is the minimum figure-of-merit for single interactions for which a single interaction is accepted as stemming from one γ ray. If the figure-of-merit is below said value, the single interaction point cluster is rejected. Similarly, *minprobtrack* is the minimum for the figure-of-merit (see Eq. (3.21)) for clusters containing more than one interaction point.

Backward Methods

In contrast to the forward approach, “Back tracking” methods search for energy deposition in the range of 100-250 keV [MC99, MC02, MC03]. In this energy region, photoelectric absorption is the most likely scenario of the interaction of γ rays with the HPGe detectors (see Fig. 3.6). Starting from these interaction points, the most likely path of the photon is reconstructed backwards via the measured energies at their respective interaction points and the geometrical scattering angles (similar to Sec. 3.4.3). However, this method does not perform as well as forward methods since the possibility of a high-energetic γ ray in the range of a few MeV being directly photo-absorbed is neglected completely [Lop04].

Hence, in general, forward methods are utilized in experiments with AGATA. A novel approach based on a probabilistic modeling of the γ-ray paths using Bayesian inference [SS06], firstly developed in [Nap16], is presented in Appendix A.

4. *Coulex-multipolarimetry* – First Benchmark Tests

A first example of possible applications for γ-ray tracking techniques are emission position reconstruction procedures, a method commonly used by so-called Compton cameras [Ste17, Ald17]. An experiment where such capabilities are demanded of AGATA was the ^{85}Br $\pi p_{3/2} \rightarrow \pi p_{1/2}$ spin-flip experiment performed during the PreSPEC campaign at GSI in 2014. It was planned as a first benchmark test of the novel *Coulex-multipolarimetry* method [Sta15b], determining $E2/M1$ multipole mixing ratios via measurement of beam-energy dependent γ-ray yields.

In the following, the physical motivation behind said experiment as well as the experimental setup, used data analysis methods and results are presented and discussed in regards to standard γ-spectroscopic analysis tools and γ-ray tracking and derived approaches. The data analysis has been performed with the `elder-pt` framework developed by M. Reese (see [Ree18, Ree] for details).

The work presented in this Chapter is based on [Nap20b].

4.1. Motivation

Single particle states are one of the major keys to access information about the underlying structure of a nucleus. However, the unambiguous identification of such states is crucial to yield reliable predictions about nuclear structure. Fortunately, single-particle excitations in even-odd nuclei can be identified via the so-called spin-flip transition. Such a transition corresponds to a transition of a single nucleon in a nucleus from a $j_> = l + 1/2$ to a $j_< = l - 1/2$ state. These types of transitions exhibit one of the largest known $M1$-transition strengths in the range of $\sim 1\,\mu_N^2$ [Sta15a, Sta15b].

In the vicinity of the doubly magic nucleus ^{78}Ni, situated far from the valley of

stability, the evolution of single-particle excitation energies in odd Ni isotopes has been subject to numerous experimental and theoretical studies. Here, changes in relative positioning of the $\pi p_{1/2}, \pi p_{3/2}, \pi f_{5/2}$ and $\pi f_{7/2}$ shells potentially caused by the tensor-force [Ots05, Ots10] as a function of the filling of the $\nu g_{9/2}$ shell have been observed [Fra98, Fra01, Fla09]. In a similar manner, the evolution of single-particle energies in the $N = 50$ isotonic chain of ^{78}Ni has also been subject to experimental studies. The first nucleus that has been analyzed in this region in regards to single-particle energies was ^{87}Rb [Sta13]. Its $1/2^-_1 \rightarrow 3/2^-_{\text{g.s.}}$ transition has been identified as the main fragment of a single-particle $\pi p_{3/2} \rightarrow \pi p_{1/2}$ transition via measurement of the corresponding $M1$-transition strength of $0.64^{+8}_{-5}\,\mu^2_N$.

In the next even-odd nucleus towards ^{78}Ni [Tan19], the neutron-rich ^{85}Br, the $1/2^-_1$ state with an energy of 1191 keV has been suggested to be the most likely candidate for a single-particle excitation. To measure the $M1$-transition strength of the $1/2^-_1 \rightarrow 3/2^-_{\text{g.s.}}$ transition, a novel experimental technique, the *Coulex-multipolarimetry* was developed by C. Stahl *et al.* [Sta15b]. Its working principle is based on the fact that excitation cross-sections of $M1$ to $E2$ scale with the velocity v of the used beam with $(v/c)^2$ [AW79]. Hence, $M1$ transitions are not suppressed at large beam velocities $v \approx c$. Due to this relation, the $E2/M1$ multipole mixing ratio δ can be obtained via γ-ray yield measurements with two different beam energies.

As a first benchmark test of this novel method, experiment S426 of the PreSPEC campaign at GSI has been performed in March 2014. The experimental setup consisted of the FRagment Separator (FRS) [Gei92], the Lund-York-Cologne CAlorimeter (LYCCA) [Gol13], AGATA and the High Energy deteCTOR (HECTOR) [Maj94].

In the following, this first benchmark test of the *Coulex-multipolarimetry*, is presented. The principle of *Coulex-multipolarimetry* as well as the experimental setup are described. Theoretical relative yields of target-to-beam like excitations are shown. In addition, all used particle-like conditions are emphasized. Afterwards, the measured results are given and discussed. The possible impact of γ-ray tracking and derived data analysis techniques are also shown.

4.2. *Coulex-multipolarimetry*

The method of *Coulex-multipolarimetry* is based on the fact that $M1$-excitation cross sections are generally not strongly influenced by the beam velocity whereas $E2$ excitations are. In general, the ratio of $M1/E2$ cross sections scale with β^2. Hence, the multipole mixing ratio for $E2/M1$ [Suh07]

$$\delta = \frac{\sqrt{3}}{10}\frac{E_0}{\hbar c}\frac{\langle J_f||\mathscr{M}(E2)||J_i\rangle}{\langle J_f||\mathscr{M}(M1)||J_i\rangle}, \tag{4.1}$$

with the reduced electromagnetic transition matrix elements $\langle J_f||\mathscr{M}(M1)||J_i\rangle$ (see Secs. 2.1 and 2.2) for $M1$ and $E2$ transitions can be accessed via measurement of γ-ray yields

$$y = \rho_t \frac{N_A}{A_t}\int_{x_1}^{x_2} \mathrm{d}x\, \sigma(E_{\mathrm{kin}}(x)) \tag{4.2}$$

for two different beam energies E_{kin}. Here, ρ_t is the mass density of the target material, N_A is the Avogadro constant, A_t the mass number of the target nuclei and $\sigma(E_{\mathrm{kin}}(x))$ the excitation cross sections as a function of the beam energy. Since the energy loss of the beam in matter can be modeled approximately [TB08, Wei10], an experimental setup with a single beam energy and two consecutive targets can be used. After the first target, the kinetic energy of the beam has dropped significantly which results in different yields y from the second target (see Fig. 4.1). The ratio of those yields then can be used to gain access to δ (see Fig. 4.2) under the condition that $\delta \in [0.01, 0.1]$ for ^{85}Br as the nucleus of interest since for smaller or larger values of δ, there is no sensitivity on the γ-ray yield ratio anymore (see Fig. 4.2). For more details on *Coulex-multipolarimetry*, see [Sta15b].

4.3. Setup

The used setup of the experiment performed at GSI is depicted in Figure 4.3. The primary ^{86}Kr beam that was extracted from the heavy-ion synchrotron SIS 18 impinged on a thick ^{9}Be fragmentation target. The produced fragments were then separated by mass and charge number by the FRS, resulting in an almost

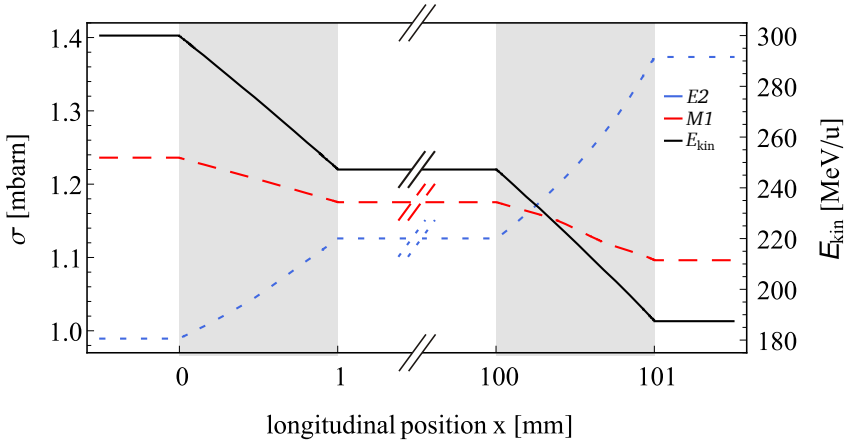

Figure 4.1.: Beam-energy E_{kin} (black) of ^{85}Br nuclei due to energy loss in two consecutive gold targets with 1 mm thickness. The cross sections for $E2$ (blue) and $M1$ (red) transitions of the ^{85}Br beam nuclei due to the varying beam energy develop differently. The cross sections were calculated via DWEIKO with $B(M1) = 1\,\mu_N^2$ and $B(E2) = 1$ W.u. Reprinted from [Sta15b], Copyright (2015), with permission from Elsevier, and slightly modified.

pure ^{85}Br beam with $E_{\text{kin}} = 300$ MeV/u at the entrance point of the experimental hall with an average rate of $4.9 \times 10^4\,\text{s}^{-1}$. Due to the large achieved purity of the secondary beam, particle tracking detectors of the FRS were switched off, yielding a smaller dead-time of the complete system. Time-of-flight detectors and scintillators of the FRS were still operating. After extraction, the beam impinged on the consecutively aligned ^{197}Au targets with respective thicknesses of 2 g/cm^2 and 1 g/cm^2. After the first target, the beam is approximately left with a kinetic energy of 242 MeV/u and with 210 MeV/u after the second target (calculated via LISE++[1] [TB08]). Emitted γ rays were detected by AGATA which consisted of 21 detectors during the experiment. Particle identification of the outgoing beam was performed via LYCCA.

[1] *He*-parameterization [Hub90] for energy-loss calculations was used

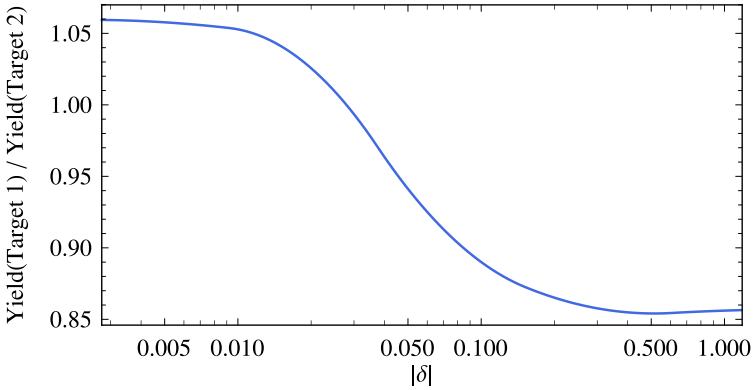

Figure 4.2.: Relation between measurable target yield ratios and $E2/M1$ multipole mixing ratio $|\delta|$ for ^{85}Br. Only for values of $\delta \in [0.01, 0.1]$, target yields can be used to obtain information about δ. Reprinted from [Sta15b], Copyright (2015), with permission from Elsevier, and slightly modified.

4.3.1. LYCCA

The Lund-York-Cologne CAlorimeter LYCCA plays an essential role for the benchmark test experiment since a lot of undesired background can be reduced via its usage. In total, LYCCA consists of five different modules [Gol13].

- Three Time-of-flight detectors situated in front of the reaction chamber (called ToFStart for now), at target position (called ToFTarget) and at the beam-dump position (called ToFStop).
- A double sided silicon-strip detector (DSSSD) at target position (called TargetDSSSD).
- The LYCCA $\Delta E - E_{\text{kin}}$ wall which is used as a beam-dump.

A detailed description of all modules can be found in [Gol13]. All LYCCA detectors are depicted in Figure 4.4. In the setup of the experiment, only the ToFStop detector, the TargetDSSSD as well as the $\Delta E - E_{\text{kin}}$ wall were used.

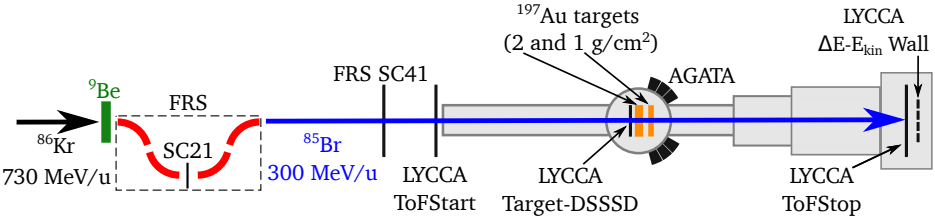

Figure 4.3.: Schematic drawing of the experimental setup. The incident ^{86}Kr beam is shown in black, the ^{9}Be fragmentation target in green, and the secondary ^{85}Br beam in blue. The FRS scintillator SC21 inside the FRS and the SC41 scintillator directly in front of the experimental hall as well as all LYCCA components present in the experiments are depicted. The target chamber with the two gold targets (in orange) as well as AGATA is shown. For simplicity, the FRS is only schematically shown with its dipole magnets in red (for details on the FRS, see [Gei92]). The picture was adapted from [Ree18] and modified. Drawing is not to scale.

ToFStop

The ToFStop detector (as well as ToFStart) consists of two independent plastic scintillators in a circular shape. Their diameter is 270 mm and their thickness 1 mm. The light yield from a particle interaction with the scintillator is read out by 32 photomultiplier tubes (PMTs). Since the light signal, emerging from the point of impingement of the beam with the scintillators, travels with a constant velocity $v < c_0$ (due to the refraction index of the scintillator), the respective measured times $t_i = d_i/v$ of all 32 PMTs can be used to geometrically pinpoint the position of impingement via the measured travel distances d_i of each PMT (see [Ree13, Ree18] for details).

$\Delta E - E_{\mathrm{kin}}$ Wall

The $\Delta E - E_{\mathrm{kin}}$ wall is built out of various modules consisting of a DSSSD for energy loss measurements and nine CsI(Tl) scintillators for total kinetic energy measurement of the beam. The CsI(Tl) scintillators are square-shaped with a front face

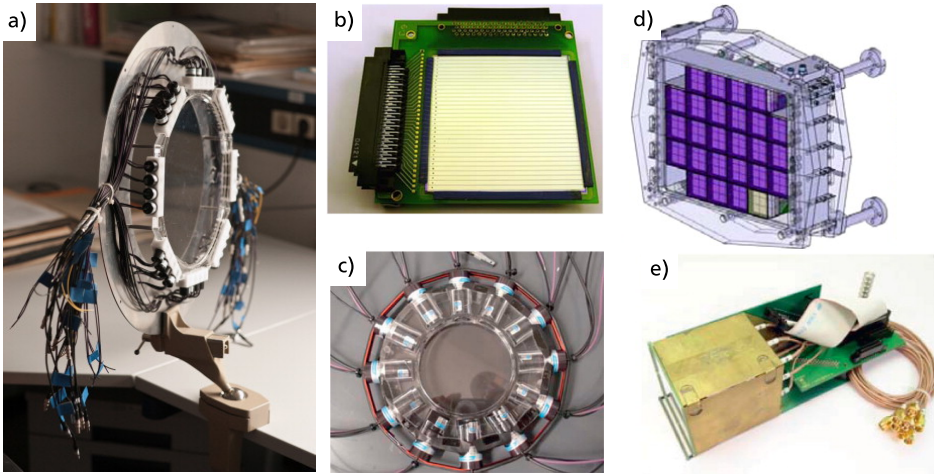

Figure 4.4.: Pictures of all LYCCA detectors used in the PreSPEC campaign. ToFStart and ToFStop (a), TargetDSSSD (b), ToFTarget (c, removed for S426), schematics of the $\Delta E - E_{\mathrm{kin}}$ wall (d) and picture of said wall (e). Pictures (b-e) reprinted from [Gol13], Copyright (2013), and (a) reprinted from [Hoi11], Copyright (2011) with permission from Elsevier, slightly modified in and adapted from [Ree18].

area of $19.4 \times 19.4\,\mathrm{mm}^2$ and two possible thicknesses of 10 mm or 33 mm – depending on the used beam-energy. The DSSSD detectors, wall DSSSDs as well as TargetDSSSD, are also square-shaped with front face areas of $58.5 \times 58.5\,\mathrm{mm}^2$. They are divided into 32 strips on the respective p- and n-sides. The strip-orientations of the p- and n-side are perpendicular to each other. The $\Delta E - E_{\mathrm{kin}}$ wall is generally used for particle identification of the beam particles behind the reaction chamber. The energy-loss in the DSSSD for a certain type of beam nucleus ${}^{A}_{Z}\mathrm{X}$ with mass number A and charge number Z is proportional to [Ree18]

$$\Delta E \propto \chi \frac{Z^2}{\beta^{\kappa}}, \tag{4.3}$$

with empirical constants χ and κ that can be determined from energy-loss calculations of charged particles in matter, e.g, via the program `ATIMA` [Wei10, LS96].

In addition to the energy loss in the DSSSD, the total remaining kinetic energy of the beam after passing through the DSSSD is measured via the large CsI(Tl) blocks. Since

$$E_{\text{kin}} = mc^2(\gamma - 1) = Au\,c^2\left(\frac{1}{\sqrt{1-\beta^2}} - 1\right), \tag{4.4}$$

with the atomic mass unit u, the energy loss and the kinetic energy are linked via a power law in β for the same nucleus ${}^{A}_{Z}\text{X}$, measurement of ΔE and E_{kin} can be used for beam particle identification. A detailed description of all detector systems can be found in [Gol13] and [Ree18].

For the benchmark test of *Coulex-multipolarimetry*, a total amount of 73 hours of beam time were scheduled. In the following, calibrations, performed data analysis methods such as expected yields and particle conditions are presented.

4.3.2. Calibrations

LYCCA

For the calibration of LYCCA, many automatized procedures developed by M. Reese (see [Ree18]) can be used. All DSSSD detectors are automatically calibrated by the analysis code, gain matching p- and n-side signals via a probabilistic approach (see [Ree18]). Hence, the resulting ΔE spectra were only gain matched to be aligned at a $\Delta E = 305\,\text{MeV}$, as calculated via `LISE++` (see Fig. 4.5 (left)). Similarly, all CsI(Tl) detectors were gain matched to align at 17.5 GeV (see Fig. 4.5 (right)). The position of ion impingement of the ToFStop detector was calibrated via a novel method described in [Ree13]. Here, the variance of the time measurements of all PMTs t_i is

$$\text{Var}_{x,y}(\{t_i\}) = \left\langle t_i^2 \right\rangle - \left\langle t_i \right\rangle^2, \tag{4.5}$$

which directly depends on the position of impingement. An iterative process is used to find the respective position of impingement $x_{\text{true}} = (x, y)^\intercal$ via assuming a start value of impingement (x_0, y_0) and iterating until a minimum for $\text{Var}_{x,y}(\{t_i\})$ is found. For details see [Ree13, Ree18]. A comparison of the achieved positions to the ones obtained from the DSSSD of the $\Delta E - E_{\text{kin}}$-wall modules is shown exemplarily for the x-coordinate of both detectors in Figure 4.6.

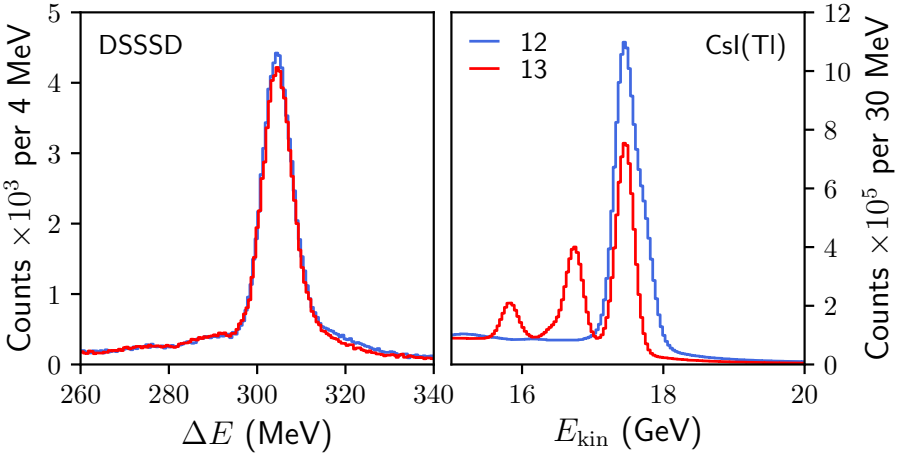

Figure 4.5.: Calibration of the DSSSD and CsI(Tl) detectors exemplarily shown for two $\Delta E - E_{\mathrm{kin}}$ modules (module number 12 in blue and 13 in red).

AGATA

The energy calibration of all $21 \times 36 = 756$ crystal segments and their respective 42 core signals has been performed via ^{60}Co and ^{152}Eu measurements. The resulting spectra for all segments are shown in Figure 4.7. The segments were multiplied by their respective core id for better visibility. To account for any potential neutron-damage that might alter the measured energies [Bru13], the segment energies have been scaled to their respective measured core energy via

$$E'_{\mathrm{seg},i} = E_{\mathrm{seg},i} \frac{E_{\mathrm{dep,core}}}{\sum_j E_{\mathrm{seg},j}}, \tag{4.6}$$

where $E_{\mathrm{seg},i}$ is the measured segment energy, $E_{\mathrm{dep,core}}$ the total measured energy of the respective core and $E'_{\mathrm{seg},i}$ the energy after the correction. This approach is sufficient since the movement of electrons is not as severely influenced by neutron damage of the detector as electron-holes. Since the amount of hit segments per event is relatively low (see Fig. 4.7), this approach is suited to correct for neutron

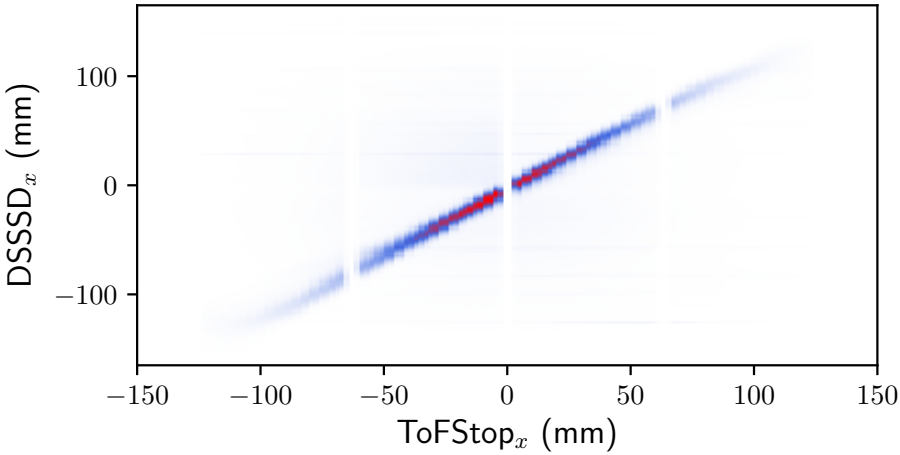

Figure 4.6.: Comparison between x-values of ToFStop and the DSSSD of the $\Delta E-E_{\text{kin}}$ wall. Events from the same ^{85}Br nucleus lie on a diagonal line.

damage. For high event rates, potential pile-up in the measured core energies might yield an incorrect measured deposited energy in the core. This would lead to a falsely assigned segment energy. Different measures have to be taken in this scenario [Bru13].

4.4. Data Analysis

4.4.1. Expected Relative Yields

As mentioned in Section 4.2, the relation between target- and beam-excitation cross sections are the main focus behind *Coulex-multipolarimetry*. However, since the incident beam energy is quite high, the absolute cross sections for the respective excitations coupled to the target-position-dependent efficiencies of AGATA need to be taken into account. To calculate beam-energy dependent cross-sections, the program `DWEIKO` (see Sec. 2.1.2) has been used. For simplicity, the only two transitions analyzed via `DWEIKO` are the $7/2_1^+ \rightarrow 3/2_{\text{g.s.}}^+$ transition in gold with

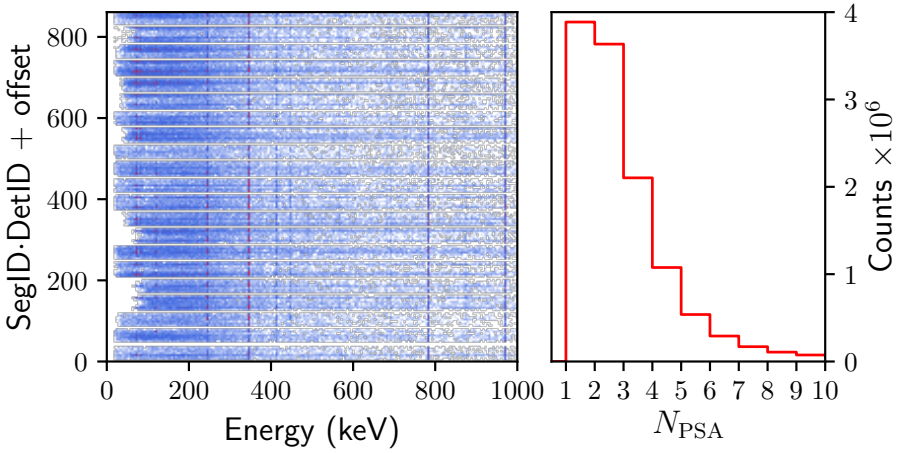

Figure 4.7.: *Left*: ^{152}Eu spectrum of energy-calibrated and aligned segment energies of all 21 used AGATA detectors. The segments were multiplied by their detector id. For better visibility, the different detector id multiplied by segment id were offset slightly between the different detectors. *Right*: Event multiplicity of PSA events independent of core id.

$E_{\gamma,\mathrm{Au}} = 547.5\,\mathrm{keV}$ with a transition strength $B(E2,\downarrow) = 33.3\,\mathrm{W.u.}$ [Stu88] and the potential spin-flip transition $1/2^-_1 \rightarrow 3/2^-_{\mathrm{g.s.}}$ in ^{85}Br with $E_{\gamma,\mathrm{Br}} = 1191\,\mathrm{keV}$ [HT75]. For the potential spin-flip transition, an assumed $M1$-transition strength corresponding to a proton transitioning from a $j = 1/2$ to a $j = 3/2$ state (with $l = 1$), given by [Sta15a]

$$\begin{aligned} B(M1; 1/2 \rightarrow 3/2) &= \frac{1}{2} \left| \langle 3/2 || \mathscr{M}(M1) || 1/2 \rangle \right|^2 \\ &= \frac{1}{2\pi} \left(g_l^\pi - g_s^\pi \right)^2 \mu_N^2 \\ &= 3.34\, \mu_N^2 , \end{aligned} \tag{4.7}$$

Table 4.1.: Excitation cross sections σ_i (calculated via DWEIKO) for gold target and bromine beam excitations and their ratio $\eta^\star$, relative photo-absorption efficiencies ϵ_{rel} and resulting efficiency weighted ratios η under the made assumptions on $B(M1)$ and $B(E2)$ values in ^{85}Br (see text) for two different beam energies E_{kin} at the respective targets.

E_{kin} (MeV/u)	β	σ_{Au} (mb)	σ_{Br} (mb)	$\eta^\star$	ϵ_{rel}	η
300	0.65	63.4	4.72	13.4	0.98	13.2
242	0.61	73.0	4.64	15.7	1.23	19.4

is used. Here, $g_l^\pi = 1$ is the orbital g-factor of a proton and $g_s^\pi = 5.59$ its unquenched spin g-factor [Suh07]. In addition, a small $E2$ contribution of $B(E2) = 1\,\text{W.u.}$ is added, resulting in a $\delta = 0.026$ and an approximate mean lifetime of 10 fs (see Sec. 2.2). With these assumptions, the fraction of target- to beam-like cross sections as a function of the beam energy reads

$$\eta^\star := \frac{\sigma_{\text{Au}}(E_{\text{kin}})}{\sigma_{\text{Br}}(E_{\text{kin}})}. \tag{4.8}$$

Table 4.1 depicts the calculated cross sections as well as their ratios for the beam energy before and after the first gold target with $2\,\text{g/cm}^2$. The DWEIKO input files can be found in Appendix B. To include the geometry-dependent influence of AGATA's efficiency, an efficiency-weighted ratio of target- to beam-like excitations can be defined as

$$\eta_i = \eta_i^\star \cdot \epsilon_{\text{rel},i} = \eta_i^\star \cdot \frac{\epsilon_{\gamma,i}(E_{\gamma,\text{Au}})}{\overline{\epsilon_{\gamma,i}}(E_{\gamma,\text{Br}})}, \tag{4.9}$$

with the photo-absorption efficiency of incident ^{197}Au γ rays emitted from the i-th target

$$\epsilon_{\gamma,i}(E_{\gamma,\text{Au}}) = \frac{N_{\text{abs,Au},i}}{N_{\text{tot}}}, \tag{4.10}$$

with $N_{\text{abs,Au},i}$ as the amount of fully-absorbed ^{197}Au γ rays emitted from target position i, N_{tot} as the total amount of emitted γ rays. No significant Doppler-

broadening of ^{197}Au γ rays is assumed. The integrated efficiency for γ rays emitted by the ^{85}Br beam nuclei with energy $E_{\gamma,\mathrm{Br}}$ at target i is given by

$$\overline{\epsilon_{\gamma,i}}(E_{\gamma,\mathrm{Br}}) = \int_{-1}^{1} \mathrm{d}\cos\Theta \, \frac{N(E'_{\gamma,\mathrm{Br}} \,|\, \mathrm{abs.}, i)}{N_{\mathrm{tot}}}, \tag{4.11}$$

with $N(E'_{\gamma,\mathrm{Br}} \,|\, \mathrm{abs.}, i)$ as the amount of photo-absorbed, Doppler-shifted ^{85}Br γ rays emitted from target position i, Θ as the emission angle of the γ ray in the center-of-mass frame of the beam and the Doppler-shifted energy $E'_{\gamma,\mathrm{Br}} = E'_{\gamma,\mathrm{Br}}(\cos\Theta, \beta)$ (see Eq. (2.41)). To estimate the amount of absorbed γ rays (target- or beam-like), a *Geant4* simulation [Ago03, All06, All16] using the AGATA simulation code [Far10] has been used. Although this might introduce some discrepancies to measured efficiencies, simulated γ rays suffice for this estimate since only ratios $\epsilon_{\mathrm{rel},i}$ between efficiencies are of interest. In addition, the better grasp on the position of emission of the γ rays allows for a cleaner target-specific estimate as well as the exact impact of the Lorentz-boosted emission direction of the bromine γ rays can be included. In total, the efficiency-weighted ratios between gold and bromine excitations are $\eta_1 = 13.2$ and $\eta_2 = 19.4$ (see also Table 4.1).

4.4.2. Particle Conditions

An excessive amount of background radiation is present caused by atomic background from the beam's interaction with various particle detectors and targets as well as particles, e.g., neutrons, emitted by the FRS that interact with AGATA, yielding large amounts of measurable Ge(n, n′γ) and Al(n, n′γ) reactions, where the latter are caused by neutron reactions with the detector capsules made of aluminium. To significantly reduce the background radiation and therefore enhancing the selectivity of the *Coulex-multipolarimetry*, conditions on LYCCA's particle detectors can be utilized.

The first used condition is the outgoing particle identification of the beam via LYCCA's $\Delta E - E_{\mathrm{kin}}$ wall modules. As mentioned in Section 4.3.1, the energy loss ΔE in the DSSSD can be correlated with the total remaining kinetic energy of the beam E_{kin} measured by the CsI(Tl) crystals. The comparison between those energies is shown in Figure 4.8. The peak in Figure 4.8 at $\Delta E = 305\,\mathrm{MeV}$ and $E_{\mathrm{kin}} = 17.5\,\mathrm{GeV}$ shows that most of the incident particles are in fact ^{85}Br nuclei. At $15\,\mathrm{GeV} < E_{\mathrm{kin}} < 17.5\,\mathrm{GeV}$ with constant $\Delta E = 305\,\mathrm{MeV}$, additional peaks arise.

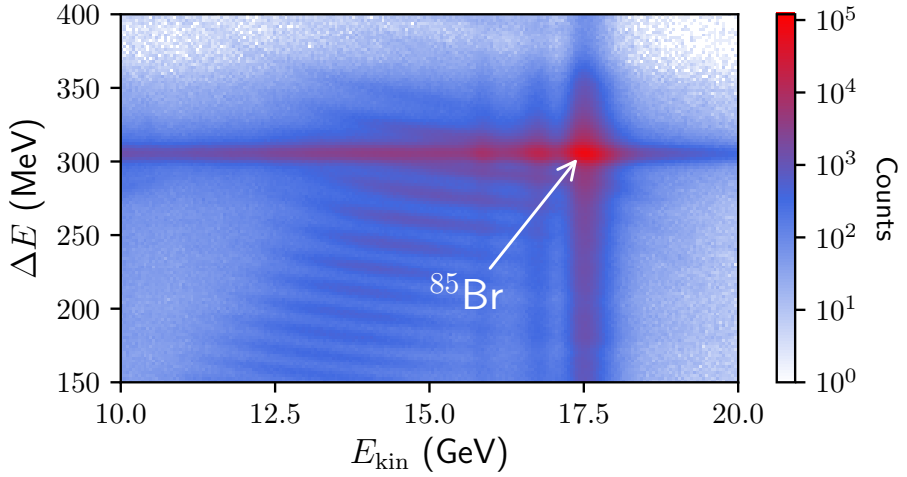

Figure 4.8.: Total remaining kinetic energy E_{kin} in the CsI(Tl) scintillators vs. energy loss ΔE in the DSSSD of LYCCA's $\Delta E - E_{\mathrm{kin}}$ wall modules. The peak at $E_{\mathrm{kin}} = 17.5\,\mathrm{GeV}$ and $\Delta E = 305\,\mathrm{MeV}$ corresponds to ^{85}Br nuclei. Diagonal lines correspond to different types of nuclei. Picture adapted from [Nap20b].

These are probably also caused by ^{85}Br nuclei, but were most likely assigned to wrong values of E_{kin} due to instabilities in the used electronics. This limits the particle identification directly to the region around $\Delta E = (305 \pm 14)\,\mathrm{MeV}$ and $E_{\mathrm{kin}} = (17.5 \pm 0.4)\,\mathrm{GeV}$.

Random events from the background or other coincident particles (possibly ^{85}Br or a different type of nucleus) might spoil the energy measurement used to identify the beam nuclei. To ensure a correct correlation between DSSSD and CsI(Tl), the x and y positions on the DSSSD and the CsI(Tl) crystals are cross-checked with the respective positions on the time-of-flight detector ToFStop directly situated in front of the $\Delta E - E_{\mathrm{kin}}$ wall modules (see Sec. 4.3.1). If a single ^{85}Br nucleus impinges on the ToFStop perpendicular to its plane (which can be assumed to be the case), it should hit the DSSSD and the CsI(Tl) on the same x and y position.

Thus, correlating the x (or y) positions of the ToFStop and the DSSSD should yield a diagonal line. The relation between the ToFStop's and DSSSD's x coordinate is shown in Figure 4.6.

The time information between particles and γ rays can be obtained via the global trigger and synchronization system (GTS) timestamp that links the AGATA data acquisition (NARVAL) [Akk12] with the Multi Branch System (MBS) of GSI [EK99, Ess96]. Reliable time differences can be extracted from the FRS's scintillator SC21 (see Fig. 4.3) time as well as AGATA's γ time obtained from the pulse shapes of each contributing crystal. The particle-γ time difference can be expressed via

$$\begin{aligned} \Delta T = T_{\mathrm{GTS(AGATA)}} - T_{\mathrm{GTS(MBS)}} \\ + \Delta t_{\mathrm{GTS(AGATA)},\gamma} - \Delta t_{\mathrm{GTS(MBS)},p}\,, \end{aligned} \tag{4.12}$$

where $T_{\mathrm{GTS(AGATA)}}$ and $T_{\mathrm{GTS(MBS)}}$ are the GTS timestamps of AGATA and the MBS. In addition, $\Delta t_{\mathrm{GTS(AGATA)},\gamma}$ is the time difference between $T_{\mathrm{GTS(AGATA)}}$ and the measured time of the incident γ extracted from AGATA's pulse shapes, $\Delta t_{\mathrm{GTS(MBS)},p}$ is the time difference between $T_{\mathrm{GTS(MBS)}}$ and the particle time measured by the FRS scintillator SC21 (see Fig. 4.3). The resulting time difference spectrum is shown in Figure 4.9.

4.5. Results

All γ-ray energies measured via AGATA's cores (details see Sec. 3.2.1) are depicted in Figure 4.10 with and without any particle-like conditions (see Sec. 4.4.2). In addition, the Doppler-corrected γ-ray spectra for the gated spectrum are shown in Figure 4.11. The interaction point with the largest deposited energy is chosen as the first interaction point of the respective incident γ rays. This assumption is used to compute the angle of emission between the emitted γ ray and the beam direction. The beam velocities after the respective targets T_1 and T_2 are $\beta_1 \approx 0.61$ and $\beta_2 \approx 0.58$ which are approximately known from `LISE++` calculations. As shown in Figure 4.12, the CoulEx of the $7/2^+_1 \rightarrow 3/2^+_{\mathrm{g.s.}}$ transition of ^{197}Au at 547.5 keV is present, consisting of $A_{\mathrm{Au}} = 2110(370)$ counts. Applying the ratios $\eta_1 = 13.2$ and $\eta_2 = 19.4$ from cross section and efficiency estimates (see Sec. 4.4.1), a total of 160 counts for T_1 and 110 counts for T_2 in the Doppler-corrected spectra for the $1/2^-_1 \rightarrow 3/2^-_{\mathrm{g.s.}}$ transition of ^{85}Br are expected. Compared to the present

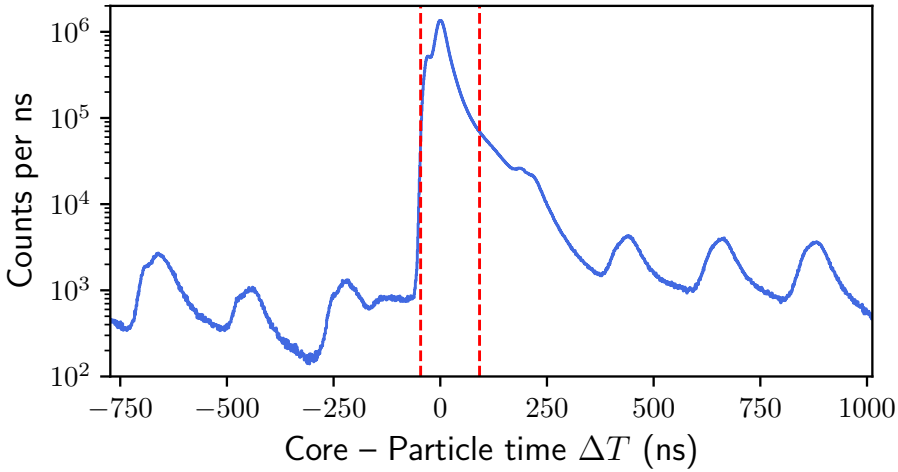

Figure 4.9.: Time difference ΔT between the particle time from FRS and AGATA's time extracted via PSA in nanoseconds. All 21 AGATA crystal - FRS time differences have been offset to align at 0 ns. Beam spills every 220 ns are the cause for the periodic structure. The gates on ΔT, shown in red, are used to select the prompt peak. Roughly 90 % of all events are contained in this region. Picture adapted from [Nap20b].

background in the Doppler-corrected spectra, this amount of anticipated events is negligibly small. Although no transition of ^{85}Br has been observed, a detection limit (see Fig. 4.12) for such transitions can be performed.

4.6. Discussion

The detection limit for the potential $\pi p_{3/2} \rightarrow \pi p_{1/2}$ spin-flip transition of ^{85}Br can be obtained via an estimate on the statistical background fluctuation around the peak-of-interest area at 1191 keV. To estimate the background, a second order

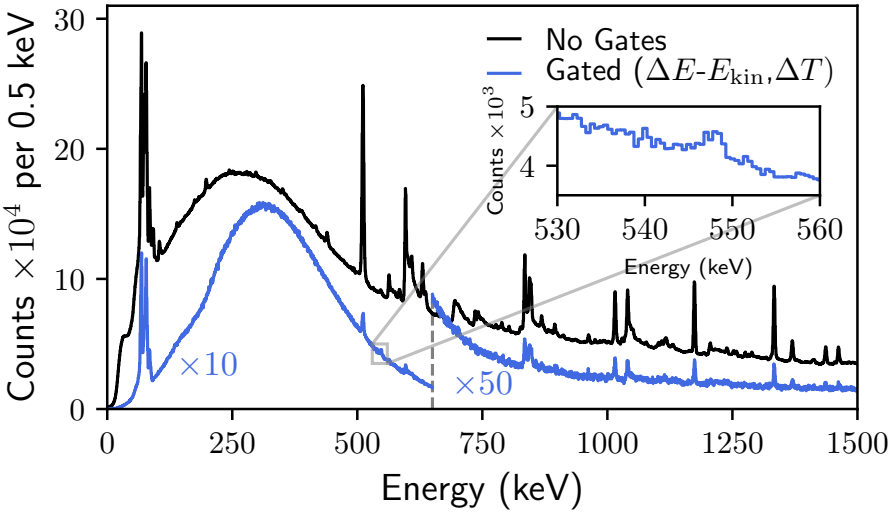

Figure 4.10.: Core energies measured by AGATA in ∼73 h of beam time without any conditions on any ancillary detectors in black and with ^{85}Br particle identification condition on LYCCA and time condition on prompt beam in blue (see Sec. 4.4.2). For better visibility, the gated spectrum was upscaled by a factor of ten for energies up to 650 keV and by a factor of 50 for larger energies. Picture adapted from [Nap20b].

polynomial

$$p(E, a_0, a_1, a_2) = \sum_{i=0}^{2} a_i E^i \,, \tag{4.13}$$

with the three parameters a_0, a_1 and a_2 and the deposited energy E is applied. A non-linear regression around the expected peak-of-interest area in the Doppler-corrected spectra is performed. The area, or amount of counts, around the peak-

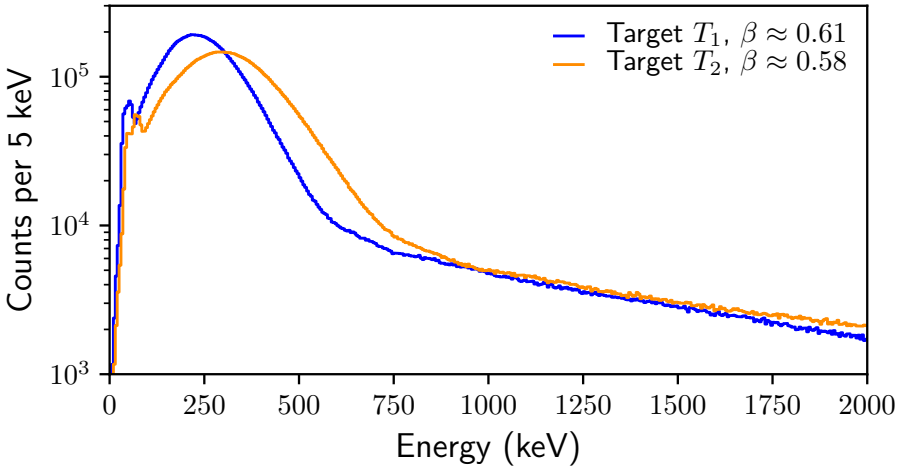

Figure 4.11.: Doppler-corrected particle gated (see Sec. 4.4.2) γ-ray energy spectra for target 1 (blue) and target 2 (orange) with respective velocities β. No beam excitation of ^{85}Br at 1191 keV is present. Picture adapted from [Nap20b].

of-interest can be calculated via

$$A_B = \int_{E_{\gamma,\mathrm{Br}}-\sigma_E}^{E_{\gamma,\mathrm{Br}}+\sigma_E} \mathrm{d}E\, p(E, a_0, a_1, a_2), \tag{4.14}$$

where $\sigma_E = 8.5$ keV (20 keV FWHM) as the width of the integration interval. Since uncertainties arise during the Doppler-correction process, e.g., because of limited knowledge about the first interaction point, uncertainties in beam velocity and the exact point of emission of the γ ray, it is expected that the width of the 1191 keV peak is going to be significantly broader than for γ rays emitted from particles at rest. From simulations performed in advance of the experiment, a FWHM of 20 keV was calculated. For simplicity, a Gaussian shape for the expected ^{85}Br peak is assumed. Calculating the integral in Equation (4.14) yields $A_{B,T_1} = 13056$ as well as $A_{B,T_2} = 14142$. A significant peak with A_P counts above the statistical

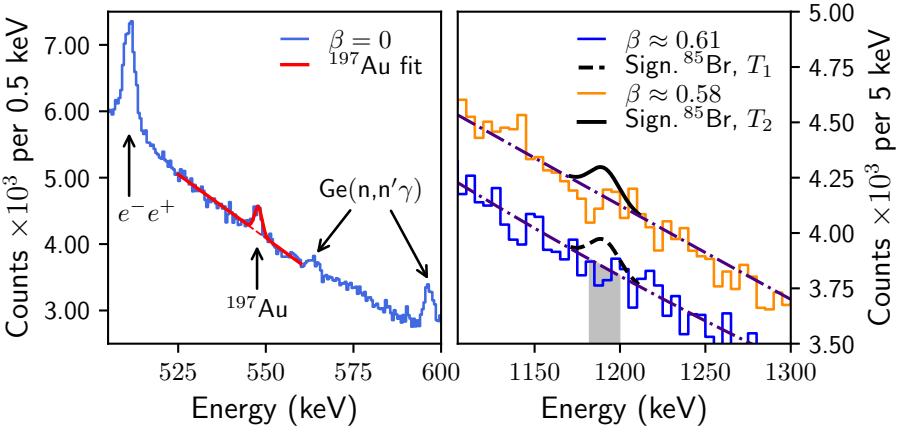

Figure 4.12.: *Left*: Zoom into gated spectrum from Fig. 4.10 around ^{197}Au CoulEx peak. A background subtracted fit on the ^{197}Au peak is depicted in red. *Right*: Doppler-corrected spectra around the energy of the potential spin-flip transition of ^{85}Br. A statistical significant ^{85}Br peak at 1191 keV above the background radiation approximated via a quadratic function (purple) is depicted in black (dashed) for T_1 and black (solid) for T_2. The integration window used for estimating the potential ^{85}Br peak are is shown in gray. Picture adapted from [Nap20b].

fluctuation of the background level, given by

$$\sigma_{B,T_i} = \sqrt{A_{B,T_i}}\,, \tag{4.15}$$

should at least show a 4.653σ difference to the background fluctuation (see [Kno00] for details). Hence,

$$A_{P,T_i} \geq 4.65\sigma_{B,T_i} = 4.65\sqrt{A_{B,T_i}}. \tag{4.16}$$

For the respective targets, this yields $A_{P,T_1} \geq 532$ and $A_{P,T_2} \geq 553$. The potential ^{85}Br peaks are shown in Figure 4.12 (right panel; in black). From this significant

peak, the necessary measured target excitations can be inferred via the assumed ratio of target- to beam-like excitations η, yielding a total of 6999 counts for T_1 and 10708 counts for T_2 in the ^{197}Au peak that are necessary to be able to successfully detect a statistically significant ^{85}Br peak. The ratio of necessary target excitation counts N_{need,T_1} and N_{need,T_2} to actually measured ones N_{meas} is

$$\begin{aligned}\varepsilon &= \frac{N_{\mathrm{need}}}{N_{\mathrm{meas}}} = \frac{\rho_N N_{\mathrm{need},T_1} + (1-\rho_N) N_{\mathrm{need},T_2}}{N_{\mathrm{meas}}} \\ &= \frac{0.45 \times 6999 + 0.55 \times 10108}{2110(370)} \approx 4.3\,(8)\,.\end{aligned} \tag{4.17}$$

Here, the value ρ_N is used to scale the Doppler-corrected spectra to their respective excitation probability as well as to their γ-ray detection efficiencies via

$$\rho_N = \frac{N_{T_1}}{N_{T_1} + N_{T_2}} \frac{\sigma_{\mathrm{Br},T_1}}{\sigma_{\mathrm{Br},T_2}} = \frac{3.9 \times 10^5}{(3.9+4.9) \times 10^5} \frac{4.72\,\mathrm{mb}}{4.64\,\mathrm{mb}} \approx 0.45\,. \tag{4.18}$$

The values N_{T_i} are the amount of photo-absorbed 1191 keV γ rays emitted from the respective targets T_i, Lorentz-transformed and Doppler-shifted according to the corresponding β (see Tab. 4.1) obtained from a *Geant4* simulation using the AGATA simulation code (see also Tab. 4.2).

To estimate the upper limit of the $M1$-transition strength of the $1/2^-_1 \rightarrow 3/2^-_{\mathrm{g.s.}}$ transition, the ratio

$$\kappa = \frac{A_{\mathrm{Au}}}{\rho_N A_{\mathrm{Bg},1} + (1-\rho_N) A_{\mathrm{Bg},2}} \tag{4.19}$$

between the measured ^{197}Au transition γ rays as well as the upper limit of a ^{85}Br peak that cannot be distinguished from the present background within a 95 % confidence interval, given by [Kno00]

$$A_{\mathrm{Bg},i} = 2.33\sqrt{A_{B,T_i}}\,, \tag{4.20}$$

can be used. Via the measured $A_{\mathrm{Au}}, A_{B,T_1}$ and A_{B,T_2}, this ratio is

$$\kappa = 7.8(14)\,. \tag{4.21}$$

The lower boundary $\kappa_< = 7.8-1.4 = 6.4$ yields an estimate on the upper boundary of the excitation cross section at T_2[2] of the beam particles

$$\sigma_{\mathrm{Br},T_2} < \frac{\sigma_{\mathrm{Au},T_2}}{\kappa_<} = 11.4\,\mathrm{mb}\,. \tag{4.22}$$

Using `DWEIKO`, this cross section for T_2 yields an upper limit for the $M1$-transition strength of $B(M1,\downarrow) < 9.5\,\mu_N^2$. Together with the assumed $B(E2,\downarrow) = 1\,\mathrm{W.u.}$, the resulting multipole-mixing ratio $\delta = 0.015$ would still be in the applicable range for *Coulex-multipolarimetry*.

Given that the made assumptions about the transition strengths seen in Section 4.4.1 are valid, the necessary amount of beam time t_{need} fo the used setup can be estimated. Since the amount of measured $^{197}\mathrm{Au}\ 7/2_1^+ \rightarrow 3/2^+_{\mathrm{g.s.}}$ transition γ rays are directly linked to the expected $^{85}\mathrm{Br}\ 1/2_1^- \rightarrow 3/2^-_{\mathrm{g.s.}}$ transition γ rays, it follows that

$$A_{\mathrm{Br}} = \frac{A_{\mathrm{Au}}}{\rho_N\eta_1 + (1-\rho_N)\eta_2} \equiv \zeta A_{\mathrm{Au}}\,, \tag{4.23}$$

where ζ accounts for the different excitation probabilities at T_1 and T_2. Additionally, it follows from Equation (4.16) that

$$A_{\mathrm{Br}} \geq 4.65\left[\rho_N\sqrt{A_{B,T_1}} + (1-\rho_N)\sqrt{A_{B,T_2}}\right]. \tag{4.24}$$

Since any peak area $A_i(t)$ can be expressed in terms of a counting rate $\dot{A}_i(t)$ via

$$A_i(t) = \dot{A}_i(t)t \approx \frac{A_{i,\mathrm{meas}}}{t_{\mathrm{meas}}}t\,, \tag{4.25}$$

where t is the time, $t_{\mathrm{meas}} = 73\,\mathrm{h}$ the measurement time of experiment S426 and $A_{i,\mathrm{meas}}$ a measured peak area (e.g., A_{Au}). From Equations (4.23), (4.24) and (4.25) follows

$$\begin{aligned} t_{\mathrm{need}} &= t_{\mathrm{meas}}\,\frac{4.65^2\left[\rho_N\sqrt{A_{B,T_1}} + (1-\rho_N)\sqrt{A_{B,T_2}}\right]^2}{\zeta^2 A_{\mathrm{Au}}^2} \\ &= 1330(470)\,\mathrm{h}\,. \end{aligned} \tag{4.26}$$

[2] T_2 yields a larger upper boundary of $B(M1,\downarrow)$ than T_1

Table 4.2.: Expected increase of measurable ^{85}Br excitations ν with AGATA 1π. Here, $N_{1\pi}$ are photo-absorbed γ rays with 1191 keV (Doppler-shifted and Lorentz-boosted) in the AGATA 1π setup and N_{PreSPEC} respectively in the PreSPEC setup of AGATA.

Target	$N_{1\pi}$	N_{PreSPEC}	ν
T_1 (@ 0 cm)	1.05×10^6	3.9×10^5	2.70
T_2 (@ 10 cm)	1.38×10^6	4.9×10^5	2.83

Hence, a significant peak of the $1/2^-_1 \rightarrow 3/2^-_{\text{g.s.}}$ transition in ^{85}Br should be measurable in 36−75 days of beam time, given the made assumptions about the transition strengths are correct. Since this is a substantial amount of beam time, it has to be reduced via advances achieved in the development of AGATA.

In comparison to the experimental setup during the PreSPEC campaign in 2014, the amount of available AGATA detectors has significantly increased since then. In the near future, the completion of AGATA 1π [Clé17], consisting of 45 crystals, is anticipated. The influence of almost thrice the amount of detectors on the necessary beam time can be estimated via a *Geant4* simulation. Both AGATA setups, 1π and the PreSPEC configuration, are used to calculate the absorption efficiency of Doppler-shifted and Lorentz-boosted (see Sec. 2.3) bromine excitations with an un-shifted energy of 1191 keV and an isotropically distributed angle Θ between beam direction (assumed to be simply in z-direction) and the emission direction of the γ ray in the center-of-mass frame of the beam nucleus. Comparing the total amount of photo-absorbed γ rays yields

$$\nu = \frac{N_{1\pi}}{N_{\text{PreSPEC}}}, \tag{4.27}$$

where $N_{1\pi}$ is the amount of γ rays photo-absorbed by AGATA 1π and N_{PreSPEC} the amount for γ rays absorbed by AGATA in the PreSPEC configuration. The respective ratios ν for both targets are presented in Table 4.2. Hence, it is anticipated that the total amount of measurable beam-like excitations can be increased by a factor $\nu \in [2.70, 2.83]$ by using AGATA in its 1π configuration. Therefore, the necessary beam time can be reduced to roughly $310 - 648$ hours or $13 - 27$ days.

The analysis of the core energies already highlighted the achieved performance and the necessary increase in beam time. However, AGATA's γ-ray tracking capabilities have been neglected so far. The potential impact of tracking and derived methods is presented in the following.

4.7. Impact of γ-ray Tracking

4.7.1. MGT Analysis

As mentioned in Chapter 3, AGATA has been conceptualized as a γ-ray tracking array. Via γ-ray tracking, a similar analysis to the one shown in Sections 4.5 and 4.6 can be performed. In the following, MGT is used as a tracking algorithm (see Sec. 3.4.4). Similar to Section 4.6, the best ratio ε as a function of the tracking parameter χ^2_{Max} (see Sec. 3.4.4) can be calculated. Figure 4.13 shows the development of ε as a function of χ^2_{Max}. At very low values of χ^2_{Max}, a lot of "good" events are rejected, resulting in a comparatively high ε. With increasing χ^2_{Max}, a potential "sweet-spot" is hit around $\chi^2_{\mathrm{Max}} = 0.08$ where the rate of rejected background events to not-rejected target-excitations is the lowest. For larger values of χ^2_{Max} many target excitations will be accepted. However, many background events are also accepted, yielding a larger ε. The optimal $\chi^2_{\mathrm{Max}} = 0.08$ yields an $\varepsilon = 3.7(6)$. Due to the small acceptance value χ^2_{Max}, many γ rays that do not necessarily stem from the target position such as e^-e^+ annihilation events as well as particle reactions with AGATA are significantly reduced in the tracked spectrum compared to the core spectrum (see Fig. 4.14). This is due to large discrepancies between assumed γ-ray paths, starting from one of the targets, compared to the true physical paths, starting from an unknown position. This yields to a large rejection of such events. However, due to measurement uncertainties, it is still possible that background γ rays are interpreted as γ rays that were emitted from the target position (see Sec. 3.4.4). The achieved Peak-to-Background (P/B) ratios, quantifying the ratio of background-subtracted counts in a peak to the amount of counts in the subtracted background, are shown in Figure 4.13 (right). As expected, the largest P/B ratio is reached for $\chi^2_{\mathrm{Max}} = 10^{-3}$, where most of the background events are rejected. The core analysis reached a $P/B_{\mathrm{core}} = 5.6(9)\,\%$ whereas for $\chi^2_{\mathrm{Max}} = 0.08$, a $P/B_{\mathrm{track}} = 6.1(10)\,\%$ was reached.

The achieved performance via γ-ray tracking in addition to the impact of AGATA 1π yield a necessary beam time of $237-468$ hours or $10-19$ days instead of up

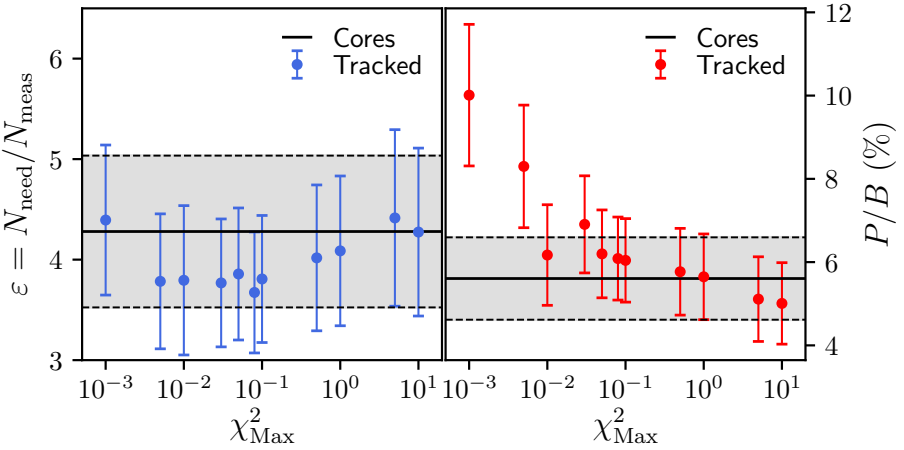

Figure 4.13.: *Left*: Detection limit ratios ε for various χ^2_{Max} parameters of MGT (blue). The achieved ε for directly using core energies (see Secs. 4.5 and 4.6) is depicted as a black line with respective uncertainties as dashed lines. *Right*: Achieved Peak-to-Background (P/B) ratios as a function of χ^2_{Max} for tracked γ rays in red and for the core-energy analysis in black. Picture adapted from [Nap20b].

to 27 days achieved in the core analysis.

Since the point of emission of the 547.5 keV γ rays of the $7/2^+_1 \rightarrow 3/2^+_{\mathrm{g.s.}}$ transition in gold is practically known from the target positions and the beam-spot measurements from LYCCA, a target identification could be performed using γ-ray tracking methods. This is presented in the following.

4.7.2. Target Reconstruction

A possible approach for further reducing undesired background events is a target identification via γ-ray tracking. Therefore, the first two interaction points $\vec{x}_1$ and $\vec{x}_2$ of the incident γ rays calculated by MGT as well as the two possible target

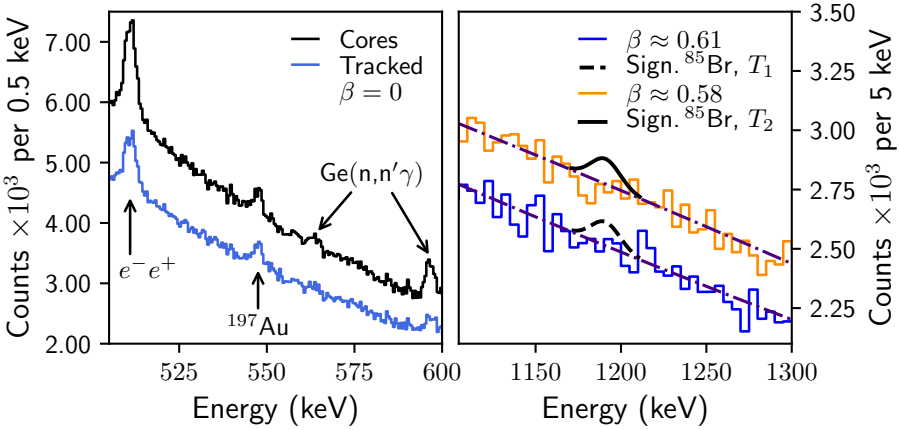

Figure 4.14.: *Left*: Comparison between core spectrum (black) and γ-ray tracked spectrum with MGT for $\chi^2_{\text{Max}} = 0.08$ (blue). A decrease in overall statistics in the tracked spectrum is present. However, the P/B-ratio (see Fig. 4.13) increases. *Right*: Doppler-corrected spectrum around the expected ^{85}Br peak for T_1 (blue) and T_2 (orange). Statistically significant ^{85}Br peaks are depicted in black (dashed) for target T_1 and in black (solid) for target T_2. Picture adapted from [Nap20b].

positions $\vec{s}_1$ and $\vec{s}_2$ are used. Here

$$\vec{s}_i = (x_B, y_B, z_i)^\intercal \,, \quad \text{with} \quad i \in \{1, 2\} \,, \tag{4.28}$$

where $z_1 = 0\,\text{mm}$ and $z_2 = 100\,\text{mm}$ are the target positions along the beam-line. In addition, $x_B = -0.64\,\text{mm}$ and $y_B = -2.06\,\text{mm}$ are the mean x and y coordinates of the beam-spot on the target DSSSD taken from a non-linear regression assuming a Gaussian distribution on the measured beam-profile. From these regressions, the respective beam widths in x and y can be extracted. They are $\sigma_x = 14.5\,\text{mm}$ and $\sigma_y = 7.4\,\text{mm}$. The uncertainties in z-direction are given by the respective target thicknesses d_i (see Sec. 4.3) via

$$\sigma_{z_i} = \frac{1}{2}\frac{d_i}{\rho_{\text{Au}}} \,, \tag{4.29}$$

where $\rho_{\mathrm{Au}} = 19.3\,\mathrm{g/cm^3}$ is the mass density of gold. The factor 1/2 is used to account for the width of the targets from their centers to the left and right border. Hence, the uncertainties are $\sigma_{z_1} = 0.52\,\mathrm{mm}$ and $\sigma_{z_2} = 0.26\,\mathrm{mm}$. From the assumed emission positions $\vec{s}_1$ and $\vec{s}_2$, the respective probabilities of the measured γ rays stemming from target one or two can be modelled via the probability density

$$\varrho(\alpha_i, \theta) = \frac{1}{\sqrt{2\pi}\sigma_{\alpha_i,\theta}} \exp\left(-\frac{(\alpha_i - \theta)^2}{2\sigma^2_{\alpha_i,\theta}}\right). \tag{4.30}$$

Here, the angle α_i is given by the measured interaction points $\vec{x}_1$ and $\vec{x}_2$ and the potential source position $\vec{s}_i$ is given by

$$\cos(\alpha_i) = \frac{\langle \vec{x}_1 - \vec{s}_i, \vec{x}_2 - \vec{x}_1 \rangle}{||\vec{x}_1 - \vec{s}_i|| \cdot ||\vec{x}_2 - \vec{x}_1||}. \tag{4.31}$$

The angle θ is defined via the assumed incident γ-ray energy E_γ calculated by MGT and the deposited energy E_{dep} at $\vec{x}_1$ using the Compton-scattering formula (see Eq. (3.2)). The uncertainties of position and energy-resolution are taken into account via $\sigma^2_{\alpha_i,\theta} = \Delta\alpha_i^2 + \Delta\theta^2$. The uncertainties $\Delta\alpha_i$ and $\Delta\theta$ are calculated using Gaussian uncertainty propagation of Equations (4.31) and (3.2). For $\Delta\alpha_i$, the uncertainties in the source position are given by σ_x, σ_y and σ_{z_i}. For AGATA's position resolution, an uncertainty of 5 mm FWHM [Rec09b, Söd11] is assumed. As AGATA's energy resolution, 0.2% E_{dep} FWHM is assumed [Akk12]. To quantify the degree of target identification, an asymmetry

$$A_{1,2} := \frac{\varrho(\alpha_1, \theta) - \varrho(\alpha_2, \theta)}{\varrho(\alpha_1, \theta) + \varrho(\alpha_2, \theta)}, \quad \text{with} \quad A_{1,2} \in [-1, 1], \tag{4.32}$$

can be defined. Here, $A_{1,2} = 1$ for an identification as target one and $A_{1,2} = -1$ for target two. For simulated 547.5 keV γ rays that are either emitted from target one or two using AGATA's PreSPEC configuration, $A_{1,2}$ is depicted in Figure 4.15. Most of the γ rays cannot be assigned to a target. This is mainly due to the assumption of free, non-moving electrons which is done in the γ-ray tracking process (see Eq. (3.2)), as well as large uncertainties in α_i for closely lying interaction points that yield to problems in the target identification process even for the ideal case of a *Geant4* simulation. Due to the exponentially-declining behavior of the travel distance of γ rays in matter (see Sec. 3.4.2), small distances between interaction points especially contribute to the low statistics in identified target positions.

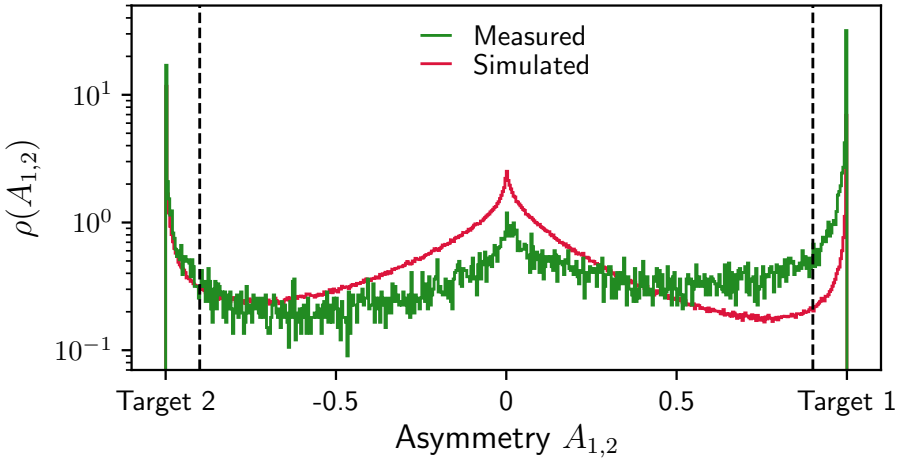

Figure 4.15.: Probability densities $\rho(A_{12})$ of asymmetries $A_{1,2}$ for simulated γ rays (red) and measured γ rays (green). Only γ rays that yielded $\varrho(\alpha_k, \theta) \geq 10^{-3}$ with $k = 1 \vee 2$ are used to ensure events with small uncertainties. Only measured γ rays with a total energy deposition $E_\gamma = (547.5 \pm 2)\,\mathrm{keV}$ were used.

As a threshold for the respective target asymmetries, a value of $|A_{1,2}| \geq 0.9$ was used. In this range, ∼16 % of all simulated 547.5 keV γ rays are situated. In addition, a threshold on the respective $\varrho(\alpha_k, \theta) \geq 10^{-3}$ with $k = 1 \vee 2$ as the index of the identified target is used to suppress events, where large uncertainties in tracking are present. For $\chi^2_{\mathrm{Max}} = 0.08$, the resulting spectrum is shown in Figure 4.16. Although the background radiation is strongly reduced in this scenario, a ^{197}Au peak with 200(120) counts with $P/B = 5(3)\,\%$ is present. The amount of events in the background beneath the peak is $N_{\mathrm{Bg}} = 3858$ with statistical fluctuation $\sigma_{\mathrm{Bg}} = \sqrt{N_{\mathrm{Bg}}} = 62$. Hence, the ^{197}Au peak differs from the background fluctuation only within a 70 % confidence interval which renders the peak questionable in a statistical sense. In literature, a confidence interval ≥ 95 % is usually applied to probe the significance of a peak (see [Kno00]). The small amount of measured events is caused by larger uncertainties in position resolution present

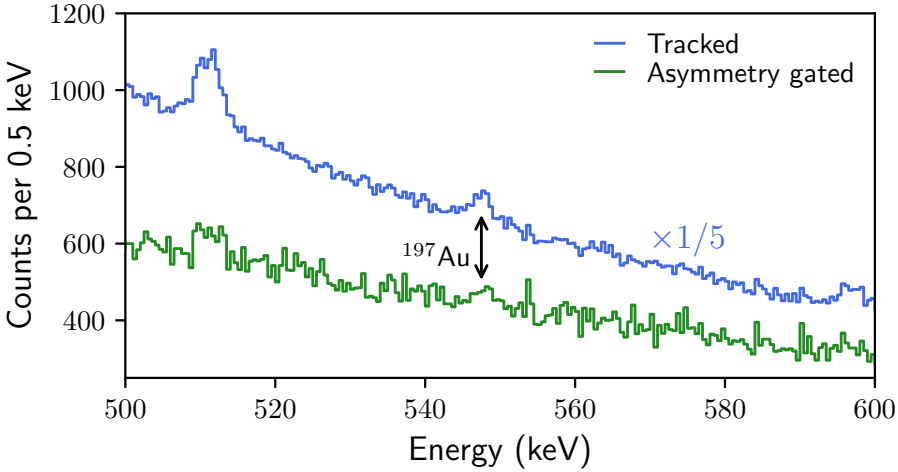

Figure 4.16.: MGT spectrum for $\chi^2_{\mathrm{Max}} = 0.08$ (see Fig. 4.14) scaled by 1/5 (blue) and asymmetry-gated γ rays with $\varrho(\alpha_k, \theta) \geq 10^{-3}$ with $k = 1 \vee 2$ and $|A_{1,2}| \geq 0.9$ (green). After applying the asymmetry condition, only a $e^- e^+$ annihilation peak as well as the ^{197}Au remain in the spectrum. The significance of the ^{197}Au is discussed in the text.

in the experiment, compared to the simulation, which ultimately yield to more γ rays being rejected in the assignment process. Whether or not a target identification for such an experiment is possible via the proposed method is not known due to the lack of statistics in the ^{197}Au peak.

An inverted approach, a so-called Compton-camera approach, to the target reconstruction has also been performed. However, due to the setup of two consecutive targets, unwanted mapping effects arise which strongly hinder the target reconstruction process. Since the x and y coordinates are known due to the beam-spot measurement via the TargetDSSSD of LYCCA, the asymmetry approach is superior to the Compton-camera approach. For details on the Compton-camera approach and its mapping problems, see Appendix C.

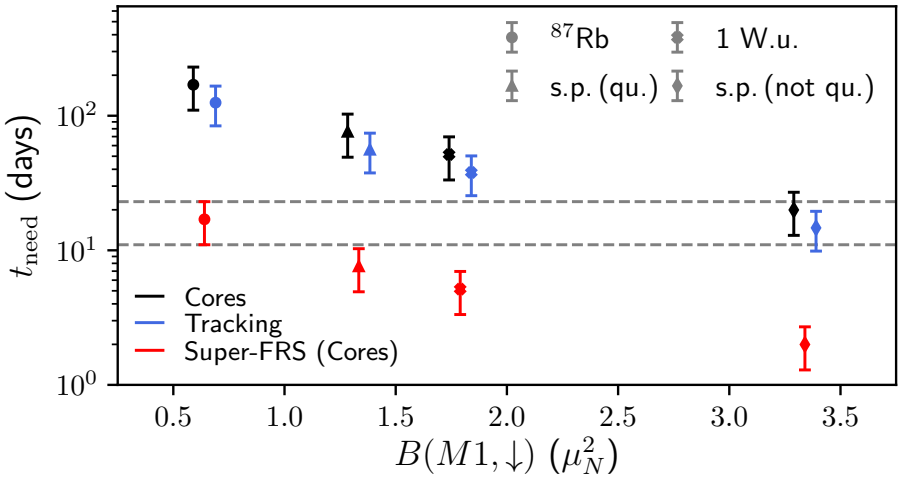

Figure 4.17.: Necessary measurement time t_{need} for a significant ^{85}Br peak as a function of $B(M1,\downarrow)$ for $B(M1,\downarrow) = 0.64\,\mu_N^2$ as measured in ^{87}Rb (dots), 1 W.u. (crosses), a single particle transition with quenched g_s^π (triangles) and without a quenched g_s^π (diamonds). Black depicts t_{need} for the performed core analysis (see Sec. 4.6), blue for the MGT analysis (see Sec. 4.7.1) and red for the assumed performance of the Super-FRS (for core analysis). If the background would be reducible by a factor of ten via the Super-FRS, a significant ^{85}Br peak for $B(M1,\downarrow) = 0.64\,\mu_N^2$ would be measurable in a similar amount of beam time as for a $B(M1,\downarrow) = 3.34\,\mu_N^2$ using the FRS. $B(M1,\downarrow)$ values for core and MGT analysis slightly offset for better visibility. Picture adapted from [Nap20b].

4.8. Impact of $M1$-transition Strength Assumptions

Although a measurement time of down to 10−19 days (see Sec. 4.7.1) seems reasonable, this value strongly depends on the assumed $B(M1,\downarrow)$ value (see Fig. 4.17). In the case of a similar transition strength as measured in ^{87}Rb with $B(M1,\downarrow) =$

$0.64^{+8}_{-5}\,\mu_N^2$, the necessary measurement time would increase to $t_{\text{need}} = 170(69)\,\text{d}$, which is not justifiable anymore. However, since future experiments will most likely operate on novel machines such as the Super-FRS [Gei09], the successor of the FRS at the Facility for Anitproton- and Ion-Research (FAIR), the necessary beam time will most likely decrease significantly. Assuming that the measured background radiation induced by the Super-FRS is one order of magnitude less than for the FRS, t_{need} would be reduced by that same factor. This results in the potential measurement of the $\pi p_{3/2} \rightarrow p_{1/2}$ spin-flip excitation in ^{85}Br with an assumed $B(M1,\downarrow) = 0.64\,\mu_N^2$ in a similar time as achievable with the FRS for an assumed $B(M1,\downarrow) = 3.34\,\mu_N^2$.

5. An Experimental Approach to γ-ray Tracking

γ-ray tracking methods like MGT or OFT (see Sec. 3.4.4) are already very potent experimental techniques. However, one of their theoretical foundations, the assumption of a single interaction at a measured point is only partially valid. In the following, one of the major flaws in γ-ray tracking methods is emphasized, spatially induced tracking performance restraints.

The work presented in this Chapter is based on [Nap20a].

5.1. The Pitfall of γ-ray Tracking

The biggest influence on the achievable tracking performance is based on the used PSA methods (see Sec. 3.2.1). For a given γ-ray energy E'_γ after a scattering at $\vec{x}_i$, the probability density for a traveled distance d through matter is given by the respective mean free path (see Eq. (3.8)). Hence, most of the time, γ rays interact with matter very close to their first interaction, called $\vec{x}_{i+1}$ for now. The typical energies of γ rays after their first interaction in AGATA lie in the range of a few 100 keV, given an incident γ-ray energy of about 1 MeV. For these energies, the mean free path is around $20-30$ mm. Due to AGATA's detector crystal segments having similar dimensions (see Sec. 3.3), the probability of two consecutive interactions lying in a single segment is non-negligible. For these types of events, the standard PSA methods are not suited to correctly reconstruct them as two consecutive interactions. Usually, these events are reconstructed as a single interaction with a total deposited energy

$$E_{\mathrm{dep,tot}} = E_{\mathrm{dep},i} + E_{\mathrm{dep},i+1}\,. \tag{5.1}$$

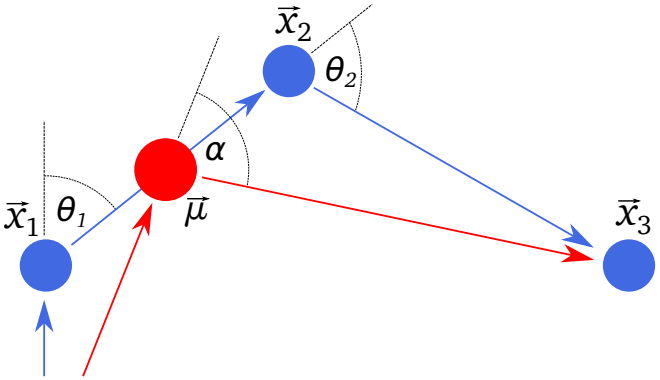

Figure 5.1.: PSA-induced Compton-scattering problem for two interactions at $\vec{x}_1$ and $\vec{x}_2$ with respective deposited energies $E_{\text{dep},1}$ and $E_{\text{dep},2}$ in a single segment. Although $E_{\text{dep},1}$ and $E_{\text{dep},2}$ fit their scattering angles θ, the merged interaction point at $\vec{\mu}$ with respective scattering angle α does not necessarily fit its total deposited energy related angle given by $E_{\text{dep},1} + E_{\text{dep},2}$.

If the γ ray is photo-absorbed in its second interaction, the γ-ray tracking is not strongly influenced by a possible interaction-point merging. However, if the γ ray is again Compton-scattered at the second interaction, the merging of interaction points alters the relation between true and assumed γ ray behavior in the detector. Given the scenario of a perfectly performing PSA, the true deposited energies $E_{\text{dep},i}$ and $E_{\text{dep},i+1}$ are directly linked to the scattering angles θ_i at $\vec{x}_i$ and θ_{i+1} at $\vec{x}_{i+1}$ via the Compton-scattering equation (see Eq. (3.2)). In the case of a merging of interaction points, $\vec{x}_i$ and $\vec{x}_{i+1}$ are merged into a single interaction point $\vec{\mu}$ with the total deposited energy $E_{\text{dep,tot}}$. Although the position based scattering angle α does not necessarily change significantly, the relation between α and $E_{\text{dep,tot}}$ is not given by the Compton-scattering equation anymore, but is rather randomly distributed. For these types of events, the γ-ray tracking performance is lowered significantly. In general, the interaction-point merging is moderated by the position based scattering angle uncertainty σ_{ϑ_i} (see Eq. (3.16)). However, for deposited energies close to the Compton edge, the γ-ray path cannot be described by means of a single Compton scattering anymore. This behavior is shown

exemplarily in Figure 5.2 for simulated incident γ rays with an energy of 661.7 keV that interacted thrice with corresponding deposited energies $E_{\mathrm{dep},1}$, $E_{\mathrm{dep},2}$ and $E_{\mathrm{dep},3}$ until being fully absorbed, meaning $E_\gamma = E_{\mathrm{dep},1} + E_{\mathrm{dep},2} + E_{\mathrm{dep},3}$. The γ rays have been simulated using the AGATA simulation code for *Geant4*. Figure 5.2 depicts the deposited energies at the first $E_{\mathrm{dep},1}$ and second interaction $E_{\mathrm{dep},2}$ and their respective sums $E_{\mathrm{dep},1+2}$. The distance $d_{1,2}$ between the first two interaction points has been limited to $d_{1,2} \leq 2.12\,\mathrm{mm}$ (5 mm FWHM) where a merge of interaction points is likely. It is assumed here, that both interactions lie in the same segment. Given the geometrical design parameters of AGATA's detector segments (see Sec. 3.3), this assumption holds approximately. Roughly 53 % of all merged events lie above the Compton edge at around 477 keV. This strongly hinders a correct tracking since the Compton edge is the theoretical limit for maximum depositable energy. Although stemming from a single γ ray, the used γ-ray tracking algorithm will most likely identify the measured data set as being created by two (or more) incident γ rays, if the preset thresholds of the tracking algorithms are not fulfilled for the case of a single γ ray (see Sec. 3.4.4). However, if the interaction points corresponding to $E_{\mathrm{dep},2}$ and $E_{\mathrm{dep},3}$ are merged, the tracking process is not hindered since only a photo-absorption with a larger deposited energy occurs at the end of the interaction point sequence. The issue of PSA-induced interaction-point clustering (see, e.g., Fig. 16 in [KL19]) and its influence on the achievable γ-ray tracking performance is neglected in the following.

5.2. `ExpTrack` – Novel γ-ray Tracking Approach

As mentioned in Section 5.1, the γ-ray tracking performance is diminished by incorrect assumptions in PSA-performance behavior. To cover these problems, an improved PSA method would be the best solution. However, research on this matter is still ongoing and has not yet solved the position-merging enigma. To bypass PSA induced issues, a novel tracking approach called `ExpTrack`, short for Experimental Tracking, is presented in the following.

5.2.1. Geometrical Scattering Angle Uncertainty Modeling

Although conventional tracking algorithms perform well applying a Gaussian uncertainty propagation approach (see Sec. 3.4.3), this approach does not correctly

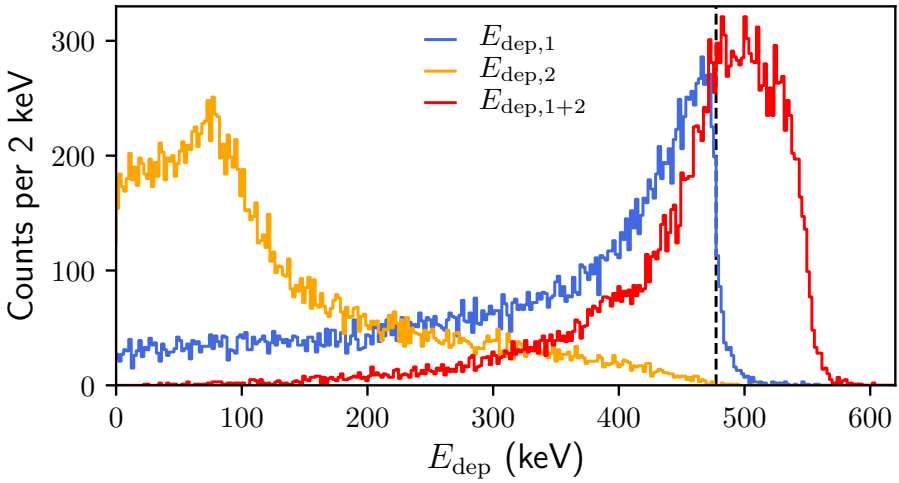

Figure 5.2.: Deposited energies E_{dep} for simulated γ rays with an incident energy of 661.7 keV that interacted three times until being absorbed. Deposited energy at the first interaction in blue, at the second interaction in orange and their respective sum in red. The distance $d_{1,2}$ between the interaction points is limited to $d_{1,2} \leq 2.12$ mm – the achieved position resolution of the PSA. The Compton edge at 477 keV is depicted as black dashed line. Roughly 53 % of all merged events (red) lie above the Compton edge. Figure adapted from [Nap20a].

reproduce the scattering behavior at very small ($\sim 0°$) or very large ($\sim 180°$) angles. To correctly parameterize this behavior, a Monte Carlo simulation is used. Since the Euclidean norm as well as the dot product are invariant under arbitrary rotational and translational transformations in $\mathbb{R}^3$, the uncertainty in the geometrical scattering angle ϑ between three randomly selected points $\vec{r}_0$, $\vec{r}_1$ and $\vec{r}_2$ in

$\mathbb{R}^3$ can be modeled using only three parameters, namely $d_{0,1}$, $d_{1,2}$ and ϑ itself, via

$$\vec{r}_0 = \begin{pmatrix} 0 \\ 0 \\ 0 \end{pmatrix}, \quad \vec{r}_1 = \begin{pmatrix} d_{0,1} \\ 0 \\ 0 \end{pmatrix}, \quad \vec{r}_2 = \begin{pmatrix} d_{0,1} + d_{1,2}\cos(\vartheta) \\ d_{1,2}\sin(\vartheta) \\ 0 \end{pmatrix}. \tag{5.2}$$

Here, $d_{0,1}$ corresponds to the distance between $\vec{r}_0$ and $\vec{r}_1$, $d_{1,2}$ to the distance between $\vec{r}_1$ and $\vec{r}_2$ and ϑ to the angle between $\vec{r}_1 - \vec{r}_0$ and $\vec{r}_2 - \vec{r}_1$ (see Eq. (3.10)). For any given set of $d_{0,1}$, $d_{1,2}$ and ϑ, the uncertainty in ϑ due to the finite position resolution of AGATA can be inferred by sampling random points $\vec{\mu}_i$ around each respective $\vec{r}_i$ ($i \in \{0,1,2\}$). The random points are taken from a multivariate normal distribution $\mathcal{N}_{3D}(\vec{r}_i, \Sigma_X)$ with mean $\vec{r}_i$, covariance matrix $\Sigma_X = \mathbb{1} \cdot \sigma_X^2$ and standard deviation $\sigma_X = 2.12\,\text{mm}$ (5 mm FWHM). Defining the scattering angle ψ as the angle between one set of $\vec{\mu}_0$, $\vec{\mu}_1$ and $\vec{\mu}_2$, the uncertainty in ϑ for one set of $d_{0,1}$ and $d_{1,2}$ can be expressed by means of a probability density distribution $\rho_\vartheta(\cos(\psi))$.

In Figure 5.3, an example case of those probability densities $\rho_\vartheta(\cos(\psi))$ for $d_{0,1} = d_{1,2} = 12\,\text{mm}$ for various values of ϑ is shown. Especially at small and large ϑ, a strong deviation from a Gaussian distribution can be seen. For example, in the case of $\vartheta = 0°$, a random set of $\vec{\mu}_0$, $\vec{\mu}_1$ and $\vec{\mu}_2$ has to be aligned in a straight line to yield a scattering angle of 0°. Depending on the distances $d_{0,1}$ and $d_{1,2}$, this can be comparatively unlikely compared to all other possible configurations (see Fig. 5.4).

5.2.2. Experimental Compton-scattering Database

To incorporate the physical aspect of Compton scattering into the `ExpTrack` framework, a ^{137}Cs source run of the experiment *e673* conducted at GANIL in May/June 2017, using AGATA, consisting of 30 HPGe detectors at that time, with $\sim 6 \cdot 10^7$ events was used. The measured spectrum is shown in Figure 5.5. From this measurement, 80 % of all events were used in the following probability density construction. The remaining 20 % are used for performance tests (see Sec. 5.3). The 80/20 ratio is used to access rare events in the calculations of $\rho_{E_{\text{dep}}}(\cos(\psi))$ (see below) while still ensuring a large enough test set for the benchmark test performed in Section 5.3. In the following, only γ rays with a total deposited energy $E_{\text{dep,tot}} = (661.7 \pm 2)\,\text{keV}$ that interacted $2 \leq N \leq 10$ times were

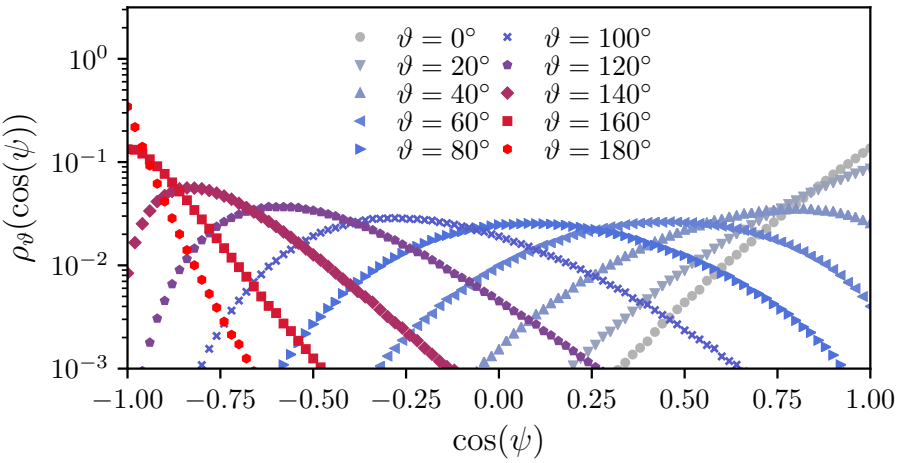

Figure 5.3.: Distributions of $\rho_\vartheta(\cos(\psi))$ for various ϑ (color-coded, see legend) for $d_{0,1} = d_{1,2} = 12\,\text{mm}$. A strong deviation from a Gaussian distribution occurs especially at small and large angles.

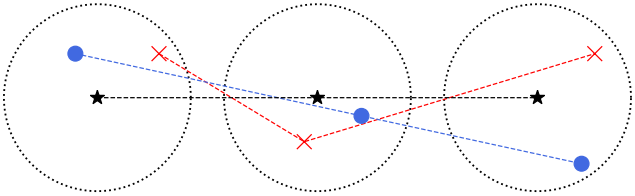

Figure 5.4.: Configurations of $\vec{\mu}_0$, $\vec{\mu}_1$ and $\vec{\mu}_2$ for the true interaction points $\vec{r}_0$, $\vec{r}_1$ and $\vec{r}_2$ (black stars) with their uncertainty σ_X (dotted circles). The true scattering angle between those $\vec{r}_i$ is $\vartheta = 0°$. Only those $\vec{\mu}_i$ configurations arranged in a straight line (blue dots) will yield the correct angle ϑ. All others (red crosses) yield an incorrect angle.

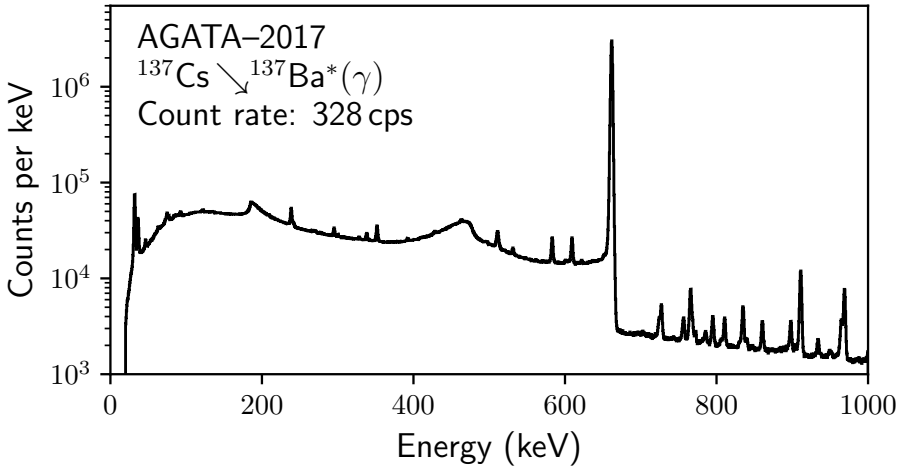

Figure 5.5.: Measured ^{137}Cs source spectrum in May/June 2017 during experiment *e673* at GANIL. In total, 30 AGATA crystals with full addback have been used. The counting rate was $\sim$ 328 counts per second. Figure adapted from [Nap20a].

used. To map the experimental tracking behavior, the first and second interaction point of the incident γ ray has to be identified. From their measured positions $\vec{r}_1$ and $\vec{r}_2$ and the known source position $\vec{r}_0$, the geometrical scattering angle ψ is calculated via Equation (3.10). Together with the measured deposited energy E_{dep}, a probability density distribution $\rho_{E_{\text{dep}}}(\cos(\psi))$ is formed. Given the small probability of multiple γ rays causing the deposited energy $E_{\text{dep,tot}} = (661.7 \pm 2)\,\text{keV}$ for the comparatively small event rate of 328 cps of the source measurement, falsely assigned events such as two 661.7 keV γ rays coincidentally depositing a total energy of $E_{\text{dep,tot}}$ are negligible for the calculation of $\rho_{E_{\text{dep}}}(\cos(\psi))$ since they are comparatively rare. The resulting probability density is shown in Figure 5.6. Similar to Section 5.2.1, the position- and energy-resolution based uncertainty in E_{dep} is expressed by means of $\cos(\psi)$. As shown in Figure 5.6, for energies below the classical Compton edge at 477 keV, the limit of free electrons at rest (black dashed line) describes the scattering quite well. However, at energies above the Compton

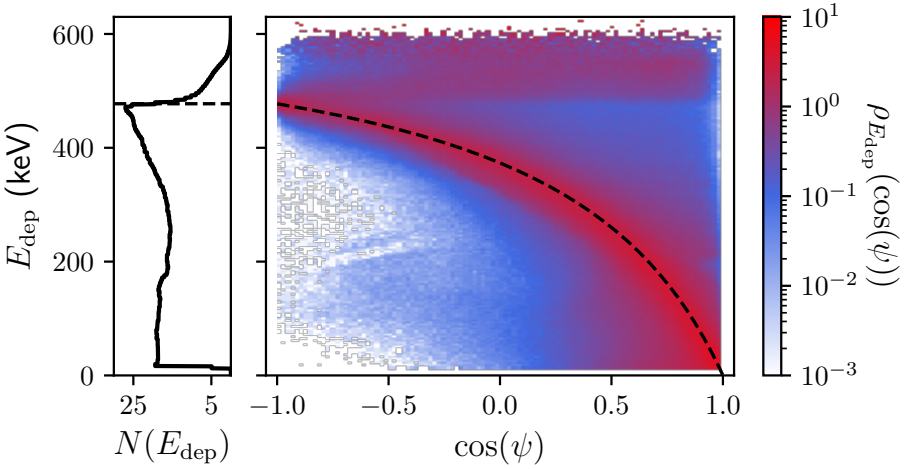

Figure 5.6.: Experimental probability densities $\rho_{E_{\mathrm{dep}}}$ of Compton scattering with AGATA for incident γ rays with an energy of 661.7 keV. The black dashed line marks the Compton-scattering limit of free electrons at rest. Especially at high deposited energies E_{dep} above the Compton edge at 477 keV, almost all scattering angles $\cos(\psi)$ are possible. Each row's area of the matrix plot is normalized to one by the normalization function $N(E_{\mathrm{dep}})$ displayed at the left side of the matrix plot. Figure adapted from [Nap20a].

edge, the mentioned interaction point merging allows for almost all scattering angles $\cos(\psi)$ for a given deposited energy. The performance of this approach strongly depends on the correct identification of the first two interaction points. At the moment, this is done via OFT (see Sec. 3.4.4). Here, the possible first two interactions that yield the highest figure of merit are chosen to be the most likely first interactions of the incident γ ray. Deposited energies close to the Compton edge are most likely the first interaction.

5.2.3. The `ExpTrack` Algorithm

To incorporate purely geometric (see Sec. 5.2.1) and PSA-induced effects (see Sec. 5.2.2), the various probability density distributions are merged into joint probability density distributions $P(E_{\mathrm{dep}}, \vartheta)$. For a given set of E_{dep} and ϑ, the joint probability density is given by

$$P(E_{\mathrm{dep}}, \vartheta) = N \int_{-1}^{1} \mathrm{d}\cos(\psi)\, \rho_{E_{\mathrm{dep}}}(\cos(\psi)) \cdot \rho_{\vartheta}(\cos(\psi)), \tag{5.3}$$

with N as a normalization constant such that

$$\int_{0^\circ}^{180^\circ} \mathrm{d}\vartheta\, P(E_{\mathrm{dep}}, \vartheta) \equiv 1\,. \tag{5.4}$$

Since all possible Compton-scattering scenarios for a given incident γ-ray energy E_γ can be calculated beforehand, the act of γ-ray tracking boils down to identifying the interaction point distances $d_{0,1}$ and $d_{1,2}$, calculating their geometrical scattering angle ϑ and checking whether it lies between preset boundaries of ϑ given the deposited energies. These boundaries, called ϑ_{min} and ϑ_{max}, can be calculated starting from the respective peak positions $\vartheta_{\mathrm{peak}}$ in a given $P(E_{\mathrm{dep}}, \vartheta)$. From this point, the total area P_A between ϑ_{min} and ϑ_{max} is iteratively calculated while increasing (decreasing) ϑ_{max} (ϑ_{min}) via

$$P_A = \int_{\vartheta_{\mathrm{min}}}^{\vartheta_{\mathrm{peak}}} \mathrm{d}\vartheta\, P(E_{\mathrm{dep}}, \vartheta) + \int_{\vartheta_{\mathrm{peak}}}^{\vartheta_{\mathrm{max}}} \mathrm{d}\vartheta\, P(E_{\mathrm{dep}}, \vartheta), \tag{5.5}$$

until P_A reaches a predefined value P_{max}, set to $P_{\mathrm{max}} = 0.95$ for now. Here, $0^\circ \leq \vartheta_{\mathrm{min}} < \vartheta_{\mathrm{max}}$, $\vartheta_{\mathrm{max}} \leq 180^\circ$ and $\vartheta_{\mathrm{min}} < \vartheta_{\mathrm{peak}} < \vartheta_{\mathrm{max}}$.

As an example case, joint probability densities for $d_{0,1} = d_{1,2} = 4\,\mathrm{mm}$ and $d_{0,1} = d_{1,2} = 120\,\mathrm{mm}$ for $E_{\mathrm{dep}} = 120, 360$ and $520\,\mathrm{keV}$ are shown in Figure 5.7. Since $\vec{r}_0$, $\vec{r}_1$ and $\vec{r}_2$ are very close compared to AGATA's position resolution in Figure 5.7 (left), the resulting joint probability densities are very broad. With increasing distance between the points, the peak centers shift and the boundary widths decrease significantly due to the smaller influences of uncertainties in ϑ.

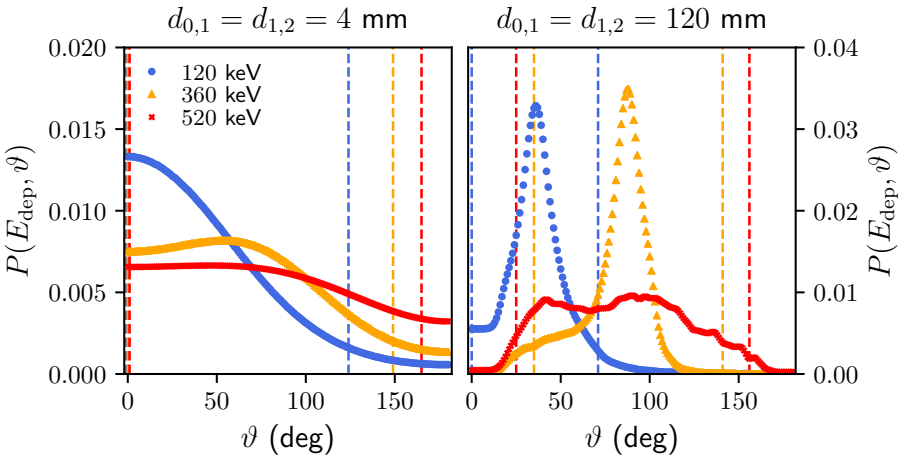

Figure 5.7.: Joint probability density distributions as a function of ϑ for $d_{0,1} = d_{1,2} = 4\,\mathrm{mm}$ (left) and $d_{0,1} = d_{1,2} = 120\,\mathrm{mm}$ (right) for deposited energies $E_{\mathrm{dep}} = 120, 360$ and $520\,\mathrm{keV}$. The mentioned boundaries (details see text) are visualized as dashed lines and are centered around each distributions respective maximum. On the left,the lower boundaries ϑ_{min} all lie at 0° but have been offset slightly for better visibility. Figure adapted from [Nap20a].

5.3. First Experimental Benchmarks with ^{137}Cs

To test the performance of `ExpTrack`, the remaining 20 % of the mentioned ^{137}Cs source measurement (see Sec. 5.2.2) have been used. Only events with a total deposited energy of $E_{\mathrm{dep,tot}} = (661.7 \pm 2)\,\mathrm{keV}$ were analyzed. Since only γ rays with an incident energy $E_\gamma = 661.7\,\mathrm{keV}$ were analyzed beforehand (see Sec. 5.2.2), only events with a total of $N = 2$ interaction points can be used for the benchmark test. For $N > 2$, the γ ray's scattering dynamics after the first interaction cannot be correctly described by the calculated joint probability density distributions anymore since the remaining γ-ray energy yields a different Compton-scattering behavior. Additional source measurements with different incident γ-ray

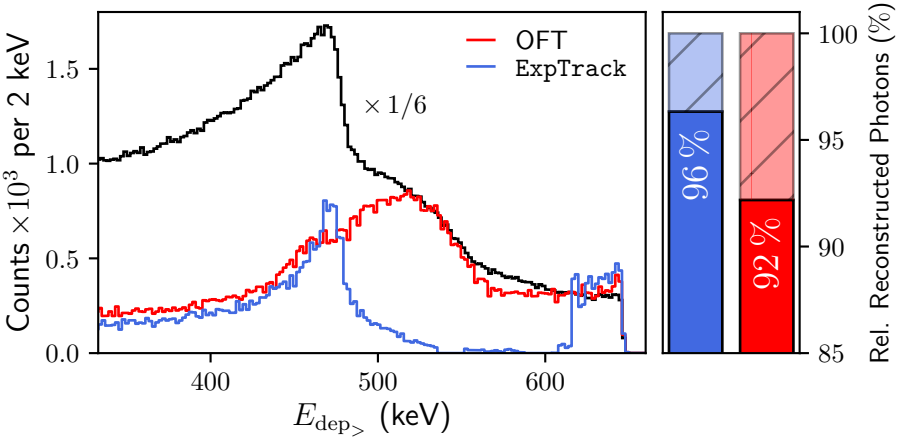

Figure 5.8.: *Left*: Distribution of largest deposited energy $E_{\mathrm{dep}_>}$ from the set $\{E_{\mathrm{dep},1}, E_{\mathrm{dep},2}\}$ for all events with $E_{\mathrm{dep,tot}} = (661.7 \pm 2)\,\mathrm{keV}$ and $N = 2$ (black, scaled by factor of 1/6) and distributions of deposited energy $E_{\mathrm{dep}_>}$ for non-reconstructed events (`ExpTrack` in blue, OFT in red). *Right*: Respective reconstruction rates of used tracking methods relative to all events in %. Figure adapted from [Nap20a].

energies are needed for this. `ExpTrack` is compared to OFT. The parameters of OFT are set to *sigma_theta* = 0.8, *minprobsing* = 0.02 and *minprobtrack* = 0.05 (see Sec. 3.4.4). Given the condition $E_{\mathrm{dep,tot}} = (661.7 \pm 2)\,\mathrm{keV}$, roughly 40 % of all incident γ rays interacted twice. These types of events often showed a deposited energy close to the Compton edge at 477 keV at their first interaction (see Fig. 5.8). In this energy range, conventional tracking methods tend to struggle due to the mentioned reasons in Section 5.2.2. OFT's and `ExpTrack`'s tracking performance is shown in Figure 5.8 as a function of $E_{\mathrm{dep}_>} = \max(E_{\mathrm{dep}_1}, E_{\mathrm{dep}_2})$. All events processed by the respective tracking algorithms are shown in black. Events that were not correctly tracked (OFT: red, `ExpTrack`: blue) are also shown. A γ ray is not correctly tracked, if it is not physically possible that all permutations of the measured interaction points in a single event stem from one γ ray, given the deposited energies, the assumed Compton-scattering dynamics and the as-

sumption of an incident γ-ray energy $E_\gamma = 661.7\,\text{keV}$. As depicted in Figure 5.8, `ExpTrack` correctly reconstructs 96.3 % of all events, whereas OFT reaches a total of 92.1 %. Both tracking algorithms, however, also show weaknesses in different parts of their respective spectra. OFT mostly struggles in the energy range of 480-550 keV, where interaction point merging predominately influences γ-ray tracking (see Sec. 5.2.2). Since this effect introduces discrepancies between measured and assumed tracking behavior, OFT has to decide whether a single photon or two incident photons have deposited the measured energies. Depending on the tracking parameter *minprobsing* and the remaining $E_{\text{dep}_<} = E_{\text{dep,tot}} - E_{\text{dep}_>}$, the scenario of two incident photons might be more likely than a single photon scenario, even if the measured events do stem from a single γ ray. In contrast, `ExpTrack` especially struggles at energies lower than the Compton edge at 477 keV and at energies above 600 keV. Close to the Compton edge, the probability density distribution $\rho_{E_{\text{dep}}}$ (see Fig. 5.6) is sharply distributed around the classical Compton limit close to the Compton edge. Thus, even small deviations from the limit yield incorrectly tracked γ rays. The performance decrease manifesting in a large amount of untracked events at high $E_{\text{dep}_>}$ is caused by an absence of events in $\rho_{E_{\text{dep}}}$ at high deposited energies close to the full energy deposition (see Fig. 5.6).

5.4. Possible Improvements for `ExpTrack`

Although `ExpTrack` is already performing quite well, it is far from being complete. In total, there are two major fields for improvement – the need of a γ-ray energy database of incident γ rays as well as a geometrical clustering algorithm.

5.4.1. γ-ray Database

As mentioned in Section 5.2.2, up to this point only γ rays with an energy $E_\gamma = 661.7\,\text{keV}$ can be correctly processed. However, to process any kind of γ-ray energy, incident or after being scattered, a fine grid of energies has to be preprocessed. This could be achievable by using common calibration sources like ^{137}Cs, ^{60}Co and ^{152}Eu. Between the measurable γ-ray energies, an interpolation of γ-ray scattering behavior is applicable. Since the Klein-Nishina cross section does not vary strongly in the range of $\sim 100\,\text{keV}$ (see Fig. 3.6), a cross-section weighted interpolation should yield good results.

5.4.2. Geometrical Clustering

Many experiments with relativistic ion beams suffer from very high multiplicities of incident γ rays per implantation event. Since all possible permutations of interaction points have to be processed, a general γ-ray tracking algorithm roughly runs with a time complexity $\mathcal{O}(nN!)$, where n is the amount of measured events and N the amount of interactions. Applying a geometrical clustering algorithm, the complexity can be reduced drastically. Such clustering algorithms search for closely lying interaction points and form clusters out of them. This is physically justified if the respective clusters are far away from each other since it is very unlikely that a single γ ray travels over the distance of a few ten centimeters. Applying such an algorithm, the computational time can be roughly reduced to $\mathcal{O}(n\sqrt{N}!)$ – assuming that the amount of clusters K is related to the amount of interaction points via $K \approx \sqrt{N}$. For more details on clustering algorithms, see Section 3.4.4 and Appendix A.

6. $\gamma\gamma/\gamma$ Experiments with AGATA

Thanks to AGATA's high position resolution in addition to its γ-ray tracking capabilities, it is very selective regarding different types of incident γ-ray energies occurring in a typical γ-spectroscopy experiment. However, a scenario in which AGATA is potentially pushed to its achievable discrimination limits are, e.g., experiments of the $\gamma\gamma/\gamma$ decay (see Sec. 2.4). The high achievable position resolution of AGATA should potentially allow for the measurement of angular correlations between the γ-ray pairs emitted in the $\gamma\gamma$ decay, giving rise to novel nuclear structure properties such as generalized polarizabilities (see Sec. 2.4). However, due to the comparatively low time resolution of HPGe detectors, compared to scintillation detectors used in the first observation of the $\gamma\gamma/\gamma$ decay [Wal15], a discrimination between γ and $\gamma\gamma$ decay events has to fully rely on γ-ray tracking methods. Whether such an approach is feasible, is discussed in the following using the already measured $\gamma\gamma/\gamma$ decay of ^{137}Ba as an example case. For this analysis, OFT (see Sec. 3.4.4) as well as the novel γ-ray tracking algorithm `ExpTrack` (see Chap. 5) are used.

6.1. Experimental Method

As already stated, the discrimination between γ and $\gamma\gamma$ decay events cannot rely on the time difference between the measured interaction points in AGATA. Hence, the potential analysis of such experiments has to fall back to γ-ray tracking techniques. As shown in Figure 6.1, the typical discrimination scenario is the following – assuming that only two interaction points have been measured for now, which is generally not the only possible case. Given the measured deposited energies $E_{\mathrm{dep},1}$ at $\vec{x}_1$ and $E_{\mathrm{dep},2}$ at $\vec{x}_2$, there are two possible scenarios:

- One γ-decay photon with incident energy E_γ that Compton-scattered at $\vec{x}_1$ and was photo-absorbed at $\vec{x}_2$ (Fig. 6.1, blue path).

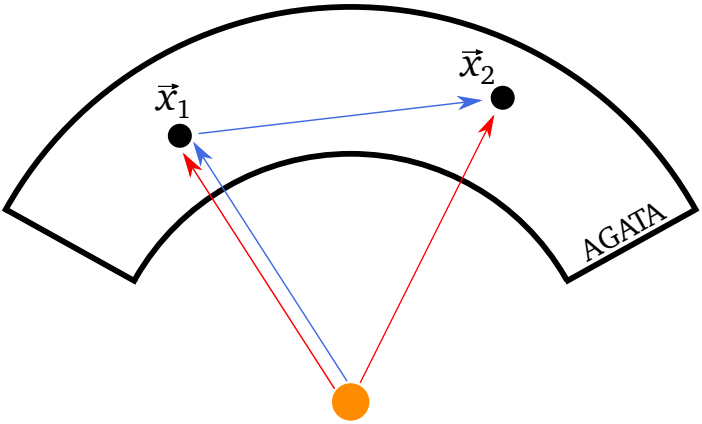

Figure 6.1.: Discrimination scenario in AGATA between the potential path of a single γ ray from the γ decay (blue) and two γ rays from the $\gamma\gamma$ decay (red). The source is depicted as an orange dot.

- Two $\gamma\gamma$-decay photons with respective incident energies $\omega_1 = E_{\mathrm{dep},1}$ and $\omega_2 = E_{\mathrm{dep},2}$ both being photo-absorbed at $\vec{x}_1$ and $\vec{x}_2$ (Fig. 6.1, red paths).

For each event, those two scenarios now have to be compared from a γ-ray tracking point-of-view. Since the Compton-scattering dynamics of photons in matter are known (see Sec. 3.4.3), a *cone of acceptance* is formed given the incident photon energy E_γ and the deposited energy $E_{\mathrm{dep},1}$ (see Fig. 6.2). Its opening angle is given by the Compton-scattering angle based on the incident energy E_γ and the deposited energy $E_{\mathrm{dep},1}$ (see Eq. (3.2)). Given the metrological uncertainties in energy and position resolution, the cone of acceptance is widened by the respective uncertainty $\Delta\theta$ (see Fig. 6.2). If the second interaction at $\vec{x}_2$ lies inside said cone, it is very likely that a single photon has deposited the measured energies. If this is not the case, however, it is not likely that a single photon is responsible for the measured data.

However, in addition to the possibility that two $\gamma\gamma$ decay photons are the cause of the measured data, there are (at least) three further causes for such events.

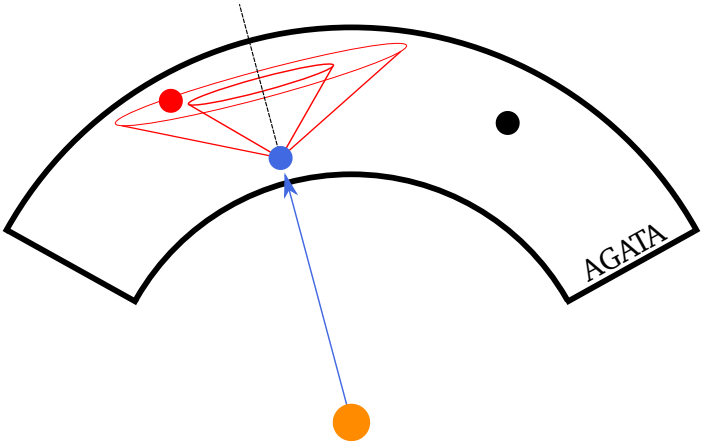

Figure 6.2.: The red measured interaction point lies within the cone of acceptance defined by the incident γ-ray energy and the deposited energy at the blue interaction point. The black dot lies outside the cone, rendering a Compton scattering from the blue towards the black dot very unlikely.

6.1.1. $\gamma\gamma - \gamma$ Discrimination Restraints

Since the $\gamma\gamma$ decay is strongly suppressed compared to the γ decay, the biggest challenge for its potential measurement with AGATA is background reduction. In total, there are three different kinds of background – natural background radiation, random coincident γ-decay events and falsely tracked γ-decay events.

Natural Background

As per usual, natural background radiation is present during nuclear physics experiments. To generate events that mimic a $\gamma\gamma$ decay, the following possibilities arise (scenarios sketched in Fig. 6.3):

1. A single background photon, e.g., from a decay of ^{40}K, interacts twice and exits the detector after the second scattering.

2. Two background photons interact both once and exit the detector.

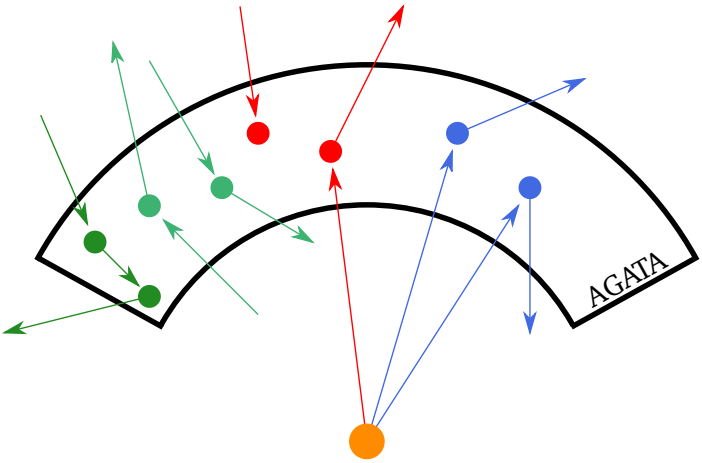

Figure 6.3.: Examples for possible scenarios mimicking the $\gamma\gamma$ decay. Cases 1 and 2 in different shades of green, case 3 in red and random coincidences of γ-decay events in blue.

3. A γ-decay photon and a background photon both interact and exit the detector.

In addition, any combination of these scenarios is also possible. The only physical condition is the total deposited energy of all measured interaction points – $E_{\mathrm{dep},1} + E_{\mathrm{dep},2} = E_\gamma$, where E_γ is the energy of the γ-decay transition. Depending on the scenario, these events are quite unlikely, especially given the mentioned condition on the deposited energy. However, since the $\gamma\gamma$ decay itself is extremely rare (see Sec. 2.4), such scenarios may very well spoil the low statistics achievable of the $\gamma\gamma$ decay.

Random Coincidences

In addition to background induced false $\gamma\gamma$-decay events, it is also possible that two γ-decay photons from two simultaneous γ decays both enter the detector, deposit $E_{\mathrm{dep},1} + E_{\mathrm{dep},2} = E_\gamma$ and exit the detector afterwards (see Fig. 6.3). The probability of the emission of two γ decay photons within a time window ΔT can

be approximated via a Poisson distribution [Kno00, Leo94]

$$P_{\gamma,\gamma} = \frac{(\Delta T \cdot A)^2}{2} e^{-\Delta T \cdot A}, \tag{6.1}$$

where A is the activity of the used source. Comparing this to the γ decay

$$\frac{P_{\gamma,\gamma}}{P_\gamma} = \frac{\Delta T \cdot A}{2}, \qquad \frac{P_{\gamma\gamma}}{P_\gamma} = \frac{\Gamma_{\gamma\gamma}}{\Gamma_\gamma}, \tag{6.2}$$

it can be seen that random coincident γ events can be reduced by simply choosing a relatively low activity which is still high enough to allow for a measurement of the $\gamma\gamma$ decay in a sensible time.

Falsely Tracked γ-decay Events

The biggest problem for γ-decay events is the tracking performance of AGATA itself. As mentioned in Chapter 5, one of the main problems for tracking algorithms is the merging of interaction points by the PSA. Although this happens in only 10 % of the cases – at least in the simulated scenario – a background of many orders of magnitude above the $\gamma\gamma$ decay arises. This ultimately yields a very challenging analysis of such experiments.

In the following, a first feasibility study of $\gamma\gamma$ experiments with AGATA based on simulations is presented.

6.2. γ-ray Tracking Analysis of $\gamma\gamma/\gamma$-decay Experiments

Although there are many possible candidates for nuclei that undergo a potential $\gamma\gamma/\gamma$ decay, the only experimental observation has been achieved for the nucleus ^{137}Ba via its $11/2^- \rightarrow 3/2^+$ transition with the γ-ray energy of $E_\gamma = 661.7\,\text{keV}$. Since the $\gamma\gamma$ decay is a strongly suppressed process, no experimental data with AGATA can be used to quantify the achievable performance for such an exotic experiment. Hence, only simulations can be used.

6.2.1. Simulations

All simulations performed for this analysis are based on *Geant4* [Ago03, All06, All16] simulations with the AGATA simulation code [Far10]. The used configuration for AGATA is based on the GANIL setup in 2017 – as described in Section 5.2.2.

γ Events

Single γ-decay events are simulated via 661.7 keV γ rays being emitted isotropically in all directions since there is no predominant orientation of the emitting nuclei.

$\gamma\gamma$ Events

The first decision that has to be made by the simulation is the decay behavior, approximately described by $E3M1$ or $M2E2$ (see Sec. 2.4). As stated in Section 2.4, Table 2.1, the respective decay widths $\Gamma_{\gamma\gamma,E3M1}$ and $\Gamma_{\gamma\gamma,M2E2}$ are approximately given by the $1h^{-}_{11/2} \rightarrow 2d^{+}_{5/2} \rightarrow 2d^{+}_{3/2}$ and $1h^{-}_{11/2} \rightarrow 1g^{+}_{7/2} \rightarrow 2d^{+}_{3/2}$ transitions. Hence, the relative probabilities of the $E3M1$ and $M2E2$ transitions are given by

$$P_{E3M1} = \frac{\Gamma_{\gamma\gamma,E3M1}}{\Gamma_{\gamma\gamma,E3M1} + \Gamma_{\gamma\gamma,M2E2}} = \frac{0.78 \times 10^{-6}}{(0.78 + 1.28) \times 10^{-6}} = 0.38\,, \tag{6.3}$$

$$P_{M2E2} = 1 - P_{E3M1} = 0.62\,. \tag{6.4}$$

Via a random variable $X \sim \mathcal{U}(0,1)$, the decay behavior is set to be $E3M1$, if $X \leq 0.38$ and $M2E2$, if $X > 0.38$. Since the energy distribution of 661.7 keV on both $\gamma\gamma$-decay photons is governed by the respective decay behavior (see Sec. 2.4), the respective probability densities $\rho_{E\lambda_1 M\lambda_2}(\omega_1)$ (see Fig. 2.4) are used to generate the two photon energies ω_1 and $\omega_2 = E_\gamma - \omega_1$ via the approach mentioned in Section 2.5.2. The angles of emission are generated in a similar manner. The first γ ray with energy ω_1 is emitted isotropically. Via the decay behavior $E\lambda_1 M\lambda_2$, the respective probability densities $\rho_{E\lambda_1 M\lambda_2}(\alpha)$ are used to obtain the emission angle α between the two γ rays via $\alpha \sim P_{E\lambda_1 M\lambda_2}(0,\pi)$ with $P_{E\lambda_1 M\lambda_2}(0,\pi)$ as the CDF of $\rho_{E\lambda_1 M\lambda_2}(\alpha)$ (see Sec. 2.5.2). The second spatial angle φ between both γ rays (see Fig. 6.4) is chosen via $\varphi \sim \mathcal{U}(0, 2\pi)$.

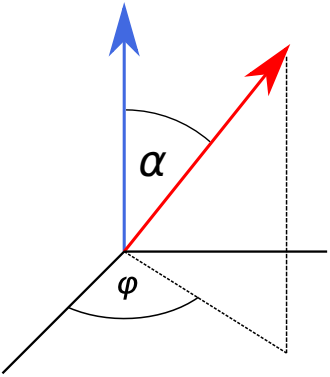

Figure 6.4.: Angles between simulated $\gamma\gamma$ events. The first γ ray is emitted randomly (blue arrow). The second γ ray is emitted based on the emission behavior of the $E3M1$ or $M2E2$ transition mentioned in Section 2.4.

General Preprocessing

To incorporate PSA-induced issues such as interaction point merging, both γ and $\gamma\gamma$ events are preprocessed before they are analyzed further. To account for the intrinsic position and energy resolution, the simulated deposited energies $E_{\mathrm{dep,true}}$ are varied via

$$E_{\mathrm{dep}} \sim \mathcal{N}(E_{\mathrm{dep,true}}, \sigma(E_{\mathrm{dep,true}})), \tag{6.5}$$

where E_{dep} is randomly chosen from the normal distribution $\mathcal{N}(\mu, \sigma)$ with mean $\mu = E_{\mathrm{dep,true}}$ and standard deviation

$$\sigma(E) = \frac{0.002}{2.355} \cdot E, \tag{6.6}$$

corresponding to an intrinsic energy resolution of 0.2 % FWHM. The interaction points are varied in a similar manner. For each simulated interaction point $\vec{x}_{\mathrm{true}}$, a randomization via

$$\vec{x} \sim \mathcal{N}_{\mathrm{3D}}(\vec{x}_{\mathrm{true}}, \Sigma_x), \tag{6.7}$$

with a multivariate normal distribution $\mathcal{N}_{3D}$ with mean $\vec{x}_{true}$ and covariance matrix $\Sigma = \mathbb{1} \cdot \sigma_x^2$ and the PSA-induced position resolution of $\sigma_x = 2.12\,\text{mm}$ (5 mm FWHM) is applied. Modeling the position resolution via $\mathcal{N}_{3D}$ is only a rough approximation. The uncertainty generally depends on many factors such as the special properties of the hit crystal – since they are not exactly the same – as well as the actual position inside the crystal. To model the interaction point merging, a probability density

$$\rho(\vec{x}_1, \vec{x}_2, \sigma_x) = \frac{1}{\sqrt{2\pi}\sigma_x} \exp\left(-\frac{||\vec{x}_1 - \vec{x}_2||^2}{2\sigma_x^2}\right), \tag{6.8}$$

is used. Here, $\vec{x}_1$ and $\vec{x}_2$ are the potential candidates for an interaction point merge. To decide whether an interaction point merge occurred, a random variable

$$X \sim \mathcal{U}\left(0, \frac{1}{\sqrt{2\pi}\sigma_x}\right), \tag{6.9}$$

is obtained. An interaction point merge is performed, if

$$X \leq \rho(\vec{x}_1, \vec{x}_2, \sigma_x). \tag{6.10}$$

Hence, an interaction point merge is very likely for closely lying points and gets decreasingly likely with increasing distance $||\vec{x}_1 - \vec{x}_2||$ between the interaction points. The position of the merged point is calculated via

$$\vec{\mu} = \frac{E_{dep,1}\vec{x}_1 + E_{dep,2}\vec{x}_2}{E_{dep,1} + E_{dep,2}}, \tag{6.11}$$

where $\vec{\mu}$ is the merged interaction point of $\vec{x}_1$ and $\vec{x}_2$ with energy deposition $E_{dep,\mu} = E_{dep,1} + E_{dep,2}$. The interaction point merging procedure is performed on every simulated interaction point. Multiple merges with $\vec{\mu}$ taking the role of $\vec{x}_1$ in the described process is possible.

6.2.2. Method

For both γ and $\gamma\gamma$ events, the same analysis methods apply since no discrimination can be done beforehand. For each event, γ or $\gamma\gamma$, only events with two interaction points in total (after interaction point merging) are analyzed. These events

are then passed to a γ-ray tracking algorithm. Given the predefined acceptance windows of the algorithm, only events which were identified as two photons with incident photon energies $E_{\mathrm{dep},1}$ and $E_{\mathrm{dep},2}$ are analyzed further. Figure 6.1 shows the general discrimination task that has to be performed by the γ-ray tracking algorithm. In the case of $\gamma\gamma$ events, only a small amount of events should be incorrectly identified as a single incident photon that interacted twice. However, in the case of γ events, the amount of photons that were incorrectly identified as two incident photons should be as small as possible. Additionally, since an identification of the $\gamma\gamma/\gamma$ is only possible for fully-absorbed events, meaning

$$E_{\mathrm{dep},1} + E_{\mathrm{dep},2} = (661.7 \pm 2)\,\mathrm{keV}\,, \tag{6.12}$$

only such events are used in the analysis.

Both OFT (see Sec. 3.4.4) and `ExpTrack` (see Chap. 5) have been used as γ-ray tracking algorithms. OFT's parameters have been set to *sigma_theta* $= 0.8$, *minprobsing* $= 0.02$ and *minprobtrack* $= 0.05$. Although the highest discrimination between γ and $\gamma\gamma$ events as stated in [Bru18] would stem from *minprobsing* $= 0.4$ and *minprobtrack* $= 0.15$, these values were not used since the large value of the parameter *minprobsing* is causing a cutoff of energies at $E_{\mathrm{dep}_>} \lesssim 390\,\mathrm{keV}$. In addition, `ExpTrack`'s parameter P_{max} (see Sec. 5.2.3) is set to 0.65.

6.2.3. Results

In total, 7.2×10^9 γ events and 3.6×10^9 $\gamma\gamma$ events[1] were simulated. As shown in Figure 6.5, the resulting spectra for the total deposited energies for the γ and the $\gamma\gamma$ events are visible for events with two interaction points. In contrast to the single γ decay events, there is no Compton edge present in $\gamma\gamma$ events since no 661.7 keV photons with their Compton edge at 477 keV are present. A comparatively small amount of fully absorbed $\gamma\gamma$ events, compared to γ events, is present due to the small probability of both photons being emitted in the direction of AGATA. In addition, Figure 6.6 shows the potential energy $\omega = E_{\mathrm{dep},1}$ (see Sec. 2.4) for both decay types which is just the first deposited energy in the list of $\{E_{\mathrm{dep},1}, E_{\mathrm{dep},2}\}$ – representing the first "measured" interaction for γ events as well as the energy of the first γ ray for $\gamma\gamma$ events. For $\gamma\gamma$ events, the expected mixture

[1] Emission of two γ rays per event

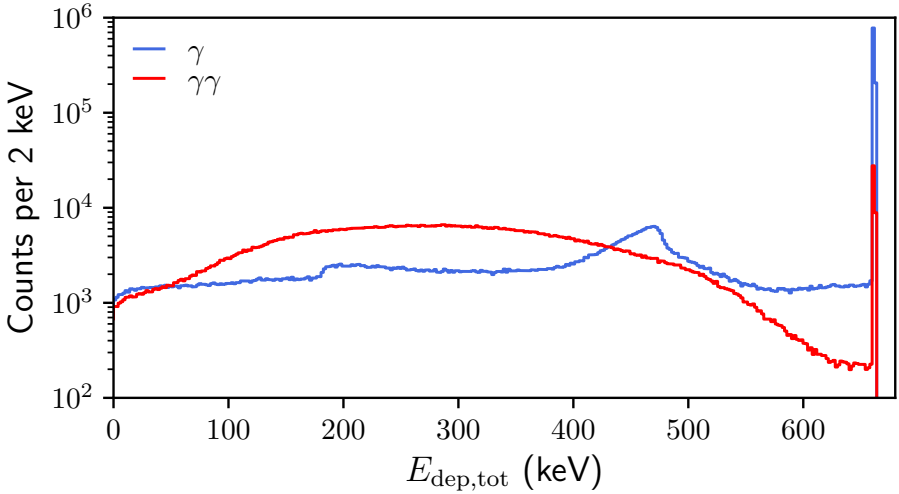

Figure 6.5.: Total deposited energies from γ decay events (blue) and $\gamma\gamma$ decay events (red). For the γ decay, 1.2×10^7 events were used to create the respective spectrum. For $\gamma\gamma$ events, 6×10^7 events were used.

of $E3M1$ and $M2E2$ (see Sec. 2.4) is present. For γ events, the majority of $E_{\mathrm{dep}_>}$ is located around the Compton edge at 477 keV (see also Sec. 5.1).

For both utilized γ-ray tracking algorithms, the spectra for $E_{\mathrm{dep}_>}$ for all events identified as $\gamma\gamma$ events are shown in Figure 6.7. For OFT, there are a few discrepancies between the ingoing events (see Fig. 6.6) and the events identified as $\gamma\gamma$ events. A small dip around the Compton edge for true $\gamma\gamma$ events is present since these events might resemble γ event photons that Compton-scattered in an angle of 180° (see also Sec. 5.3). In contrast, γ events identified as $\gamma\gamma$ events by `ExpTrack` show a similar distribution as depicted in Figure 5.8. In contrast, $\gamma\gamma$ events identified as $\gamma\gamma$ events by `ExpTrack` show a completely altered spectrum. It can be roughly understood as a mapping of the algorithm's response to tracking γ events as $\gamma\gamma$ events (see Fig. 5.8) onto the ingoing spectrum of $\gamma\gamma$ events (see Fig. 6.6). Since $\gamma\gamma$ events are not related by any Compton scattering, the likelihood for $\gamma\gamma$ physically resembling γ events is relatively large – at least, if compared

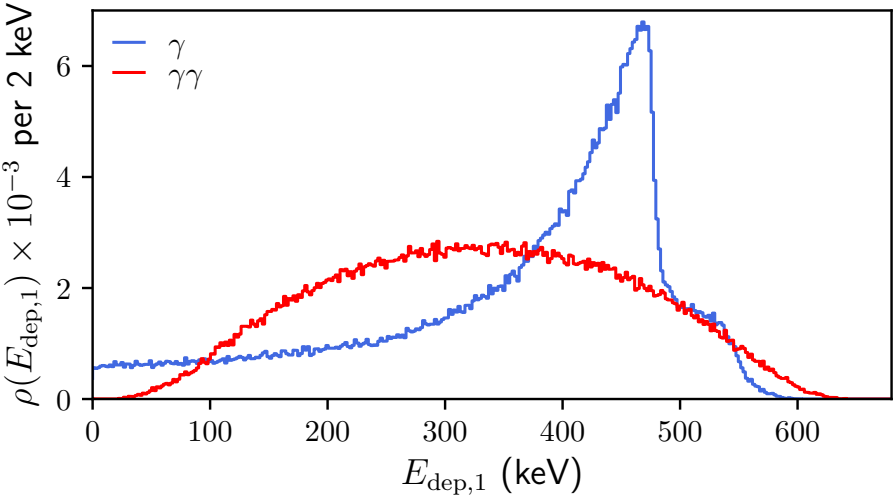

Figure 6.6.: Probability densities for the energy $E_{\mathrm{dep},1}$ of the first "measured" interaction point for simulated γ and $\gamma\gamma$ events that interacted only twice while depositing the full (661.7 ± 2) keV. For γ events, the Compton edge as well as larger values due to interaction point merging (see Chap. 5) are present. For $\gamma\gamma$ events, the spectrum mimics the overlap of possible $E3M1 - M2E2$ behavior.

to γ events with a different incident photon energy. Hence, a mapping of the tracking behavior onto the ingoing spectrum of $\gamma\gamma$ events is likely. The identification-efficiencies for identifying γ events as $\gamma\gamma$ events $\epsilon_{\gamma\to\gamma\gamma}$, $\gamma\gamma$ events as $\gamma\gamma$ events $\epsilon_{\gamma\gamma\to\gamma\gamma}$ as well as their ratio $\eta_{\gamma,\gamma\gamma} = \epsilon_{\gamma\to\gamma\gamma}/\epsilon_{\gamma\gamma\to\gamma\gamma}$ are given in Table 6.1. In addition, the respective reconstruction performances of OFT and `ExpTrack` given by the ratios $r_{\gamma\to\gamma\gamma} = N_{\gamma\to\gamma\gamma}/N_{\gamma,\mathrm{abs.}}$ and $r_{\gamma\gamma\to\gamma\gamma} = N_{\gamma\gamma\to\gamma\gamma}/N_{\gamma\gamma,\mathrm{abs.}}$ with the amount of falsely identified γ events $N_{\gamma\to\gamma\gamma}$ and correctly identified $\gamma\gamma$ events $N_{\gamma\gamma\to\gamma\gamma}$ compared to the respective events $N_{\gamma,\mathrm{abs.}}$ and $N_{\gamma\gamma,\mathrm{abs.}}$ that were photo-absorbed are also shown in Table 6.1. In total, OFT identifies γ and $\gamma\gamma$ events better than `ExpTrack`. Despite the fact that $\eta_{\gamma,\gamma\gamma}$ is around one, at least for OFT, the physical suppression of $\gamma\gamma$ events of 2.05×10^{-6} in the ^{137}Ba case (see Sec. 2.4) is too

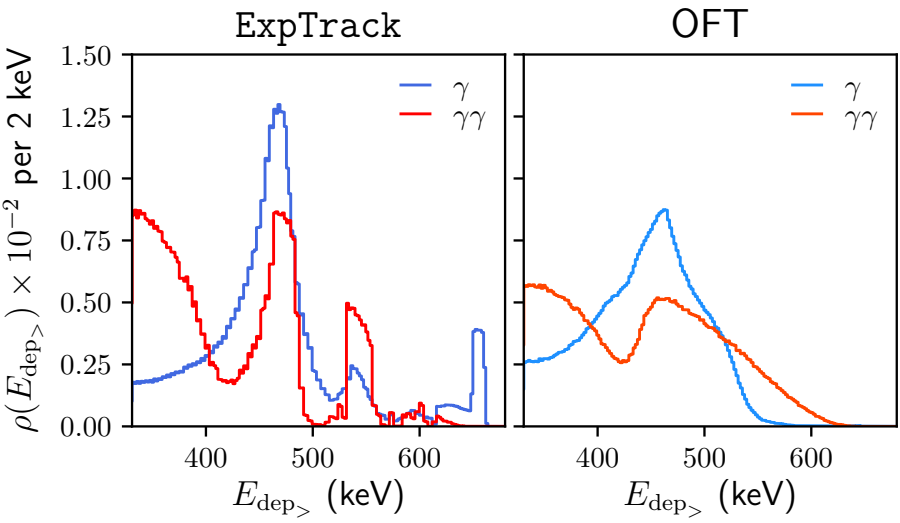

Figure 6.7.: $E_{\mathrm{dep}_>}$ for γ and $\gamma\gamma$ events for $N = 2$ and $E_{\mathrm{dep,tot}} = (661.7 \pm 2)\,\mathrm{keV}$ for events that were identified as two incident γ rays via `ExpTrack` (left) and OFT (right). Compared to Figure 6.6 the energy distribution between the two potential γ rays is severely altered. A detailed description of the emerging structures in the respective spectra for γ and $\gamma\gamma$ events is given in the text.

large to identify $\gamma\gamma$ events using only γ-ray tracking. Hence, additional measures to suppress falsely identified γ events have to be taken.

6.2.4. Discussion

For all events that are identified as $\gamma\gamma$ events, an additional identification measure is taken. In the case of $\gamma\gamma$ events, the distance between the two interaction points is not governed by any physical relation except the emission angle α between the two γ rays (see Sec. 6.2.1). Hence, any distance realizable in the setup of AGATA is possible. In the case of the γ decay, the distance is governed by the mean free

Table 6.1.: Achieved reconstruction efficiencies of γ and $\gamma\gamma$ events by `ExpTrack` and OFT. Ratios of events reconstructed as $\gamma\gamma$ events to absorbed events $r_{\gamma\to\gamma\gamma}$ for γ events and $r_{\gamma\gamma\to\gamma\gamma}$, respective reconstruction efficiencies $\epsilon_{\gamma\to\gamma\gamma}$ and $\epsilon_{\gamma\gamma\to\gamma\gamma}$ as well as their ratio $\eta_{\gamma,\gamma\gamma}$.

	$r_{\gamma\to\gamma\gamma}$ (%)	$r_{\gamma\gamma\to\gamma\gamma}$ (%)	$\epsilon_{\gamma\to\gamma\gamma}$ (10^{-4})	$\epsilon_{\gamma\gamma\to\gamma\gamma}$ (10^{-4})	$\eta_{\gamma,\gamma\gamma}$
OFT	1.2	70.8	2.1	2.4	0.9
`ExpTrack`	13.9	45.2	24.9	1.5	16.4

path λ of the scattered photon after its first interaction (see Sec. 3.4.2). Hence, large distances $d \gg \lambda$ are very unlikely. Due to AGATA's geometrical shape, it is possible that γ rays travel through air between the interaction points. This alters the possible travel distances severely. Hence, the distance through air between the interaction points has to be subtracted via

$$d = ||\vec{x}_1 - \vec{x}_2|| - d_{\text{air}}(\vec{x}_1, \vec{x}_2), \tag{6.13}$$

where $d_{\text{air}}(\vec{x}_1, \vec{x}_2)$ is the distance through air between $\vec{x}_1$ and $\vec{x}_2$. The method of calculating d_{air} is shown in Appendix D. Via utilization of the travel distance d, the amount of incorrectly categorized γ events can be further reduced.

The distances d between the interaction points are shown in Figure 6.8. For OFT, the distance between interaction points in γ events drops exponentially, as expected. At low distances d, a sudden jump in the probability density is present. This is not caused by any physical behavior of the photons, but most likely by some internal thresholds set by OFT, e.g., *minprobsing*, which indirectly handles the accepted distance between interaction points stemming from two incident γ rays (see Sec. 3.4.4). It is present in both γ and $\gamma\gamma$ events. For $\gamma\gamma$ events, small distances are unlikely to be registered as two photons in addition to a relatively small probability for two photons being emitted with a very small angle α. Hence, the maximum of the $\gamma\gamma$ distribution is reached at higher values of d. For $d \gtrsim 150\,\text{mm}$, the distribution also decreases since large distances are also very unlikely due to AGATA's limited geometry. `ExpTrack`'s spectra show a similar behavior without the sudden dip around $d \approx 40\,\text{mm}$. However, closely lying events are not suppressed by any threshold like *minprobsing* in OFT.

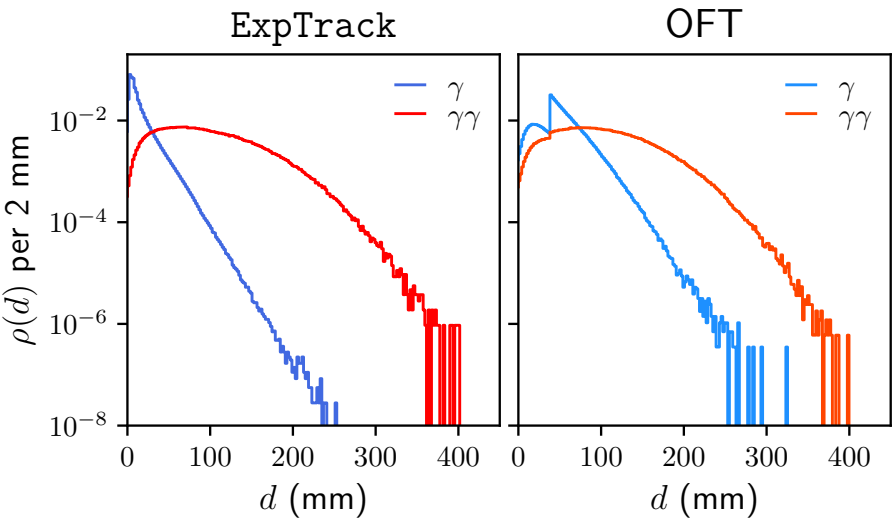

Figure 6.8.: Travel distances d calculated via Equation (6.13) of γ rays identified as $\gamma\gamma$ events with $E_{\text{dep,tot}} = (661.7 \pm 2)\,\text{keV}$ and $N = 2$ for `ExpTrack` (left) and OFT (right). The respective shapes are thoroughly discussed in the text.

To analyze the probability detecting $\gamma\gamma$-decay photons, the suppression of $\gamma\gamma$ to γ events of 2.05×10^{-6} in addition to the reconstruction efficiencies $\epsilon_{\gamma,\gamma\gamma\to\gamma\gamma}$ of γ and $\gamma\gamma$ events (see Tab. 6.1) are applied respectively. The resulting probabilities are

$$\varrho(d) = \rho(d)\epsilon_{\gamma,\gamma\gamma\to\gamma\gamma}P_{\gamma,\gamma\gamma}\,, \tag{6.14}$$

with $\rho(d)$ given in Figure 6.8 and the relative probabilities for the γ and $\gamma\gamma$ decay

$$P_\gamma = 1 - 2.05 \times 10^{-6} \approx 1 \quad \text{and} \quad P_{\gamma\gamma} = 2.05 \times 10^{-6}\,. \tag{6.15}$$

The resulting spectra for $\varrho(d)$ are shown in Figure 6.9. The distances d for γ events were phenomenologically extrapolated since the suppression at high values of d is

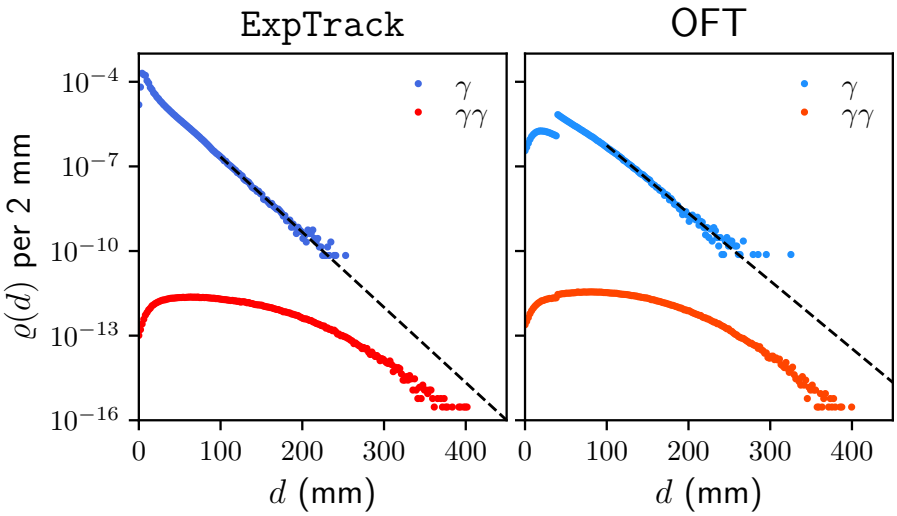

Figure 6.9.: Absolute process probabilities $\varrho(d)$ (see Eq. (6.14)) as a function of germanium travel distance d for events identified as $\gamma\gamma$ events for `ExpTrack` (left) and OFT (right). Due to excessively large needed simulation time, the distribution for γ-decay events is extrapolated via an exponential function. See text for details.

too high to simulate enough events in this range in a reasonable amount of time[2]. Although the suppression of γ events is large, the physical suppression factor of $\gamma\gamma$ to γ events is far too high to allow a successful measurement of the $\gamma\gamma/\gamma$ decay. It is not expected that an improvement in γ-ray tracking performance should be able to compensate a reduction of four orders of magnitude. This would correspond to an achieved tracking performance $r_{\gamma\to\gamma\gamma} \to 0, r_{\gamma\gamma\to\gamma\gamma} \to 1$, a perfect γ-ray tracking algorithm. Given the metrological restraints of AGATA – interaction point merging (see Chap. 5) as well as position- and energy-resolution independent of said interaction point merging – it is extremely unlikely that such a tracking algorithm

[2]It would roughly take 5.7 years to access the region of $d > 400$ mm with the used simulation tools and accessible processing power.

can ever be reached.

Of course, the probability of an assumption error in the applied extrapolation for the γ events (see Fig. 6.9) is non-negligible. If it is assumed that no falsely identified γ events remain for $d \geq 250\,\mathrm{mm}$, the total probability of such events is

$$P_{\gamma\gamma,d\geq 250\,\mathrm{mm}} = \int_{250\,\mathrm{mm}}^{\infty} \mathrm{d}d\, \varrho(d) \approx 2.37 \times 10^{-12}\ (\texttt{ExpTrack}), \approx 3.65 \times 10^{-12}\ (\mathrm{OFT}). \tag{6.16}$$

Under the assumption that a ^{137}Cs source with an activity of $A = 100\,\mathrm{kBq}$ is used, roughly twelve (OFT) or seven (ExpTrack) $\gamma\gamma$ events could be measured per year. Although only events that interacted twice were analyzed, it is not expected that events $N > 2$ should yield better results.

In general, an increased amount of interaction points introduces more possibilities for interaction-point merging – hindering the correct tracking process significantly. Hence, although more events for the $\gamma\gamma$ decay are accessible, the suppression factor of γ to $\gamma\gamma$ will most likely not increase enough to account for the general suppression of $\gamma\gamma$ events. Figure 6.11 shows the relative amount of measured interaction points N (after interaction point merging) for γ and $\gamma\gamma$ events as well as the modeled distance between the cluster centers of two assumed emitted γ rays for γ and $\gamma\gamma$ events. In first order approximation, the distance between the cluster centers $d_{\mathrm{Clust.}}$ can be interpreted as the mean distance between the interaction points of the emitted photons of the potential $\gamma\gamma$ decay (see Fig. 6.10). $d_{\mathrm{Clust.}}$ is calculated by inserting all measured interaction points per event into a fuzzy c-means algorithm (see [Bez81] and Appendix A) assuming that two geometrical clusters are present. The distance between the cluster centers is calculated and the distance through air is subtracted (see Fig. 6.11 (right)). Although small changes for γ events occur for $N > 2$, no significant change in the shape of the distribution is present. Similarly, the shape of the distance distribution for $\gamma\gamma$ also does not change.

Hence, it is not anticipated that the analysis for all $N \geq 2$ events will result in a successful measurement of the $\gamma\gamma/\gamma$ decay with AGATA given its current metrological abilities.

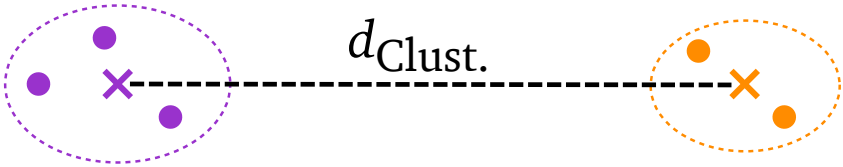

Figure 6.10.: Distance $d_{\text{Clust.}}$ between cluster centers calculated via a fuzzy c-means algorithm for events with $N > 2$. The two clusters corresponding to the two potential $\gamma\gamma$-decay photons are depicted in purple and orange, where the dots are the interaction points and the crosses the calculated cluster centers.

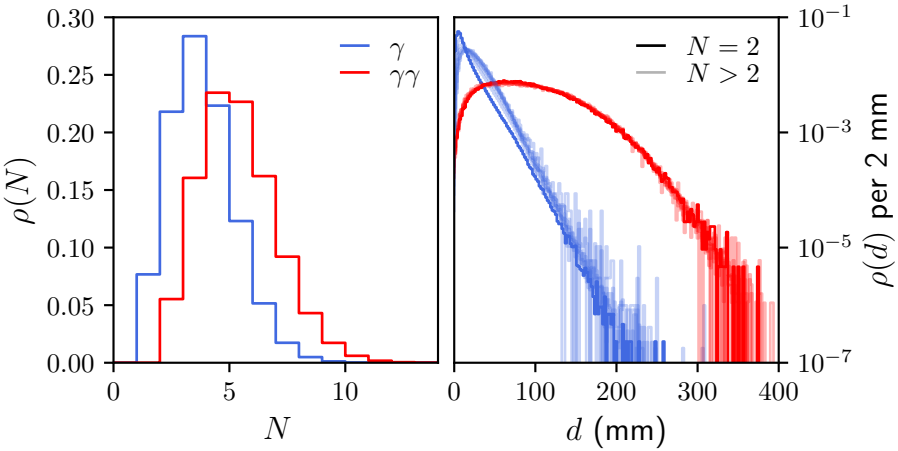

Figure 6.11.: *Left*: Probability density for amount of interactions N (after interaction point merging) for γ events (blue) and $\gamma\gamma$ events (red) that deposited (661.7 ± 2) keV in total. Roughly 95 % of the events of the $\gamma\gamma$ decay interact $N > 2$ times. For γ events, roughly 70 % interact more than twice. *Right*: Probability density for travel path (distance between cluster centers) through germanium for γ (blue) and $\gamma\gamma$ events (red) for up to ten interactions calculated via Equation (6.13).

7. Conclusion & Outlook

The presented thesis focused on two possible scenarios where γ-ray tracking and derived methods may yield an increase in performance or are the only possible way to analyze the measured data successfully.

The first scenario was the benchmark test of the *Coulex-multipolarimetry* designed for potential spin-flip experiments with relativistic ion beams. The novelty of said method is the ability to access information about $E2/M1$ multipole mixing ratios via comparison of measured γ-ray yields for different beam energies. The experiment designed for benchmarking this method via examination of the potential $\pi p_{3/2} \rightarrow \pi p_{1/2}$ spin-flip transition in the even-odd nucleus ^{85}Br was performed in 2014 during the PreSPEC campaign at GSI. In the setup of said experiment, two consecutive thick gold targets were used, mimicking a setup with a single target and two different incident beam energies. Although no beam excitation could be measured in the short beam time, an upper limit for the $M1$-transition strength of $B(M1,\downarrow) < 9.5\,\mu_N^2$ of the potential spin-flip transition has been estimated. In addition, estimates about the necessary beam time could be taken and the impact of the anticipated AGATA 1π setup has been estimated via *Geant4* simulations. Further performance improvements have been achieved via γ-ray tracking. A target identification method was presented, however, due to the limited amount of statistics in the target excitation peak, its feasibility could not be estimated with statistical significance. Conclusively, the identification of the potential $\pi p_{3/2} \rightarrow \pi p_{1/2}$ spin-flip transition in ^{85}Br with AGATA 1π via *Coulex-multipolarimetry* should be achievable in roughly 10 to 19 days of beam time in a radioactive ion beam facility, if the $M1$-transition strength of the potential spin-flip transition is in the range of $B(M1,\downarrow) \approx 3\,\mu_N^2$. If next-generation fragment separators such as the Super-FRS are available for a new experimental campaign, the necessary beam time can be further reduced. Assuming an increase in Peak-to-Background ratios of one order of magnitude caused by the utilization of novel fragment separators, the amount of necessary beam time is reduced by the same factor.

The second scenario in which γ-ray tracking is expected to strongly influence the experimental outcome are competitive double γ-decay experiments – suffering from suffocatingly large background radiation produced by the primary decay branch, the γ decay. Suppression of the desired $\gamma\gamma$ events is in the range of $\Gamma_{\gamma\gamma}/\Gamma_{\gamma} \approx 10^{-6}$. During the analysis process, a limiting factor of achievable tracking performance arose, the PSA-induced merging of interaction points. To account for this behavior, a novel type of γ-ray tracking algorithm was developed. Based on measured data of a ^{137}Cs source run as well as additional simulations, joint probability density distributions that emulate the Compton-scattering behavior of 661.7 keV γ rays in AGATA under any non-categorizable experimental influence such as PSA-induced interaction point merging have been calculated. A first version of such an experimental tracking algorithm, called `ExpTrack`, has been presented and compared to the go-to γ-ray tracking algorithm of the AGATA community – OFT. Since `ExpTrack` is still in a development stage, such a comparison can only indicate the expected performance of `ExpTrack`. Compared to OFT, `ExpTrack` performed well, especially at energies above the Compton edge where interaction point merging has its largest impact on achievable tracking performance.

To analyze, whether it is possible to measure the $\gamma\gamma/\gamma$ decay with AGATA, the $\gamma\gamma/\gamma$ decay scenario in ^{137}Ba was used – the only nucleus in which a $\gamma\gamma/\gamma$ decay has been measured so far. A feasibility study for potential $\gamma\gamma/\gamma$-decay measurements in ^{137}Ba with AGATA via *Geant4* simulations has been performed. In total, 7.2×10^9 γ-decay and 3.6×10^9 $\gamma\gamma$-decay events were simulated. The two γ-ray tracking approaches OFT and `ExpTrack` were utilized to identify γ rays that are labeled as two incident γ rays for a total amount of two interactions and a total energy deposition of (661.7 ± 2) keV. Due to the underlying mathematical structure of both tracking algorithms, the resulting energy spectra of the potential γ ray with the largest energy deposition are altered significantly. A further reduction of γ events has been achieved via consideration of the distance between the interaction points since they are related via the mean free path of the remaining γ ray for γ events, but unrelated for $\gamma\gamma$ events. However, due to the physical suppression of $\gamma\gamma$ to γ events, even travel distance considerations do not allow for a successful measurement of the $\gamma\gamma/\gamma$-decay given the current achievable position-resolution and γ-ray tracking performance.

Future improvements of AGATA might enhance the achieved discrimination rate

between γ and $\gamma\gamma$ events, e.g., via solving the interaction-point merging issue in its entirety. However, even if the $\gamma\gamma/\gamma$ decay would be potentially measurable thanks to γ-ray tracking methods, these methods still alter the energy and angle spectra. Since these spectra are the major source for information related to nuclear structure, an alteration is not advantageous. Whether or not a deconvolution of the "tracking response" is possible, potentially yielding information about the original spectra, is not known yet. It appears to be a lot less challenging to perform such a measurement via a travel-time based approach, such as performed in [Wal15]. Large arrays of $LaBr_3$(Ce) detectors appear to be far superior to HPGe arrays for successful measurements of the $\gamma\gamma/\gamma$ decay.

In general, γ-ray tracking is a very potent method to increase general selectivity in nuclear structure experiments. However, its performance strongly depends on the metrological abilities of the used detector array. Given the current problems with PSA, the clustering of interaction points at certain areas in the detectors as well as the mentioned interaction point merging, high precision experiments such as $\gamma\gamma/\gamma$ experiments are still out of reach. Much innovation in respect to position-resolving algorithms needs to be pursued in the future to push AGATA to its full potential. In addition, there are still many aspects of the behavior of γ rays in matter that need to be included into the framework of γ-ray tracking such as the influence of bound electrons in atomic shells as well as the potential reconstruction of incident γ-ray energy for Compton-escaped γ rays (see, e.g., [TG10, Nap16] and App. A).

A. Fuzzy Bayes-Tracking

Based on the work in [Nap16], an alternative approach to conventional γ-ray tracking methods (see Sec. 3.4.3) was developed and is briefly presented in the following.

A.1. General γ-ray Tracking Task

For a set amount N of measured interaction points at the respective positions $\vec{x}_i$ with deposited energy $E_{\mathrm{dep},i}$, a total probability

$$P\left(\left\{\vec{x}_1, E_{\mathrm{dep},1},\right\},\ldots,\left\{\vec{x}_N, E_{\mathrm{dep},N}\right\}\right) = \sum_{k=1}^{N} \underbrace{P\left(\left\{\vec{x}_1, E_{\mathrm{dep},1},\right\},\ldots,\left\{\vec{x}_N, E_{\mathrm{dep},N}\right\}|k\right)}_{\text{Likelihood function}} \underbrace{P(k)}_{\text{Prior}}, \tag{A.1}$$

for any potential amount of incident photons $k = 1,\ldots,N$ depositing any subset of the measured interaction points can be defined. The mentioned likelihood functions can also be formulated as the figure-of-merit used in OFT (see Sec. 3.4.4). The procedure of expanding probabilities in Equation (A.1) via

$$P(A) = \sum_i P(A, B_i) = \sum_i P(A|B_i)P(B_i) \tag{A.2}$$

is called *marginalization* [SS06] and

$$P(A|B_i) = \frac{P(A, B_i)}{P(B_i)}, \quad \text{with} \quad P(A, B_i) \equiv P(A \cap B_i), \tag{A.3}$$

is called *conditional probability* of event A given B_i. For more information about marginalization and conditional probabilities, the reader is referred to [SS06, EK17, Geo07].

The prior probability $P(k)$ of Equation (A.1) can be modeled via a Poisson distribution

$$P(k) = \frac{(\Delta T \cdot A)^k}{k!} \exp\left(-\Delta T \cdot A\right), \tag{A.4}$$

with the activity of the used source A and the used time window ΔT of AGATA limited by its time resolution. Hence, assuming that all measured γ rays are emitted from the source position, e.g., at the target position(s) in the reaction chamber, the amount of expected incident γ rays per event, defined by the time window ΔT, is included via $P(k)$. However, this assumption only holds if only a single transition per nucleus is observed. In the case of a cascade, where multiple transitions per decaying nucleus can occur consecutively, $P(k)$ has to be modified accordingly.

The γ-ray tracking task can be defined as identifying the most likely combination of subsets of $\left\{\vec{x}_1, E_{\mathrm{dep},1},\right\}, \ldots, \left\{\vec{x}_N, E_{\mathrm{dep},N}\right\}$ which directly translates to the most likely incident γ rays.

A.2. Calculation of Likelihood Functions

For a subset with k incident γ rays, the likelihood function in Equation (A.1) can be calculated via

$$\begin{aligned} &P\left(\left\{\vec{x}_1, E_{\mathrm{dep},1},\right\}, \ldots, \left\{\vec{x}_N, E_{\mathrm{dep},N}\right\} | k\right) \\ &= \sum_{\tau_i, \ldots, \tau_j} \prod_{n=1}^{k} P\left(\pi_n\left(\left\{\vec{x}_1, E_{\mathrm{dep},1},\right\}, \ldots, \left\{\vec{x}_N, E_{\mathrm{dep},N}\right\}\right) | E_n, n\right) P(n|E_n), \end{aligned} \tag{A.5}$$

where $\pi_n\left(\left\{\vec{x}_1, E_{\mathrm{dep},1},\right\}, \ldots, \left\{\vec{x}_N, E_{\mathrm{dep},N}\right\}\right)$ describes the permutation of a subset of all N interaction points with the sum over all permutations $\tau_i, \ldots, \tau_j$ that k incident γ rays can induce. An example for possible permutations for two incident γ rays is given in Figure A.1. The product $\prod_{n=1}^{k}$ is introduced to account for the coupled probabilities of the formed cluster. Hence, if, e.g., two incident γ rays are present, five interactions were measured and the first γ ray has interacted thrice, the second one has to have interacted twice. Hence, these events are coupled. However, the subsets of interaction points and corresponding energies for the k incident γ rays have to be disjoint. In addition, $P(n|E_n)$

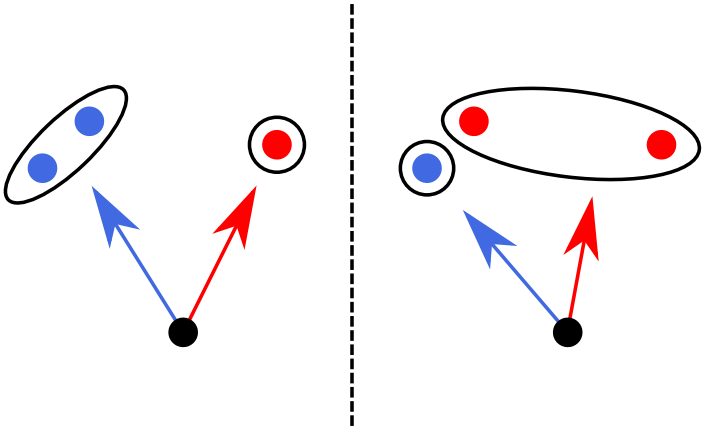

Figure A.1.: Two possible subsets of the three interaction points (colored dots) with the γ-ray source as black dot. The colors indicate the subset membership of the respective interaction points.

introduces the probability that a single γ ray interacted n times to deposit its full energy E_n with $E_n \leq \sum_{i=1}^{N} E_{\mathrm{dep},i}$. This prior probability can, e.g., be obtained via *Geant4* simulations. Figure A.2 depicts $P(n|E_n)$ for various incident γ ray energies as a function of n for AGATA in its AGATA Demonstrator configuration with five triple clusters. For each potential permutation, the probability $P\left(\pi_i\left(\left\{\vec{x}_1, E_{\mathrm{dep},1},\right\},\ldots,\left\{\vec{x}_N, E_{\mathrm{dep},N}\right\}\right)|E_n, n\right)$ can be expressed in terms of the physical γ ray travel path, the Compton scattering and photo-absorption via

$$P\left(\pi_i\left(\left\{\vec{x}_1, E_{\mathrm{dep},1},\right\},\ldots,\left\{\vec{x}_N, E_{\mathrm{dep},N}\right\}\right)|E_n, n\right) = \left[\prod_{i=1}^{n-1} P_{\mathrm{Comp},i} P_{\lambda,i}\right] \cdot P_{\mathrm{Photo}}\,, \tag{A.6}$$

where the Compton-scattering probability at the interaction point $\vec{x}_i$ is modeled via

$$P_{\mathrm{Comp},i} = \frac{\mathrm{d}\sigma(\theta_i, e_{i-1})}{\mathrm{d}\theta \sin\theta} \cdot \mathcal{G}(\vartheta_i, \theta_i) \tag{A.7}$$

with the single-differential Klein-Nishina cross section $\mathrm{d}\sigma(\theta_i, e_{i-1})/(\mathrm{d}\theta \sin\theta)$ (see Eq. (3.5)) and the comparison of geometrical and energy-based scattering angles

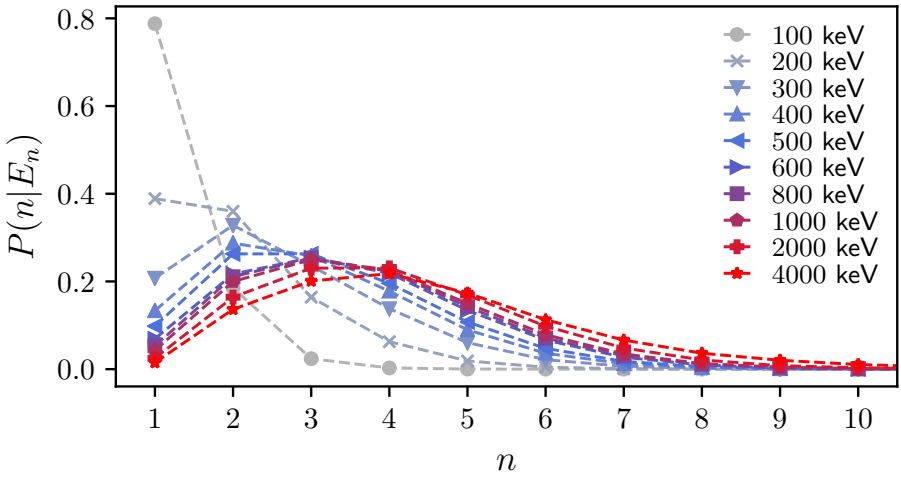

Figure A.2.: Prior probabilities $P(n|E_n)$ for various simulated incident γ-ray energies E_n for the AGATA Demonstrator setup. For small values of E_n, $n = 1$ is the most likely scenario. However, for larger values of E_n, more interactions become more likely. Interaction point merging as mentioned in Chapters 5 and 6 has not been investigated here.

ϑ_i and θ_i (see Sec. 3.4.3) via a Gaussian distribution $\mathcal{G}$ (see Eq. (3.12)). The energy of the γ ray after the i-th interaction is given by e_i with $e_0 = E_n$ as the incident energy of the γ ray. The probability for the γ ray traveling through air and germanium between $\vec{x}_{i-1}$ and $\vec{x}_i$ is given by

$$P_{\lambda,i} = \frac{1}{\lambda(e_{i-1})} \exp\left[-\frac{d(\vec{x}_{i-1}, \vec{x}_i)}{\lambda(e_{i-1})}\right], \tag{A.8}$$

with the mean free path $\lambda(e_{i-1})$ (see Sec. 3.4.2) and the pure distance through germanium

$$d(\vec{x}_{i-1}, \vec{x}_i) = ||\vec{x}_{i-1} - \vec{x}_i|| - d_{\text{air}}(\vec{x}_{i-1}, \vec{x}_i) \tag{A.9}$$

with the distance through air between the interaction points $d_{\text{air}}(\vec{x}_{i-1}, \vec{x}_i)$ (see App. D). The photo-absorption probability is given by

$$P_{\text{Photo}} = \sigma_{\text{Photo}}(e_n)\, P_{\lambda,n}\,, \tag{A.10}$$

extracted from the NIST XCOM dataset [Ber10].

To suppress γ rays that most-likely do not stem from the source position, such as background radiation, a threshold on the achieved probability can be used.

A.3. Geometrical Clustering

Since the amount of necessary computations directly scale with the amount of interaction points, i.e., $N!$, a geometrical clustering algorithm which preselects subsets of the full interaction point set significantly reduces the computation time. However, such geometrical clustering algorithms are also prone to failure since closely lying interaction points do not necessarily stem from a single γ ray. A possible approach are so-called *fuzzy c-means* algorithms [Bez81]. However, since the amount of incident photons is not known beforehand, additional measures have to be taken due to the fact that the amount of expected geometrical clusters is an input parameter of ordinary fuzzy c-means algorithms [Bez81]. A fuzzy-c-means algorithm which predicts the amount of clusters during the calculation of the cluster memberships is the *Robust learning fuzzy c means* (RLFCM) algorithm [YN17]. Starting from N clusters, where N is also the amount of total points, the amount of clusters is decreased during every iteration until the most likely amount of geometrical clusters is found. For more details on the RLFCM algorithm, the reader is referred to [YN17].

A.4. First Benchmarks

A first benchmark test of the *Fuzzy Bayes-Tracking* (FBT) has been performed using ^{60}Co and ^{152}Eu source data from the AGATA Demonstrator experiment 09.08 (see [Sta15a]). Only events with a total amount of interaction points of $1 \leq N \leq 5$ were used. The achieved performance has been compared to OFT (see Sec. 3.4.4). The

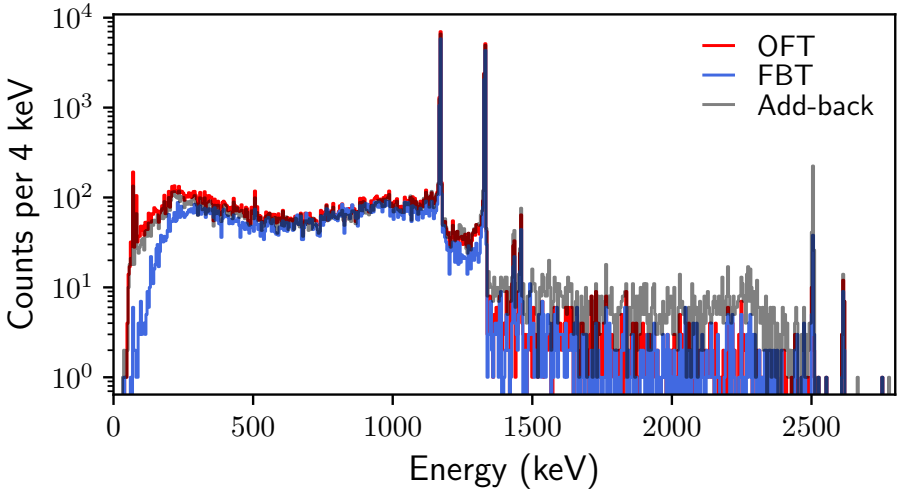

Figure A.3.: Spectrum of a ^{60}Co source measurement with the AGATA Demonstrator at LNL with a maximum of interaction points $N \leq 5$. The gray spectrum is achieved by simply using full add-back of all measured energies per event. The γ-ray tracked spectrum using OFT is depicted in red, using FBT in blue.

Table A.1.: Achieved peak-to-total ratios for ^{60}Co and ^{152}Eu source measurements with the AGATA Demonstrator using Fuzzy Bayes-Tracking (FBT), OFT or simple Add-back.

	FBT	OFT	Add-back
^{152}Eu	51.9 %	47.8 %	48.7 %
^{60}Co	43.9 %	40.4 %	39.9 %

achieved spectra, with and without γ-ray tracking, are shown in Figures A.3 and A.4. The resulting peak-to-total ratios are shown in Table A.1.

Although a higher peak-to-total ratio is achieved by FBT, its overall efficiency is

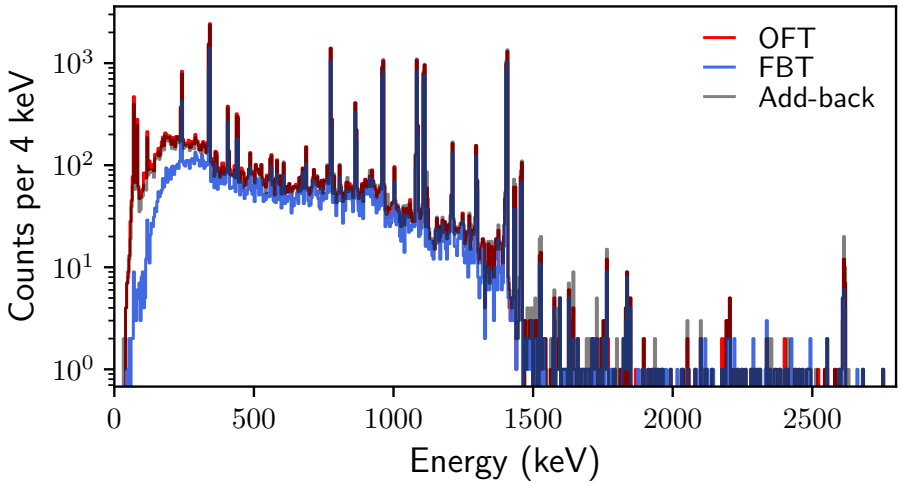

Figure A.4.: Spectrum of a ^{152}Eu source measurement with the AGATA Demonstrator at LNL with a maximum of interaction points $N \leq 5$. The used color code is the same as in Figure A.3.

roughly 17 % lower than for OFT's. Especially at low energies (see, e.g., Fig. A.4), almost all events are not accepted by FBT. This is caused by the set threshold in FBT in addition to an intrinsic measurement problem of AGATA. Events with low energies are most likely absorbed in AGATA's first section. In this region, however, interaction points tend to be reconstructed in areas further towards the back of AGATA. This fact is represented in Figure A.5, where the distance of travel in germanium divided by the energy-dependent mean free path of the γ ray as a function of the incident γ-ray energy is shown. In general, the travel distances should follow an exponentially decaying curve, given by Equation (A.8). However, at small γ-ray energies, larger values of d/λ are favored. For events with energies below 100 keV, roughly 92 % of all events show a $d/\lambda > 1$. In comparison, for events above 300 keV, only 47 % of all events are above said limit, ultimately resulting in a large suppression of low-energetic events in FBT.

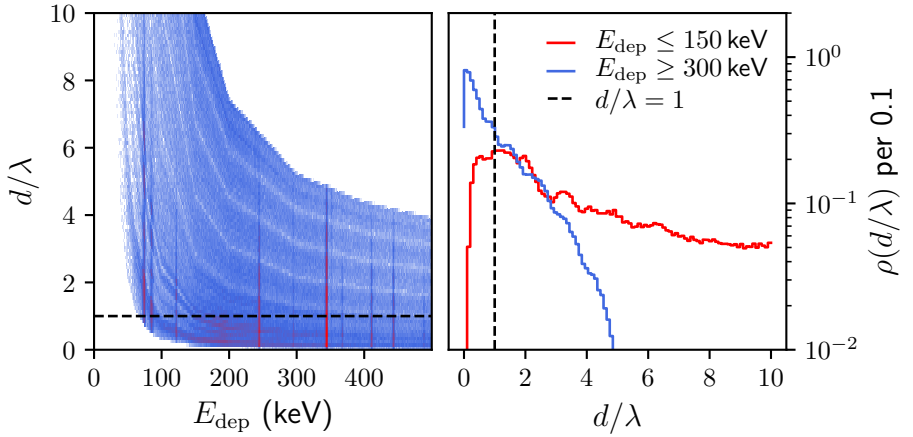

Figure A.5.: Travel distance through germanium divided by the energy-dependent mean free path λ as a function of deposited energy E_{dep} for events from a ^{152}Eu source measurement with $N = 1$ (left) and probability density $\rho(d/\lambda)$ for all events with $E_{\mathrm{dep}} \leq 150\,\mathrm{keV}$ (red) and $E_{\mathrm{dep}} \geq 300\,\mathrm{keV}$ (blue) on the right. The $d = \lambda$ limit is depicted as black dashed line. At low energies, a large deviation from the expected exponential decaying behavior is present. These events mostly interact in the first sector of AGATA, where the interaction point reconstruction tends to shift the original interaction point further towards the back of AGATA. Very large values of d/λ for the X-ray lines around 80 keV respond to X-rays entering AGATA from the side or the back.

Although the first benchmark test is convincing, additional test of FBT are necessary. Further improvement of the used clustering algorithms are necessary since even small changes in the used parameters strongly alter the achievable tracking performance.

A.5. Treatment of Compton-escape Events

In the scope of a mathematical rigorously defined γ-ray tracking algorithm, additional possible scenarios can be taken into account. As already shown in [Nap16] in the scope of the *Bayes-Tracking* algorithm, a general tracking algorithm based on Bayesian inference can also be used to include potentially escaped γ rays via reconstructing the most likely incident γ-ray energy. Similar to Equation (A.6), an additional escape probability $P_{\text{esc.}}$ consisting of a Compton-scattering probability at the last interaction point of the observed sequence coupled to an integral over all possible escape paths starting from said interaction point in all directions possible in the scope of the Compton scattering can be defined via

$$P_{\text{esc.}} = \int_0^{\pi} \mathrm{d}\theta \, P_{\text{Comp}}(e_{N-1}, \theta) \, \mathscr{G}(E_{\text{dep},N}, \mathscr{E}(e_{N-1}, \theta)) \times \int_0^{2\pi} \mathrm{d}\varphi \frac{1}{\lambda[e_{N-1} - \mathscr{E}(e_{N-1}, \theta)]} \exp\left(-\frac{d(\vec{x}_N, \theta, \phi)}{\lambda[e_{N-1} - \mathscr{E}(e_{N-1}, \theta)]}\right). \tag{A.11}$$

Here, $P_{\text{Comp}}(e_{N-1}, \theta)$ describes the probability of Compton scattering of a γ ray with energy e_{N-1} with an angle θ, $\mathscr{G}(E_{\text{dep},N}, \mathscr{E}(e_{N-1}, \theta))$ describes the probability of measuring the deposited energy $\mathscr{E}(e_{N-1}, \theta))$, calculated from Equation (3.2), as $E_{\text{dep},N}$ using a Gaussian distribution, $d(\vec{x}_N, \theta, \phi)$ is the distance until the remaining γ ray has exited AGATA given the direction of the γ ray before the Compton scattering and the scattering angles θ and ϕ and $\lambda[e_{N-1} - \mathscr{E}(e_{N-1}, \theta)]$ is the mean free path of the remaining γ ray with energy $e_{N-1} - \mathscr{E}(e_{N-1}, \theta)$. Since a Compton-escape scenario can only be possible if $E_\gamma > \sum_{i=1}^{N} E_{\text{dep},i}$, an additional marginalization over the incident γ-ray energy is performed where E_n in Equation (A.6) takes the role of an arbitrary incident γ ray energy (see [Nap16] for further details).

Although first results of this Bayes-Tracking algorithm were promising, additional measures are necessary for a successful approach to the Compton-escape scenario. Since the uncertainty modeling in position and energy is not based on a Gaussian uncertainty approach but a Monte-Carlo approach, calculating all possible γ-ray paths for a set of measured interaction points, high-dimensional integrals arise (see [Nap16] for details). The naive approach of sampling via uniformly-distributed random numbers during the integration process is not feasible for a

real experiment with billions of measured γ rays and integration dimensions

$$|D| = \underbrace{3N}_{\text{spatial dim.}} + \underbrace{1}_{E_n} + \underbrace{1}_{\theta} + \underbrace{1}_{\varphi}, \tag{A.12}$$

with N as the amount of interactions and additional dimensions for the integration over the possible incident γ ray energies E_n and the two scattering angles θ and φ for the Compton escape (see Eq. (A.11)). E.g., for three interaction points, a total of twelve integration dimensions need to be considered. In such high-dimensional regimes, a naive Monte-Carlo approach almost always samples random numbers outside of areas-of-interest of the integrand. Advanced integration methods such as Sparse-Grid methods [Hol11], using sparse grids of points in the multidimensional space for calculating the integral, or Markov-Chain Monte-Carlo methods [Mül12] that intelligently sample random numbers based on precalculated probability densities focusing on regions with the largest impact on the multidimensional integrals are mandatory. A successful treatment of these multidimensional integrals might yield a new type of γ-spectroscopy, where the most likely incident γ rays are inferred based on photo-absorbed and Compton-escaped data, ultimately resulting in a larger detection efficiency without the need of additional detector material.

B. DWEIKO Input Files

As mentioned in Section 4.4.1, DWEIKO is used to calculate the relativistic CoulEx cross sections in straight-line approximation for the ^{85}Br beam on the two ^{197}Au targets with respective beam energies of $E_{\text{kin}} = 300\,\text{MeV/u}$ in front of target 1 and $E_{\text{kin}} = 242$ MeV/u in front of target 2. For the given transition strengths of gold, $B(E2,\downarrow) = 33\,\text{W.u.}$ [Stu88] and for ^{85}Br, $B(M1,\downarrow) = 3.34\,\mu_N^2$ and $B(E2,\downarrow) = 1\,\text{W.u.}$, the corresponding matrix elements necessary for the DWEIKO calculations can be calculated via (see Eq. (2.38))

$$|\langle J_m||\mathscr{M}(\sigma\lambda)||J_n\rangle| = \sqrt{(2J_n+1)\,B(\sigma\lambda;J_n\rightarrow J_m)} \tag{B.1}$$

with $\sigma = E$ for electric and $\sigma = M$ for magnetic transitions and λ as the multipolarity. This yields

$$\left|\langle 7/2^+_{\text{g.s.}}||\mathscr{M}(E2)||3/2^+_1\rangle\right| = 134.01\,\text{e fm}^2$$

for gold and

$$\left|\langle 3/2^-_{\text{g.s.}}||\mathscr{M}(M1)||1/2^-_1\rangle\right| = 0.38\,\text{e fm}\,, \quad \left|\langle 3/2^-_{\text{g.s.}}||\mathscr{M}(E2)||1/2^-_1\rangle\right| = 6.66\,\text{e fm}^2$$

for bromine.

In the following, the input files for DWEIKO are shown for ^{85}Br in Listing B.1 and for ^{197}Au in Listing B.2, both for target 1 at a beam energy of 300 MeV/u. To change the incident beam energy, Einc in line 7 has to be modified accordingly. The states of interest J_n and J_m can be defined in lines 144 and 145[1]. The corresponding transition strengths are set in line 159. For more information on DWEIKO, see [Ber99]. The source code is available at [Ber].

[1] Lines can be added if more transitions are relevant

Listing B.1: DWEIKO input file ^{85}Br

```
# Input of program 'DWEIKO'
#
# charges and masses (AP,ZP,AT,ZT),
# bombarding energy per nucleon (Einc) in MeV.
#
# Ap       Zp      At       Zt       Einc[MeV/u]
  85       35      197      79       300
# (P.Napiralla: for T2 use Einc: 242)
# IW=0(1) for projectile (target) excitation.
# IOPM=1(0) for output (none) of optical
# model potentials.
# IOELAS=(0)[1]{2} for (no) [center of mass]
# {laboratory} elastic scattering cross section.
# IOINEL=(0)[1]{2} for (no) [center of mass]
# {laboratory} inelastic scattering cross section.
# IOGAM=(0)[1]{2} for (no) output
# [output of statistical tensors] {output of # gamma-ray
#  angular distributions}
#
# ============================================================
#
# IW=0(1) IOPM=0(1)  IOELAS=0(1)[2]  IOINEL=0(1)[2] IOGAM=0(1)[2]
  0       1          2               2              2
#
# ============================================================
# NB=number of impact parameter points (NB <= NBMAX).
# ACCUR=accuracy required for time integration at
# each impact parameter.
# BMIN=minimum impact parameter (enter 0 for default)
# IOB=1(0) prints (does not print) out
# impact parameter probabilities.
#
# ============================================================
#
#  NB          ACCUR         BMIN[fm]     IOB=1(0)
   200         0.001         0            0
#
# ============================================================
#
# OMP switch:
# IOPW=0  (no OMP)       IOPNUC=0  (no nuclear)
#      1  (Woods-Saxon)         1  (vibr. excitat.)
```

```
#      2 (read)
#      3 (t-rho-rho folding potential)
#      4 (M3Y folding potential)
# If optical potential is provided (IOPW=2), it should be
# stored in 'optw.in' in rows of
# R x Real[U(R)] x Imag[U(R)].
# The first line in 'optw.in' is the number
# of rows (maximum=NGRID).
#
# ============================================================
#
#      IOPW                          IOPNUC
       1                             0
#
# ============================================================
# If IOPW=1, enter V0_ws [VI_ws] = real part [imaginary]
# (>0, both) of Woods-Saxon.
# r0_ws [r0I_ws] = radius parameter (R_ws = r0 * (ap^1/3 + at^1/3).
#  d_ws [dI_ws]  = diffuseness.
# If IOPW is not equal to 1, place a '#' sign
# at the beginning of this line, or delete it.
#
# ============================================================
#
#   V0 [MeV]  r0[fm]   d[fm]    VI [MeV]   r0_I [fm] dI [fm]
    50.       1.2      0.8      58.        1.2       0.8
#
# ============================================================
#
# If IOPW=1 and Ap, or At, equal to one (proton),
# enter here spin-orbit part.
# If not, place a '#' sign at the beginning of this line,
# or delete it.
#  VS0 = depth parameter of the spin-orbit potential (>0).
#  r0_S = radius parameter.
#  dS = difuseness.
#  V_surf = depth parameter of the surface potentail (>0).
#  a_surf = difuseness.
#
# ============================================================
#
#   VS0 [MeV]    r0_S [fm]   dS [fm]   V_surf [fm]  d_surf [fm]
#   15.          1.02        0.6      50.          0.6
#
# ============================================================
```

```
#
# If IOPW=4, enter Wrat = ratio of imaginary to real
# part of M3Y interaction
# If IOPW is not equal to 4, place a '#' sign at the
# beginning of this line, or delete it.
#
# ============================================================
#
#   Wrat
#   1.
#
# ============================================================
#
#
# If IOELAS=1,2 or IOINEL=1,2 enter here THMAX, maximum
# angle (in degrees and in the center of mass),
# and NTHETA (<= NGRID), the number of points in scatering angle.
#
# If IOELAST or IOINEL are not 1, or 2, place a '#' sign
# at the beginning of this line,
# or delete it.
#
# ============================================================
#
#     THMAX       NTHETA
      6.          150
#
# ============================================================
#
# If IOINEL=1 enter the state (JINEL) for the inelastic
# angular distribution.
# If IOINEL is not 1, or 2, place a '#' sign at the
# beginning of this line, or delete it.
#
#
#
# ============================================================
#
#   JINEL
    2
#
# ============================================================
#
# ============================================================
#
```

```
#  NST: number of nuclear levels (<= NSTMAX).
   2
#
# ============================================================
#
# state label (I), energy (EX), and  spin (SPIN).
# I ranges from 1 to NST.
#
# ============================================================
#
#  I     Ex[MeV]    SPIN
   1     0          1.5
   2     1.191      0.5
#
# ============================================================
#
# Reduced matrix elements for E1, E2, E3, M1 and M2 excitations:
#    <I_j||O(E/M;L)||I_i>,      j > i ,
# for the electromagnetic transitions.
# To stop, add a row of zeros at the end of this list.
# If no electromagnetic
# excitation is wanted, enter a row of zeros.
#
# ============================================================
#
#  i -> j  E1[e fm] E2[e fm^2] E3[e fm^3] M1[e fm] M2[e fm^2]
   1    2  0        6.66       0          0.38     0
   0    0  0        0          0          0        0
#
# (P.Napiralla: B(M1)[mu_N^2] = 90.44*B(M1)[e^2fm^2])
# ============================================================
#
# If IOPNUC=1 enter sum rule fraction of nuclear deformation
# parameters for monopole, dipole, quadrupole nuclear
# excitations (DELTE0,DELTE1,DELTE2,DELTE3)
# for each excited state J: DELTE_i = f_i * (sum rule).
# If IOPNUC=0 insert a comment card ('#') in front of each
# entry row, or delete them.
#
# ============================================================
#
#  j      f0           f1           f2           f3
#  2      0            0            0.59         0
#  3      0            1.1          0            0
#
```

```
# ============================================================
#
# If IOGAM=2, enter
# IFF,IGG = initial and final states (iff > igg) for
# the gamma transition.
# THMIN, THMAX = minimum and maximum values of
# gamma-ray angles (in degrees).
# NTHETA = number of angle points (<= NGRID).
#
# ============================================================
#
#   IFF      IGG      THMIN       THMAX         NTHETA
    2        1        0.          179.           179
#
# ============================================================
#
```

Listing B.2: DWEIKO input file ^{197}Au

```
# Input of program 'DWEIKO'
#
# charges and masses (AP,ZP,AT,ZT),
# bombarding energy per nucleon (Einc) in MeV.
#
# Ap       Zp      At       Zt       Einc[MeV/u]
  85       35      197      79       300
# (P.Napiralla: for T2 use Einc: 242)
# IW=0(1) for projectile (target) excitation.
# IOPM=1(0) for output (none) of optical
# model potentials.
# IOELAS=(0)[1]{2} for (no) [center of mass]
# {laboratory} elastic scattering cross section.
# IOINEL=(0)[1]{2} for (no) [center of mass]
# {laboratory} inelastic scattering cross section.
# IOGAM=(0)[1]{2} for (no) output
# [output of statistical tensors] {output of # gamma-ray
#  angular distributions}
#
# ============================================================
#
# IW=0(1)  IOPM=0(1)   IOELAS=0(1)[2]   IOINEL=0(1)[2]  IOGAM=0(1)[2]
  1        1           2                2               2
#
# ============================================================
```

```
# NB=number of impact parameter points (NB <= NBMAX).
# ACCUR=accuracy required for time integration at
# each impact parameter.
# BMIN=minimum impact parameter (enter 0 for default)
# IOB=1(0) prints (does not print) out
# impact parameter probabilities.
#
# ============================================================
#
#  NB          ACCUR         BMIN[fm]      IOB=1(0)
   200         0.001         0             0
#
# ============================================================
#
# OMP switch:
# IOPW=0 (no OMP)       IOPNUC=0 (no nuclear)
#      1 (Woods-Saxon)         1 (vibr. excitat.)
#      2 (read)
#      3 (t-rho-rho folding potential)
#      4 (M3Y folding potential)
# If optical potential is provided (IOPW=2), it should be
# stored in 'optw.in' in rows of
# R x Real[U(R)] x Imag[U(R)].
# The first line in 'optw.in' is the number
# of rows (maximum=NGRID).
#
# ============================================================
#
#      IOPW                          IOPNUC
       1                             0
#
# ============================================================
# If IOPW=1, enter V0_ws [VI_ws] = real part [imaginary]
# (>0, both) of Woods-Saxon.
# r0_ws [r0I_ws] = radius parameter (R_ws = r0 * (ap^1/3 + at^1/3).
#  d_ws [dI_ws]  = diffuseness.
# If IOPW is not equal to 1, place a '#' sign
# at the beginning of this line, or delete it.
#
# ============================================================
#
#   V0 [MeV]   r0[fm]    d[fm]     VI [MeV]    r0_I [fm] dI [fm]
    50.        1.2       0.8       58.         1.2       0.8
#
# ============================================================
```

```
#
# If IOPW=1 and Ap, or At, equal to one (proton),
# enter here spin-orbit part.
# If not, place a '#' sign at the beginning of this line,
# or delete it.
#  VS0 = depth parameter of the spin-orbit potential (>0).
#  r0_S = radius parameter.
#  dS = difuseness.
#  V_surf = depth parameter of the surface potentail (>0).
#  a_surf = difuseness.
#
# ============================================================
#
#   VS0 [MeV]     r0_S [fm]   dS [fm]   V_surf [fm]  d_surf [fm]
#   15.           1.02        0.6       50.          0.6
#
# ============================================================
#
# If IOPW=4, enter Wrat = ratio of imaginary to real
# part of M3Y interaction
# If IOPW is not equal to 4, place a '#' sign at the
# beginning of this line, or delete it.
#
# ============================================================
#
#   Wrat
#   1.
#
# ============================================================
#
#
# If IOELAS=1,2 or IOINEL=1,2 enter here THMAX, maximum
# angle (in degrees and in the center of mass),
# and NTHETA (<= NGRID), the number of points in scatering angle.
#
# If IOELAST or IOINEL are not 1, or 2, place a '#' sign
# at the beginning of this line,
# or delete it.
#
# ============================================================
#
#     THMAX       NTHETA
      6.          150
#
# ============================================================
```

```
#
# If IOINEL=1 enter the state (JINEL) for the inelastic
# angular distribution.
# If IOINEL is not 1, or 2, place a '#' sign at the
# beginning of this line, or delete it.
#
#
#
# ============================================================
#
#   JINEL
    2
#
# ============================================================
#
# ============================================================
#
#  NST: number of nuclear levels (<= NSTMAX).
   2
#
# ============================================================
#
# state label (I), energy (EX), and  spin (SPIN).
# I ranges from 1 to NST.
#
# ============================================================
#
#  I     Ex[MeV]    SPIN
   1     0          1.5
   2     0.5475     3.5
#
# ============================================================
#
# Reduced matrix elements for E1, E2, E3, M1 and M2 excitations:
#    <I_j||O(E/M;L)||I_i>,      j > i ,
# for the electromagnetic transitions.
# To stop, add a row of zeros at the end of this list.
# If no electromagnetic
# excitation is wanted, enter a row of zeros.
#
# ============================================================
#
#  i -> j  E1[e fm] E2[e fm^2] E3[e fm^3] M1[e fm] M2[e fm^2]
   1    2  0        134.01     0          0        0
   0    0  0        0          0          0        0
```

```
#
# (P.Napiralla: B(M1)[mu_N^2] = 90.44*B(M1)[e^2fm^2])
# ============================================================
#
# If IOPNUC=1 enter sum rule fraction of nuclear deformation
# parameters for monopole, dipole, quadrupole nuclear
# excitations (DELTE0,DELTE1,DELTE2,DELTE3)
# for each excited state J: DELTE_i = f_i * (sum rule).
# If IOPNUC=0 insert a comment card ('#') in front of each
# entry row, or delete them.
#
# ============================================================
#
#  j       f0            f1            f2            f3
#  2       0             0             0.59          0
#  3       0             1.1           0             0
#
# ============================================================
#
# If IOGAM=2, enter
# IFF,IGG = initial and final states (iff > igg) for
# the gamma transition.
# THMIN, THMAX = minimum and maximum values of
# gamma-ray angles (in degrees).
# NTHETA = number of angle points (<= NGRID).
#
# ============================================================
#
#   IFF      IGG      THMIN       THMAX         NTHETA
    2        1        0.          179.           179
#
# ============================================================
#
```

C. Compton-camera Approach to ^{197}Au Target Identification

Similar to the target identification process mentioned in Section 4.7.2, γ-ray tracking methods can also be used to pinpoint the position of emission of the γ ray via a process called *Compton imaging*. Detector systems that are based on Compton imaging are called *Compton cameras* that are often used in, e.g, medical applications [Ald17]. Due to AGATA's high position resolution, it can potentially be used as a Compton camera to identify the source position [Ste17].

C.1. Principles of a Compton Camera

In contrast to the usual γ-ray tracking approach starting from the (normally) known source position, a Compton camera operates on the fact that the Compton scattering at an interaction point $\vec{x}_1$ towards $\vec{x}_2$ with a certain deposited energy E_{dep} at $\vec{x}_1$ forms a cone $\mathscr{C}$ pointing towards the potential source position with opening angle θ given by Equation (3.2). This behavior is schematically drawn in Figure C.1. Due to measurement uncertainties in position and energy, the cone has a "thickness" defined by $\Delta\theta$ derived from uncertainty propagation (see Eq. (3.13) and (3.16)). To identify the source position, multiple $x-y$ planes for various values of z are defined. The intersection of the cone $\mathscr{C}$ with all planes is calculated. Via the overlap of many cone intersections with the $x-y$ planes, the original source position can be inferred (see Fig. C.1). If the source is sufficiently small, the $x-y$ plane with the smallest spread of intersection points corresponds to the approximate z-value of the source position. Hence, the source position can be inferred via Compton imaging.

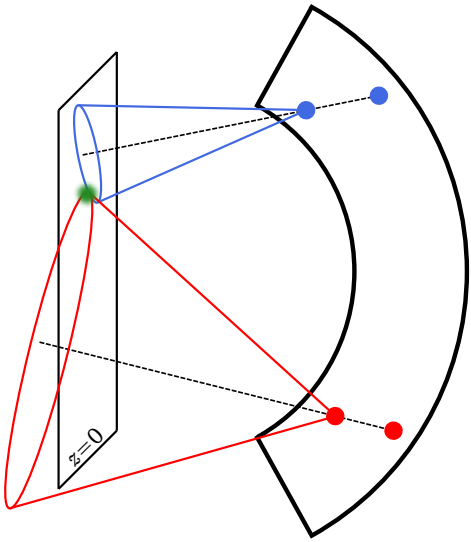

Figure C.1.: Working principle of a Compton camera using AGATA. The measured interaction points of two γ rays (blue and red dots) define cones of possible γ-ray emission directions. The intersection of multiple cones give rise about the potential source position (green dot). See text for details.

C.2. Simulations

Via a *Geant4* simulation using the AGATA simulation code, the "perfect" scenario of a point source at AGATA's nominal position $\vec{x}_S = (0,0,0)^\intercal$ emitting mono-energetic γ rays with an energy of 661.7 keV was tested. The resulting intersection plots for $x-y$ planes with

$$z_i = -200\,\text{mm} + i \cdot 10\,\text{mm}\,, \quad \text{with} \quad i \in \{0,1,\ldots,40\}\,, \tag{C.1}$$

are shown in Figure C.2. For the correct $z_i = 0\,\text{mm}$, the created intersection point of all calculated cones is the smallest. Via a non-linear regression of a Gaussian function on the intersections, the z position with the smallest standard deviation can be calculated – assuming that a Gaussian distribution is sufficient to describe

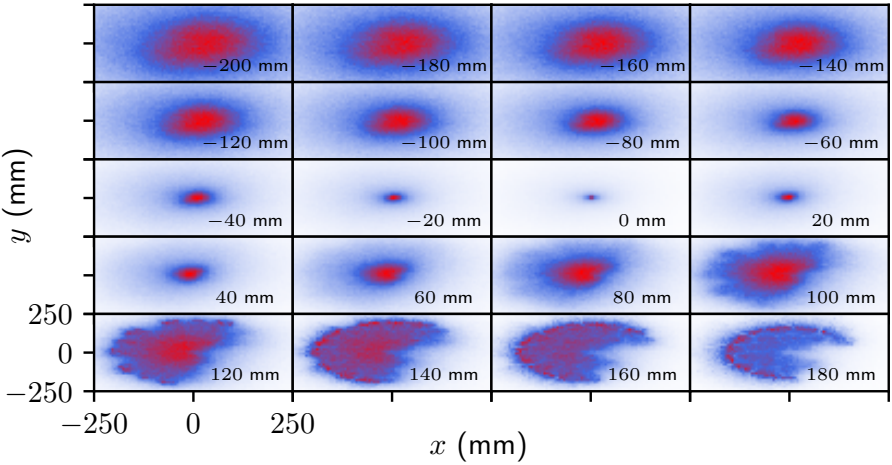

Figure C.2.: Ideal Compton camera scenario with a simulated point source of γ rays situated at $\vec{s} = (0, 0, 0)^\intercal$. Each plot shows an $x-y$ plane with cone intersections from all simulated γ rays. In the bottom right corner of each plot, the corresponding z value of the $x-y$ planes is depicted. The sharpest picture is achieved at $z = 0\,\text{mm}$ – the correct position of the source. The x and y coordinates are only exemplatory depicted for the bottom left plot. At large values of z, a mapping of the detector onto the $x-y$ plane is visible.

the mapping of the cones onto the respective $x-y$ planes. As depicted in Figure C.2, it follows that $z = 0$ is indeed the most likely candidate for the source position. Hence, it is theoretically possible to extract the source position via this approach for the case of a single source. An experimental source identification with AGATA has already been performed for two sources position in an $x-y$ plane [Ste17].

C.3. Multi-target Scenario

In a similar approach, the two-target scenario can be simulated – placing one source at $\vec{x}_{s,1} = (0,0,0)^\intercal$ and another one at $\vec{x}_{s,2} = (0,0,100\,\text{mm})^\intercal$. The resulting intersection plots are shown in Figure C.3. Although a single source position can

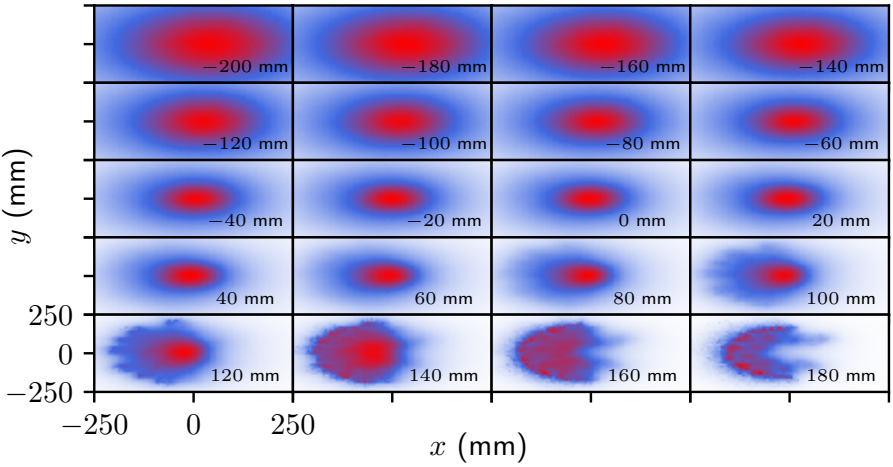

Figure C.3.: Source reconstruction via Compton camera approach for the two gold target scenario of the *Coulex-multipolarimetry* setup. Although the "true" source positions are at $z = 0\,\text{mm}$ and $z = 100\,\text{mm}$, a real distinction between the various plots around $-40\,\text{mm} \leq z \leq 120\,\text{mm}$ is not possible.

potentially be identified, two source positions introduce additional mapping effects. Assuming the two source positions are known, the general problem can be visualized (see Fig. C.4). Drawing the correct paths of the γ rays from $\vec{x}_{s,1}$ to the respective interaction points in AGATA, a "magnified" picture of the cone intersections is mapped onto the $x-y$ plane at $\vec{x}_{s,2}$, blurring the picture of intersections for photons that stem from $\vec{x}_{s,2}$. Vice versa, a reversed and magnified picture of the intersection spot of $\vec{x}_{s,2}$ is mapped onto the $x-y$ plan of $\vec{x}_{s,1}$. This behavior yields large uncertainties in the source positions in z as well as in x and y.

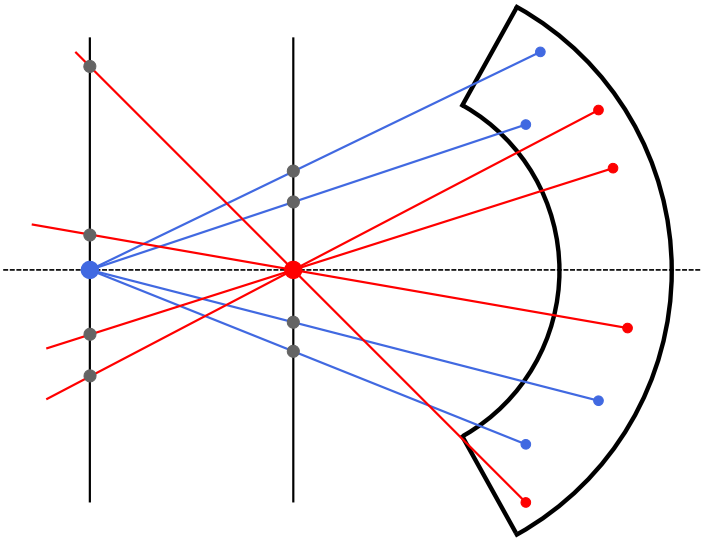

Figure C.4.: Mapping problem of a Compton camera for two source positions with same x and y values, but different z values. The two source positions are depicted as large dots with their respective interactions in AGATA depicted as small dots in the same color (source 1, blue; source 2, red). The second interaction point is necessary to construct the Compton cones (see Fig. C.2) are not depicted for simplicity reasons. The gray dots mark the mapping spots of source position 1 onto the $x-y$ plane of source 2 and vice versa. See text for details.

As depicted in Figure C.4, the uncertainty is too large for a successful discrimination of the two targets. Hence, it is advisable to use the proposed asymmetry methods (see Sec. 4.7.2), accessing the additional information about the x and y coordinates from beam-spot measurements directly. In the case of calculating cone-intersections with additional planes such as multiple $x-z$ or $y-z$ planes, ultimately resulting in a three-dimensional picture of the potential source positions, the mentioned mapping effects are also anticipated.

D. Geometrical Considerations of γ-ray Travel Paths in AGATA

Due to AGATA's assembly in multiple triple clusters, the path between measured interaction points of a single γ ray does not necessarily lie completely in the sensitive HPGe material. A major fraction of it can lie in the air between the detectors. To account for this, two possible contributions have to be subtracted to calculate the actual path of the photon through germanium.

D.1. Inner Sphere

The major influence on the travel distance is the inner sphere of air inside AGATA with a radius of 235 mm with its origin at AGATA's nominal position. Given two measured interaction points in AGATA, called $\vec{x}_1$ and $\vec{x}_2$, the path through air caused by the inner sphere can be determined via calculating the intersection point of the inner sphere with the line

$$\begin{aligned}\vec{g}(\lambda, \vec{x}_1, \vec{x}_2) &= \vec{x}_1 + \lambda \frac{\vec{x}_2 - \vec{x}_1}{||\vec{x}_2 - \vec{x}_1||} \\ &= \vec{x}_1 + \lambda \vec{\Gamma}\,,\end{aligned} \tag{D.1}$$

with $\lambda \in \mathbb{R}$ as a running parameter, representing the position on the line connecting $\vec{x}_1$ and $\vec{x}_2$. Any point $\vec{x} = (x, y, z)^\intercal$ lies on AGATA's inner sphere, if

$$||\vec{x}||^2 = r_{\text{AGATA}}^2\,, \tag{D.2}$$

with the inner radius of AGATA $r_{\text{AGATA}} = 235\,\text{mm}$. To calculate the intersection points of $\vec{g}$ with the inner sphere, all solutions of

$$\sum_{i=1}^{3} \left(x_{1,i}^2 + 2\lambda \Gamma_i x_{1,i} + \lambda^2 \Gamma_i^2 \right) - r_{\text{AGATA}}^2 = 0\,, \tag{D.3}$$

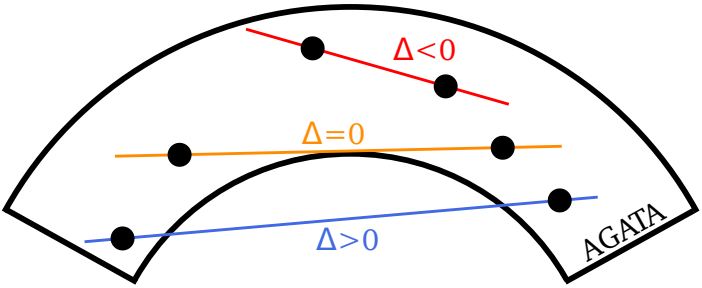

Figure D.1.: Possible intersection scenarios of line $\vec{g}$ with the inner sphere of AGATA. For details on the three possible cases for Δ, see text.

for the parameter λ have to be calculated. Since $||\vec{\Gamma}|| = 1$, all solutions for λ are

$$\lambda_{1,2} = -\langle \vec{x}, \vec{\Gamma} \rangle \pm \sqrt{\langle \vec{x}, \vec{\Gamma} \rangle^2 + r_{\text{AGATA}}^2 - ||\vec{x}_1||^2}\,. \tag{D.4}$$

It is important to note that additional restrictions on λ arise, given by the expression inside the square root

$$\Delta := \langle \vec{x}, \vec{\Gamma} \rangle^2 + r_{\text{AGATA}}^2 - ||\vec{x}_1||^2\,. \tag{D.5}$$

Since a physically sensible travel distance through air is the goal of these calculations, it is necessary that $\sqrt{\Delta} \in \mathbb{R}$. Hence, $\Delta \geq 0$. From this, three scenarios arise:

- $\Delta > 0$: two different values of λ are possible, meaning that the calculated line $\vec{g}$ intersects twice with AGATA's inner sphere.
- $\Delta = 0$: only a single point of contact of $\vec{g}$ with the sphere is present. Line $\vec{g}$ is a tangent line of the sphere.
- $\Delta < 0$: no intersection of line $\vec{g}$ with the sphere is present.

All three scenarios are schematically shown in Figure D.1.

Since solutions to Equation (D.4) for $\Delta \geq 0$ are also possible if no air lies between the interaction points, additional restrictions on λ arise:

- $\lambda > 0$ ensures that only the travel path from $\vec{x}_1$ to $\vec{x}_2$ is considered, ignoring intersections of $\vec{g}$ with the sphere behind $\vec{x}_1$.

- $\lambda \leq ||\vec{x}_2 - \vec{x}_1||$ limits the travel distance through air to areas between $\vec{x}_1$ and $\vec{x}_2$, ignoring intersections of line $\vec{g}$ with the sphere further away from $\vec{x}_1$ than $\vec{x}_2$.

Together with these restrictions on λ, the values λ_1 and λ_2 are used to calculate the distance between the intersection points. Since the directional vector $\vec{\Gamma}$ of $\vec{g}$ is normalized, meaning $||\vec{\Gamma}|| = 1$, the travel distance through AGATA's inner sphere is given by

$$d_{\text{air,Sph.}}(\vec{x}_1, \vec{x}_2) = \begin{cases} |\lambda_2 - \lambda_1|, & \text{if} \quad 0 < \lambda_{1,2} \leq ||\vec{x}_2 - \vec{x}_1|| \\ 0, & \text{else}. \end{cases} \tag{D.6}$$

Since the sign of λ pinpoints the direction of movement along $\vec{g}$, the absolute value of $\lambda_2 - \lambda_1$ is applied.

D.2. Crystal Shapes and Alignment

In addition to the inner sphere of AGATA, the crystal shapes and their geometrical alignment also contribute to the travel path through air of the γ rays. However, in contrast to the inner sphere, no straightforward analytical approach to calculate the travel path through air caused by the crystal shapes can be found. Hence, a different approach is taken. Via measured interaction points from, e.g., a source measurement, the geometrical boundaries of AGATA in the used configuration can be inferred. For a given measured interaction point $\vec{x}$, the spherical coordinates can be expressed via

$$r = \sqrt{\sum_{i=1}^{3} x_i^2}, \tag{D.7}$$

$$\theta = \arccos\left(\frac{x_3}{r}\right), \tag{D.8}$$

$$\varphi = \arctan2\left(x_2, x_1\right), \tag{D.9}$$

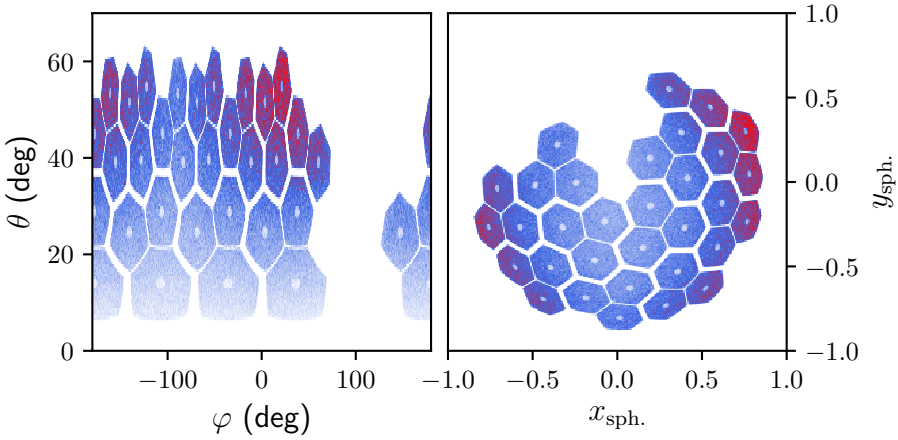

Figure D.2.: *Left*: Spherical angles θ and φ for simulated γ rays. *Right*: For better visibility, the calculated angles are mapped back on their spherical coordinates $x_{\text{sph.}} = \sin\theta\cos\varphi$ and $y_{\text{sph.}} = \sin\theta\sin\varphi$.

with the arctan2 function defined as

$$\operatorname{arctan2}(y,x) := \begin{cases} \arctan(y/x), & \text{if } x > 0, \\ \arctan(y/x) + \pi, & \text{if } x < 0, y > 0, \\ \pm\pi, & \text{if } x < 0, y = 0, \\ \arctan(y/x) - \pi, & \text{if } x < 0, y < 0, \\ +\pi/2, & \text{if } x = 0, y > 0, \\ -\pi/2, & \text{if } x = 0, y < 0. \end{cases} \tag{D.10}$$

In first-order approximation, the influence of r on the travel distance calculation through air is neglected from now on. Via θ and φ, geometrical boundaries of the AGATA crystals can be defined. As depicted in Figure D.2, for small values of θ, AGATA's hole reserved for the beam pipe is present. In addition, the outer boundaries at large values θ are also present. To calculate the distance through air between two interaction points $\vec{x}_1$ and $\vec{x}_2$, starting from $\vec{x}_1$ towards $\vec{x}_2$ and

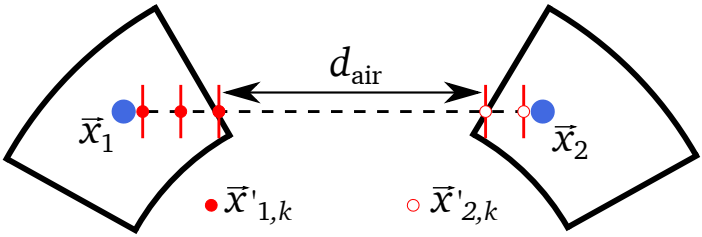

Figure D.3.: Air path reconstruction due to AGATA's detector shapes. The iteration steps are indicated as red lines. the resulting distance d_{air} roughly reproduces the distance through air between the two interaction points (blue dots).

vice versa, two points $\vec{x}'_1$ and $\vec{x}'_2$ are created via

$$\vec{x}'_{i,k} = \vec{x}_i + k \cdot \nu \frac{\vec{x}_j - \vec{x}_i}{||\vec{x}_j - \vec{x}_i||}, \tag{D.11}$$

with $i, j \in \{1,2\}$, $i \neq j$ and $k \in \{1,2,\ldots,n\}$ as the iteration factor. In addition,

$$\nu = \frac{||\vec{x}_j - \vec{x}_i||}{n}, \tag{D.12}$$

with an arbitrarily chosen value $n = 100$, mimicking the maximum amount of steps between $\vec{x}_1$ and $\vec{x}_2$, is used to move $\vec{x}'_{1,k}$ closer to $\vec{x}_2$ and $\vec{x}'_{2,k}$ closer to $\vec{x}_1$. At each iteration, the spherical coordinates of $\vec{x}'_{1,k}$ and $\vec{x}'_{2,k}$ are calculated. If their respective angles θ and φ lie outside of the detector geometry defined in Figure D.2, the respective iteration of $\vec{x}'_{i,k}$ is aborted. If both iterations stopped, the distance between $\vec{x}'_{1,k}$ and $\vec{x}'_{2,k}$ calculated via

$$d_{\text{air,Crys.}}(\vec{x}_1, \vec{x}_2) = ||\vec{x}'_{1,k} - \vec{x}'_{2,k}||, \tag{D.13}$$

and is set as the travel distance of the photon through air between the crystals. The explained iterative procedure is schematically drawn in Figure D.3. Hence, the complete traveled distance through air between $\vec{x}_1$ and $\vec{x}_2$ is

$$d_{\text{air}}(\vec{x}_1, \vec{x}_2) = d_{\text{air,Sph.}}(\vec{x}_1, \vec{x}_2) + d_{\text{air,Crys.}}(\vec{x}_1, \vec{x}_2). \tag{D.14}$$

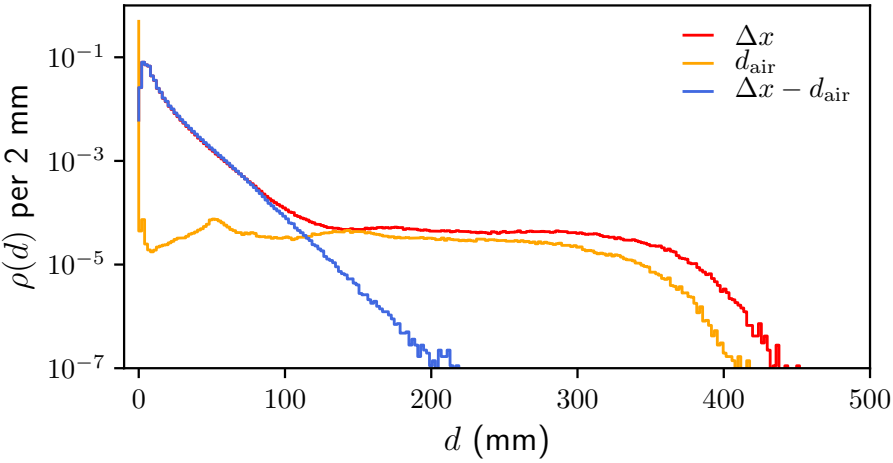

Figure D.4.: Travel path between two interaction points without any air distance correction Δx (red), the distance solely through air d_{air} (orange) and the corrected travel distances $\Delta x - d_{\text{air}}$ (blue). After subtracting the air path, an exponential distribution is present.

To test the performance of the proposed methods, 10^6 simulated γ rays via a *Geant4* simulation with the AGATA simulation code are used. Here, only γ rays with an incident energy of 661.7 keV that interacted at least twice with AGATA are analyzed[1]. To check, whether the proposed methods works, the travel distance between the first two interaction points of the γ rays can be used. Since this distance is only governed by the mean free path of the photons, the travel distance should show an exponentially decaying behavior, if the γ rays only travel through germanium (see Sec. 3.4.2). As shown in Figure D.4, the expected behavior for air path corrected distances is present, showing an exponential decay as a function of d for $d \geq 50\,\text{mm}$. At smaller values, interaction point merging causes deviations from the expected exponential behavior (see Chaps. 5 and 6 for details).

[1]The used events are part of the simulated γ-decay events mentioned in Chapter 6.

Bibliography

[Ago03] S. Agostinelli et al. *Geant4 – a simulation toolkit*. *Nuclear Instruments and Methods in Physics Research A* **506** (2003), 250. doi: 10.1016/S0168-9002(03)01368-8.

[Akk12] A. Akkoyun et al. *AGATA–Advanced GAmma Tracking Array*. *Nuclear Instruments and Methods in Physics Research A* **668** (2012), 26. doi: 10.1016/j.nima.2011.11.081.

[Ald17] S. Aldawood et al. *Development of a Compton camera for prompt-gamma medical imaging*. *Radiation Physics and Chemistry* **140** (2017), 190. doi: 10.1016/j.radphyschem.2017.01.024.

[Ald56] K. Alder et al. *Study of Nuclear Structure by Electromagnetic Excitation with Accelerated Ions*. *Reviews of Modern Physics* **28** (1956), 432. doi: 10.1103/RevModPhys.28.432.

[AW66] K. Alder and A. Winther. *Coulomb Excitation*. New York: Academic Press, 1966.

[AW75] K. Alder and A. Winther. *Electromagnetic excitation: Theory of Coulomb excitation with heavy ions*. Amsterdam-Oxford: North-Holland Publishing Company, 1975.

[AW79] K. Alder and A. Winther. *Relativistic Coulomb Excitation*. *Nuclear Physics A* **319** (1979), 518. doi: 10.1016/0375-9474(79)90528-1.

[All06] J. Allison et al. *Geant4 Developments and Applications*. *IEEE Transactions on Nuclear Science* **53** (2006), 270. doi: 10.1109/TNS.2006.869826.

[All16] J. Allison et al. *Recent developments in GEANT4*. *Nuclear Instruments and Methods in Physics Reasearch A* **835** (2016), 186. doi: 10.1016/j.nima.2016.06.125.

[Baz04] D. Bazzaco. *Nuclear Physics A (Proceedings of the 2029Sixth International Conference on Radioactive Nuclear Beams (RNB6))* (2004), 248.

[Ber10] M. J. Berger et al. *XCOM: Photon Cross Sections Database*. 2010. url: https://www.nist.gov/pml/xcom-photon-cross-sections-database.

[Ber99] C. Bertulani. *A computer program for relativistic multiple Coulomb and nuclear excitation*. *Computer Physics Communications* **116** (1999), 23. doi: 10.1016/S0010-4655(98)00141-6.

[Ber] C. Bertulani. visited: 21.10.2019. url: http://cpc.cs.qub.ac.uk/summaries/ADRN_v1_0.html.

[Bez81] J. C. Bezdek. *Pattern recognition with fuzzy objective function algorithms*. Vol. 1. New York: Plenum Press, 1981.

[Bir17] J. Birkhan et al. *Electric Dipole Polarizability of ^{48}Ca and Implications for the Neutron Skin*. *Physical Review Letters* **118** (2017), 252501. doi: 10.1103/PhysRevLett.118.252501.

[Bos19] A. Boso et al. *Isospin dependence of electromagnetic transition strengths among an isobaric triplet*. *Physics Letters B* **797** (2019), 134835. doi: 10.1016/j.physletb.2019.134835.

[Bru18] D. Brugnara. *Perspectives on the measurement of competitive double gamma decay with the AGATA tracking array*. M.Sc. thesis. Università degli studi di Padova, 2018. url: http://tesi.cab.unipd.it/61177/.

[Bru96] D. Brusa et al. *Fast sampling algorithm for the simulation of photon Compton scattering*. *Nuclear Instruments and Methods in Physics Research A* **379** (1996), 167. doi: 10.1016/0168-9002(96)00652-3.

[Bru13] B. Bruyneel et al. *Correction for hole trapping in AGATA detectors using pulseshape analysis*. *European Physical Journal A* **49** (2013), 61. doi: 10.1140/epja/i2013-13061-4.

[Bru16] B. Bruyneel et al. *Pulse shape analysis and position determination in segmented HPGe detectors: The AGATA detector library*. *European Physical Journal A* **52** (2016), 70. doi: 10.1140/epja/i2016-16070-9.

[Cas05] R. F. Casten. *Nuclear Structure from a Simple Perspective*. Vol. 2. Oxford, New York: Oxford University Press, 2005.

[Clé17] E. Clément. *Conceptual design of the AGATA 1π array at GANIL*. *Nuclear Instruments and Methods in Physics Research A* **855** (2017), 1. doi: 10.1016/j.nima.2017.02.063.

[Clé18] E. Clément et al. *The AGATA Campaigns at GSI and GANIL*. *Nuclear Physics News* **28** (2018), 16. doi: 10.1080/10619127.2018.1495478.

[Cli69] D. Cline. *Bulletin of the American Physical Society* **14** (1969), 726.

[Don10] M. Doncel et al. *Experimental test of the background rejection, through imaging capability, of a highly segmented AGATA germanium detector*. *Nuclear Instruments and Methods in Physics Research A* **622** (2010), 614. doi: 10.1016/j.nima.2010.07.069.

[Dud17] J. Dudouet et al. $^{96}_{36}Kr_{60}$ *– Low-Z Boundary of the Island of Deformation at* $N = 6$. *Physical Review Letters* **118** (2017), 162501. doi: 10.1103/PhysRevLett.118.162501.

[ES08] J. Eberth and J. Simpson. *From Ge(Li) detectors to gamma-ray tracking arrays – 50 years of gamma spectroscopy with germanium detectors*. *Progress in Particle and Nuclear Physics* **60** (2008), 283–337. doi: 10.1016/j.ppnp.2007.09.001.

[EK17] J. Eckle-Kohler and M. Kohler. *Eine Einführung in die Statistik und ihre Anwendungen*. Vol. 3. Berlin: Springer Spektrum, 2017. doi: 10.1007/978-3-662-54094-7.

[Els18] J. Elstrodt. *Maß- und Integrationstheorie*. Vol. 8. Berlin: Springer Spektrum, 2018. doi: 10.1007/978-3-662-57939-8.

[Ess96] H. Essel et al. *The new data acquisition system at GSI*. *IEEE Transactions on Nuclear Science* **43** (1996), 1. doi: 10.1109/23.486018.

[EK99] H. Essel and N. Kurz. *The general purpose data acquisition system MBS*. *IEEE Conference on Real-Time Computer Applications in Nuclear Particle and Plasma Physics* **475** (1999). doi: 10.1109/RTCON.1999.842672.

[Far10] E. Farnea et al. *Conceptual design and Monte Carlo simulations of the AGATA array*. *Nuclear Instruments and Methods in Physics Research A* **621** (2010), 331.
doi: 10.1016/j.nima.2010.04.043.

[Fla09] K. T. Flanagan et al. *Nuclear Spins and Magnetic Moments of ^{71,73,75}Cu: Inversion of $\pi 2p_{3/2}$ and $\pi 1f_{5/2}$ Levels in ^{75}Cu*. *Physical Review Letters* **103** (2009), 142501.
doi: 10.1103/PhysRevLett.103.142501.

[Fli18] T. Fließbach. *Quantenmechanik*. Vol. 6. Berlin: Springer Spektrum, 2018.
doi: 10.1007/978-3-662-58031-8.

[Fra98] S. Franchoo et al. *Beta Decay of $^{68-74}$Ni and Level Structure of Neutron-Rich Cu Isotopes*. *Physical Review Letters* **81** (1998), 3100.
doi: 10.1103/PhysRevLett.81.3100.

[Fra01] S. Franchoo et al. *Monopole migration in ^{69,71,73}Cu observed from β decay of laser-ionized $^{68-74}$Ni*. *Physical Review C* **64** (2001), 054308.
doi: 10.1103/PhysRevC.64.054308.

[Fri75] J. L. Friar. *Low-Energy Theorems for Nuclear Compton and Raman Scattering and $0^+ \to 0^+$ Two-Photon Decays in Nuclei*. *Annals of Physics* **95** (1975), 170.
doi: 10.1016/0003-4916(75)90049-4.

[Gad14] A. Gade et al. *Nuclear Structure Towards $N = 40$ ^{60}Ca: In-Beam γ-Ray Spectroscopy of ^{58,60}Ti*. *Physical Review Letters* **112** (2014), 112503.
doi: 10.1103/PhysRevLett.112.112503.

[Gad11] A. Gadea et al. *Conceptual design and infrastructure for the installation of the first AGATA sub-array at LNL*. *Nuclear Instruments and Methods in Physics Research A* **654** (2011), 88.
doi: 10.1016/j.nima.2011.06.004.

[Gei92] H. Geissel et al. *The GSI projectile fragment separator (FRS): a versatile magnetic system for relativistic heavy ions*. *Nuclear Instruments and Methods in Physics Research Section B* **70** (1992), 14.
doi: 10.1016/0168-583X(92)95944-M.

[Gei09] H. Geissel et al. *Technical Design Report on the Super-FRS*. *Technical report, GSI* (2009).
url: https://fair-center.eu/for-users/experiments/nustar/documents/technical-design-reports.html.

[Geo07] H.-O. Georgii. *Stochastics*. Vol. 1. Berlin, New York: Walter de Gruyter, 2007.

[Gol13] P. Golubev et al. *The Lund-York-Cologne Calorimeter (LYCCA): Concept, design and prototype developments for a FAIR-NUSTAR detector system to discriminate relativistic heavy-ion reaction products*. *Nuclear Instruments and Methods in Physics Research A* **723** (2013), 55.
doi: 10.1016/j.nima.2013.04.058.

[Göp30] M. Göppert-Mayer. *Über Elementarakte mit zwei Quantensprüngen*. PhD thesis. Universität Göttingen, 1930.
doi: 10.1002/andp.19314010303.

[Göp48] M. Göppert-Mayer. *On Closed Shells in Nuclei*. *Physical Review* **74** (1948), 235.
doi: 10.1103/PhysRev.74.235.

[Göp49] M. Göppert-Mayer. *On Closed Shells in Nuclei II*. *Physical Review* **75** (1949), 1969.
doi: 10.1103/PhysRev.75.1969.

[GRE17] GRETA (Gamma-Ray Energy Tracking Array). *Conceptual Design Report*. 2017.
url: http://greta.lbl.gov/documents.

[Hax49] O. Haxel et al. *On the "Magic Numbers" in Nuclear Structure*. *Physical Review* **75** (1949), 1766.
doi: 10.1103/PhysRev.75.1766.2.

[Hei60] W. Heitler. *The Quantum Theory of Radiation*. Vol. 3. Oxford: Clarendon Press, 1960.

[Hoi11] R. Hoischen et al. *Fast timing with plastic scintillators for in-beam heavy-ion spectroscopy*. *Nuclear Instruments and Methods in Physics Research A* **654** (2011), 354.
doi: 10.1016/j.nima.2011.07.013.

[Hol11] M. Holtz. *Sparse Grid Quadrature in High Dimensions with Applications in Finance and Insurance*. Vol. 1. Berlin, Heidelberg: Springer, 2011. doi: 10.1007/978-3-642-16004-2.

[Hub90] F. Hubert et al. *Range and Stopping-power tables for* 2.5—500 *MeV/Nucleon Heavy Ions in Solids*. *Atomic Data and Nuclear Data* **46** (1990), 1.

[HT75] M. H. Hurdus and L. Tomlinson. *Gamma-ray emission from* $^{84-87}$*Se and* $^{85-88}$*Br isotopes*. *Journal of Inorganic and Nuclear Chemistry* **37** (1975), 1. doi: 10.1016/0022-1902(75)80114-X.

[IA87] F. Iachello and A. Arima. *The interacting boson model*. Cambridge, New York, Melbourne: Cambridge University Press, 1987.

[Iwa14] H. Iwasaki et al. *Evolution of Collectivity in* ^{72}*Kr: Evidence for Rapid Shape Transition*. *Physical Review Letters* **112** (2014), 142502. doi: 10.1103/PhysRevLett.112.142502.

[Joh14] P. R. John et al. *Shape evolution in the neutron-rich osmium isotopes: Prompt* γ*-ray spectroscopy of* ^{196}*Os*. *Physical Review C* **90** (2014), 021301(R). doi: 10.1103/PhysRevC.90.021301.

[Joh17] P. R. John et al. *In-beam* γ*-ray spectroscopy of the neutron-rich platinum isotope* ^{200}*Pt toward the* $N = 126$ *shell gap*. *Physical Review C* **95** (2017), 064321. doi: 10.1103/PhysRevC.95.064321.

[Kay19] L. Kaya et al. *Identification of high-spin proton configurations in* ^{136}*Ba and* ^{137}*Ba*. *Physical Review C* **99** (2019), 014301. doi: 10.1103/PhysRevC.99.014301.

[Kip10] R. Kipling. *Rewards and Fairies*. London: Macmillan and Co., 1910.

[Kne96] U. Kneissl et al. *Investigation of nuclear structure by resonance fluorescence scattering*. *Progress in Particle and Nuclear Physics* **37** (1996), 349. doi: 10.1016/0146-6410(96)00055-5.

[Kno00] G. F. Knoll. *Radiation Detection and Measurement*. Vol. 3. New York: John Wiley & Sons, 2000.

[KL19] A. Korichi and T. Lauritsen. *Tracking γ rays in highly segmented HPGe detectors: A review of AGATA and GRETINA*. *European Physical Journal A* **55** (2019), 121.
doi: 10.1140/epja/i2019-12787-1.

[Kra87] J. Kramp et al. *Nuclear Two-Photon Decay in $0^+ \rightarrow 0^+$ Transitions*. *Nuclear Physics A* **474** (1987), 412.
doi: 10.1016/0375-9474(87)90625-7.

[Lee04] I. Y. Lee et al. *GRETINA: A gamma ray energy tracking array*. *Nuclear Physics A* **746** (2004), 255c.
doi: 10.1016/j.nuclphysa.2004.09.038.

[Lee90] I.Y. Lee. *The GAMMASPHERE*. *Nuclear Physics A* **520** (1990), c641.
doi: 10.1016/0375-9474(90)91181-P.

[Leo94] W. R. Leo. *Techniques for Nuclear and Particle Physics Experiments – A How-to Approach*. Vol. 2. Berlin: Springer, 1994.
doi: 10.1007/978-3-642-57920-2.

[Lie01] R.M. Lieder et al. *The TMR network project "Development of γ-ray tracking detectors"*. *Nuclear Physics A* **682** (2001), 279c.
doi: 10.1016/S0375-9474(00)00651-5.

[LS96] J. Lindhard and A. H. Sørensen. *Relativistic theory of stopping for heavy ions*. *Physical Review A* **53** (1996), 2443.
doi: 10.1103/PhysRevA.53.2443.

[Löb72] K. E. G. Löbner et al. *$E1-M2-E3$ Mixing of the 1159.3 keV Transition in ^{176}Hf*. *Nuclear Physics A* **179** (1972), 276.
doi: 10.1016/0375-9474(72)90369-7.

[Lop04] A. Lopez-Martens et al. *γ-ray tracking algorithms: a comparison*. *Nuclear Instruments and Methods in Physics Research A* **533** (2004), 454.
doi: 10.1016/j.nima.2004.06.154.

[Maj94] A. Maj et al. *Angular distribution of photons from the decay of the GDR in hot and rotating light Yb nuclei from exclusive experiments*. *Nuclear Physics A* **571** (1994), 185.
doi: 10.1016/0375-9474(94)90347-6.

[MC99] J. van der Marel and B. Cederwall. *Backtracking as a way to reconstruct Compton scattered γ-rays*. *Nuclear Instruments and Methods in Physics Research A* **437** (1999), 538. doi: 10.1016/S0168-9002(99)00801-3.

[MC02] J. van der Marel and B. Cederwall. *γ-ray tracking in germanium: the backtracking method*. *Nuclear Instruments and Methods in Physics Research A* **477** (2002). 5th Int. Conf. on Position-Sensitive Detectors, 391. doi: 10.1016/S0168-9002(01)01837-X.

[MC03] L. Milechina and B. Cederwall. *Improvements in γ-ray reconstruction with positive sensitive Ge detectors using the backtracking method*. *Nuclear Instruments and Methods in Physics Research A* **508** (2003), 394. doi: 10.1016/S0168-9002(03)01698-X.

[Mül12] T. Müller-Gronbach et al. *Monte Carlo-Algorithmen*. Vol. 1. Berlin, Heidelberg: Springer, 2012. doi: 10.1007/978-3-540-89141-3.

[Nap16] P. Napiralla. *New Methods for the Gamma-Ray Tracking with position-sensitive High-Purity Germanium detectors*. M.Sc. thesis. Technische Universität Darmstadt, 2016.

[Nap20a] P. Napiralla et al. *Approach to a Self-calibrating Experimental γ-ray Tracking Algorithm*. *Nuclear Instruments and Methods in Physics Research A* (2020). (submitted).

[Nap20b] P. Napiralla et al. *First Benchmark of Coulex-multipolarimetry via an ^{85}Br $\pi p_{3/2} \rightarrow \pi p_{1/2}$ Spin-flip Experiment with Relativistic Ion Beams*. *European Physics Journal A* (2020). (in preparation).

[Ola06] A. Olariu et al. *Pulse shape analysis for the location of the gamma-interactions in AGATA*. *IEEE Transactions on Nuclear Science* **53** (2006), 1028. doi: 10.1109/tns.2006.875130.

[Ots05] T. Otsuka et al. *Evolution of Nuclear Shells due to the Tensor Force*. *Physical Review Letters* **95** (2005), 232502. doi: 10.1103/PhysRevLett.95.232502.

[Ots10] T. Otsuka et al. *Novel Features of Nuclear Forces and Shell Evolution in Exotic Nuclei*. *Physical Review Letters* **104** (2010), 012501. doi: 10.1103/PhysRevLett.104.012501.

[Pie14] N. Pietralla et al. *On the Road to FAIR: 1$^{st.}$ Operation of AGATA in Pre-SPEC at GSI*. *EPJ Web of Conferences* **66** (2014), 02083. doi: 10.1051/epjconf/20146602083.

[Pov14] B. Povh et al. *Particles and Nuclei*. Vol. 7. Berlin, Heidelberg: Springer, 2014. doi: 10.1007/978-3-662-46321-5.

[Rac42] G. Racah. *Theory of Complex Spectra II*. *Physical Review* **62** (1942), 438. doi: 10.1103/PhysRev.62.438.

[Rai06] G. Rainovski et al. *Stabilization of Nuclear Isovector Valence-Shell Excitations*. *Physical Review Letters* **96** (2006), 122501. doi: 10.1103/PhysRevLett.96.122501.

[Ral17a] D. Ralet et al. *Lifetime measurement of neutron-rich even-even molybdenum isotopes*. *Physical Review C* **95** (2017), 034320. doi: 10.1103/PhysRevC.95.034320.

[Ral17b] D. Ralet et al. *Toward lifetime and g factor measurements of short-lived states in the vicinity of ^{208}Pb*. *Physica Scripta* **92** (2017), 054004. doi: 10.1088/1402-4896/aa6942.

[Rec09a] F. Recchia et al. *Performance of an AGATA prototype detector estimated by Compton-imaging techniques*. *Nuclear Instruments and Methods in Physics Research A* **604** (2009), 60. doi: 10.1016/j.nima.2009.01.079.

[Rec09b] F. Recchia et al. *Position resolution of the prototype AGATA triple-cluster detector from an in-beam experiment*. *Nuclear Instruments and Methods in Physics Research A* **604** (2009), 555. doi: 10.1016/j.nima.2009.02.042.

[Ree18] M. Reese. *Intermediate-energy Coulomb excitation with the PreSPEC-AGATA setup*. PhD thesis. Technische Universität Darmstadt, 2018. url: https://tuprints.ulb.tu-darmstadt.de/7327/.

[Ree] M. Reese. *elder-pt – data flow framework for data analysis applications*. visited on 21.10.2019.
url: https://sourceforge.net/projects/elderpt/.

[Ree13] M. Reese et al. *Position Sensitivity of LYCCA Time-of-Flight Detectors*. *GSI Report* **1** (2013), 185.
url: http://repository.gsi.de/record/52876.

[RN10] P.-G. Reinhard and W. Nazarewicz. *Information content of a new observable: The case of the nuclear neutron skin*. *Physical Review C* **81** (2010), 051303(R).
doi: 10.1103/PhysRevC.81.051303.

[Rib75] R. Ribberfors. *Relationship of the relativistic Compton cross section to the momentum distribution of bound electron states*. *Physical Review B* **12** (1975), 6.
doi: 10.1103/PhysRevB.12.2067.

[RB82] R. Ribberfors and K.-F. Berggren. *Incoherent-x-ray-scattering functions and cross sections* $(d\sigma/d\Omega')_{incho}$ *by means of a pocket calculator*. *Physical Review A* **26**.6 (1982).
doi: 10.1103/PhysRevA.26.3325.

[Sch11a] M. Schlarb et al. *Pulse shape analysis for* γ *-ray tracking (Part II): Fully informed particle swarm algorithm applied to AGATA*. *European Physical Journal A* **47** (2011), 131.
doi: 10.1140/epja/i2011-11131-3.

[Sch11b] M. Schlarb et al. *Pulse shape analysis for* γ*-ray tracking (Part I): Pulse shape simulation with JASS*. *European Physical Journal A* **47** (2011), 132.
doi: 10.1140/epja/i2011-11132-2.

[Sim97] J. Simpson. *The Euroball Spectrometer*. *Zeitschrift für Physik A* **358** (1997), 139.
doi: 10.1007/s002180050290.

[SS06] D. Sivia and J. Skilling. *Data Analysis – A Bayesian Tutorial*. Vol. 2. Oxford: Oxford University Press, 2006.

[Söd11] P.-A. Söderström et al. *Interaction position resolution simulations and in-beam measurements of the AGATA HPGe detectors*. *Nuclear Instruments and Methods in Physics Research A* **638** (2011), 96. doi: 10.1016/j.nima.2011.02.089.

[Sol92] V.G. Soloviev. *Theory of Atomic Nuclei: Quasiparticles and Phonons*. London: IOP Publishing Ltd., 1992.

[Sta15a] C. Stahl. *New methods for the γ-ray spectroscopy with position-sensitive detector systems*. PhD thesis. Technische Universität Darmstadt, 2015. url: https://tuprints.ulb.tu-darmstadt.de/4955/.

[Sta13] C. Stahl et al. *Identification of the proton* $2p_{1/2} \rightarrow 2p_{3/2}$ *M*1 *spin-flip transition in* ^{87}*Rb*. *Physical Review C* **87** (2013), 037302. doi: 10.1103/PhysRevC.87.037302.

[Sta15b] C. Stahl et al. *Coulex-multipolarimetry with relativistic heavy-ion beams*. *Nuclear Instruments and Methods in Physics Research A* **770** (2015), 123. doi: 10.1016/j.nima.2014.10.024.

[Sta15c] C. Stahl et al. *Population of the* 2^+_{ms} *mixed-symmetry state of* ^{140}*Ba with the α-transfer reaction*. *Physical Review C* **92** (2015), 044324. doi: 10.1103/PhysRevC.92.044324.

[Sta17] C. Stahl et al. *APCAD – Analysis program for the continous-angle DSAM*. *Computer Physics Communications* **214** (2017), 174. doi: 10.1016/j.cpc.2017.01.009.

[Ste17] T. Steinbach et al. *Compton imaging with a highly-segmented, position-sensitive HPGe detector*. *European Physical Journal A* **53** (2017), 23. doi: 10.1140/epja/i2017-12214-9.

[Stu88] A. E. Stuchbery et al. *Measured Gyromagnetic Ratios and the Low-excitation Spectroscopy of* ^{197}*Au*. *Nuclear Physics A* **486** (1988), 374. doi: 10.1016/0375-9474(88)90242-4.

[Suh07] J. Suhonen. *From Nucleons to Nuclei*. Vol. 1. Berlin, Heidelberg: Springer, 2007. doi: 10.1007/978-3-540-48861-3.

[Tan19] R. Taniuchi et al. ^{78}*Ni revealed as a doubly magic stronghold against nuclear deformation*. *Nature* **569** (2019), 53. doi: 10.1038/s41586-019-1155-x.

[TB08] O. Tarasov and D. Bazin. *LISE++: Radioactive beam production with in-flight separators*. *Nuclear Instruments and Methods in Physics Research B* **266** (2008), 4657.
doi: 10.1016/j.nimb.2008.05.110.

[TG10] S. Tashenov and J. Gerl. *TANGO – New tracking ALGOrithm for gamma-rays*. *Nuclear Instruments and Methods in Physics Research A* **622** (2010), 592.
doi: 10.1016/j.nima.2010.07.040.

[The06] H. Theissen. *Spectroscopy of light nuclei by low energy (< 70 MeV) inelastic electron scattering*. *Springer Tracts in Modern Physics* **65** (2006), 1.
doi: 10.1007/BFb0041391.

[Übe71] H. Überall. *Electron Scattering from Complex Nuclei*. New York, London: Academic Press, 1971.

[VB04] R. Venturelli and D. Bazzacco. *Adaptive Grid Search as Pulse Shape Analysis Algorithm for γ-Tracking and Results*. *LNL Annual Report 2004* (2004).
url: https://www.lnl.infn.it/~annrep/read_ar/2004/.

[Vog15] A. Vogt et al. *Light and heavy transfer products in ^{136}Xe + ^{238}U multinucleon transfer reactions*. *Physical Review C* **92** (2015), 024619.
doi: 10.1103/PhysRevC.92.024619.

[Vog17] A. Vogt et al. *Isomers and high-spin structures in the $N = 81$ isotones ^{135}Xe and ^{137}Ba*. *Physical Review C* **95** (2017), 024316.
doi: 10.1103/PhysRevC.95.024316.

[Wal14] C. Walz. *The two-photon decay of the $\frac{11}{2}^-$ isomer of ^{137}Ba and mixed-symmetry states of $^{92,94}Zr$ and ^{94}Mo*. PhD thesis. Technische Universität Darmstadt, 2014.
url: https://tuprints.ulb.tu-darmstadt.de/4056/.

[Wal15] C. Walz et al. *Observation of the competitive double-gamma nuclear decay*. *Nature* **526** (2015), 406.
doi: 10.1038/nature15543.

[Wei10] H. Weick. *ATIMA, calculate ATomic Interaction with MAtter (www interface)*. 2010.
url: https://web-docs.gsi.de/~weick/atima/.

[Wei03] D. W. Weißhaar. *MINIBALL – Ein neuartiges Gamma-Spektrometer mit ortsauflösenden Germaniumdetektoren*. PhD thesis. Universität zu Köln, 2003.
url: https://kups.ub.uni-koeln.de/718/.

[Wol19] C. Wolf et al. *Constraining the Neutron Star Compactness: Extraction of the $^{23}Al(p,\gamma)$ Reaction Rate for the rp Process*. *Physical Review Letters* **122** (2019), 232701.
doi: 10.1103/PhysRevLett.122.232701.

[Wol92] H.-J. Wollersheim. *Kernstruktur schnell rotierender Atomkerne*. Habilitation treatise. Johann-Wolfgang Goethe-Universität Frankfurt, 1992.
url: https://web-docs.gsi.de/~wolle/.

[YN17] M. S. Yang and Y. Nataliani. *Robust-learning fuzzy c-means clustering algorithm with unknown number of clusters*. *Pattern Recognition* **71** (2017), 45.
doi: 10.1016/j.patcog.2017.05.017.

List of Figures

List of Tables

List of Publications

Publications

- **P. Napiralla**, D. Brugnara, E. Clément, H. Egger, A. Goasduff, P. R. John, R. Kern, H. Li, N. Pietralla, and J. J. Valiente-Dobón. *Approach to a Self-calibrating Experimental γ-ray Tracking Algorithm*. Nuclear Instruments and Methods in Physics Research A (submitted).

- **P. Napiralla**, M. Lettmann, C. Stahl, G. Rainovski, N. Pietralla, S. Afara, F. Ameil, T. Arici, S. Aydin, M. A. Bentley, A. Blazhev, P. Boutachkov, M. L. Cortés, H. Egger, C. Fahlander, J. Gerl, K. A. Gladnishki, P. Golubev, M. Górska, A. Gottardo, L. Grassi, T. Habermann, D. G. Jenkins, P. R. John, J. Jolie, I. Kojouharov, N. Lalović, C. Lizarazo, C. Louchart-Henning, D. Mengoni, E. Merchan, O. Möller, T. Möller, K. Moschner, V. Modamio, D. Napoli, B. S. Nara Singh, S. Pietri, D. Ralet, M. Reese, P. Reiter, D. Rudolph, L. G. Sarmiento, H. Schaffner, P. P. Singh, J. J. Valiente-Dobón, V. Werner, and O. Wieland. *First Benchmark of Coulex-multipolarimetry via an ^{85}Br $\pi p_{3/2} \rightarrow \pi p_{1/2}$ Spin-flip Experiment with Relativistic Ion Beams*. European Physics Journal A (in preparation).

Conference Proceedings

- D. Brugnara, J. J. Valiente-Dobón, A. Goasduff, N. Pietralla, **P. Napiralla**, P. R. John, E. Clément, and D. Mengoni. *Perspectives on the measurement of competitive double gamma decay with the AGATA tracking array*. Il Nuovo Cimento 42 C (2019) 92.

Laboratory Reports

- **P. Napiralla**, H. Egger, P. R. John, N. Pietralla, M. Reese, and C. Stahl. *Bayes-Tracking – A novel approach to γ-ray tracking*. GSI Scientific Report 2016.
- **P. Napiralla**, H. Egger, P. R. John, N. Pietralla, M. Reese, and C. Stahl. *Fuzzy Bayes Tracking – Experimental results*. GSI Scientific Report 2017.

Danksagung

Mein größter Dank gilt Herrn Prof. Dr. Dr. h.c. mult. Norbert Pietralla, der mich über einige Umwege über den Fachbereich Mathematik für das eher unkonventionelle Gebiet des γ-ray Trackings und dessen Anwendung in der Kernstrukturphysik begeistern konnte. Für die zahlreichen interessanten Diskussionen, Ratschläge und Anregungen möchte ich mich herzlich bei ihm bedanken.

Desweiteren danke ich Herrn Prof. Dr. Herbert Egger und Christian Stahl, deren mathematische und physikalische Ratschläge eine große Hilfe in der Ausarbeitung der verschiedenen Tracking-Algorithmen waren. Dank ihnen war es möglich, das Bayes-Tracking auszuarbeiten, welches den Grundstein dieser gesamten Arbeit darstellt.

Meinen ehemaligen Kollegen Marc Lettmann und Michael Reese möchte ich herzlich für die Hilfe bei der Einarbeitung und Analyse des ^{85}Br Experiments danken. Hierdurch haben sie mir eine rasche Einarbeitung in das Themengebiet ermöglicht. Außerdem möchte ich mich bei ihnen für die nette Zusammenarbeit bedanken.

Für die schöne Zeit im Institut für Kernphysik, die ich sehr vermissen werde, möchte ich meinen Kollegen Marcel Berger[1], Udo Friman-Gayer, Johannes Wiederhold, Tobias Beck, Marc Lettmann, Marius Peck, Andreas Weber, Oliver Papst, Jörn Kleemann, Philipp R. John, Philipp C. Ries, Waldemar Witt, Cesar Lizarazo, Pavlos Koseoglou, Robert Stegmann, Pär-Anders Söderström, Christoph Kremer, Ronan Lefol, Radostina Zidarova, Oliver Möller, Volker Werner und natürlich Marius Peck danken.

Für die nette Zeit an der GSI, an der ich einige Monate ausgeholfen habe, möchte ich außerdem Matt Brunet, Sudipta Saha, Elif Şahin, Jelena Vesić, Giorgia Pasqualato und Matthias Rudigier danken.

Außerdem möchte ich Janina Willmann, Maximilian Schumacher, Kai Hansmann, Till Böhmer, Philipp Ritzert und Bastian Zapf für die schöne Zeit während

[1] geb. Schilling

meiner Masterarbeit und den ausgiebigen Kaffeepausen danken. Ich wünsche ihnen für ihre zukünftige (wissenschaftliche) Laufbahn alles erdenklich Gute.

Für das Korrekturlesen dieser Arbeit möchte ich Johannes Wiederhold, Katharina Ide, Andreas Weber, Kai Hansmann und Maximilian Schumacher danken.

Besonderer Dank gilt meinen Freunden Antonio D'Alessio, Anna Möllerberndt, Simon Becker, Clara Meier, Tatjana Thiel und Simon Heeg für die netten gemeinsamen Stunden bei gutem Essen, die wir seit fast zehn Jahren miteinander verbringen, Ralph Kern für die unterhaltsamen Jahre im Büro 210, die leider etwas zu schnell vorbei gegangen sind, und Tobias Klaus für seine Hilfsbereitschaft in beruflichen und persönlichen Belangen sowie seine in keinster Weise arrogante Art beim Tischfußball.

Natürlich möchte ich auch meiner Verlobten Carolin, meinen Eltern Evelyn und Uwe, meinem Bruder Sebastian, meinen Großeltern Heidi und Hartmut, sowie meiner Schwiegerfamilie in spe Gabriele, Stephan, Felicitas, Julian, Leni, Barbara und Fleur für die moralische Unterstützung während meiner Promotion danken.

I also would like to thank my colleagues from LNL, José-Javier Valiente-Dobón, Alain Goasduff and Daniele Brugnara for the nice time at Legnaro and fruitful discussions about the measurement of the $\gamma\gamma/\gamma$ decay with AGATA and the development of `ExpTrack`.

Diese Arbeit wurde gefördert durch das Bundesministerium für Bildung und Forschung unter den Fördernummern 05P15RDFN9 und 05P18RDFN9, durch das Helmholtz International Center for FAIR (HIC for FAIR) und durch die Helmholtz Graduate School for Hadron and Ion Research (HGS-HIRe).

Lebenslauf

Removed from online version